SPATIOTEMPORAL CHARACTERIZATION

OF

INDOOR WIRELESS CHANNELS

by

Luis Gurrieri

A Thesis
submitted to the Faculty of Graduate Studies
in partial fulfillment of the requirements for the degree of
Master in Science
in
Electrical and Computer Engineering

Department of Electrical and Computer Engineering
University of Manitoba
Winnipeg, Manitoba R3T 5V6 Canada

THE UNIVERSITY OF MANITOBA

FACULTY OF GRADUATE STUDIES

*****

COPYRIGHT PERMISSION

SPATIOTEMPORAL CHARACTERIZATION OF INDOOR WIRELESS CHANNELS

BY

Luis Gurrieri

A Thesis/Practicum submitted to the Faculty of Graduate Studies of The University of Manitoba in partial fulfillment of the requirement of the degree

OF

MASTER OF SCIENCE

ABSTRACT

The continuous advancement in wireless communications technology demands new approaches to improving the capacity of existing radio links. The high data throughput required can be achieved by the complete utilization of space, time and polarization diversities inherent in any propagation environment. Among the different propagation scenarios, the indoor channels represent a particularly challenging problem given the number and complexity of interactions between the transmitted signal and the environment. This dissertation explores the interrelation between propagation physics and space-time-polarization diversity based on a novel high resolution channel sounding and reconstruction technique. First, a method to reconstruct the indoor complex channel response based on a limited set of samples and the elimination of the interference using deconvolution techniques is presented. Then, the results for the joint angle-of-arrival, delay characterization and depolarization of electromagnetic waves are presented. Finally, a novel approach to using depolarized multipath signals to boost the receiver signal-to-noise performance is presented. The current study shows that full utilization of the diversities of channel novel wireless systems can be proposed with significant improvement in capacity.

ACKNOWLEDGEMENTS

I would like to express my most sincere gratitude to my supervisors, Professor S. Noghanian and Dr. T. Willink, for their constant support and dedication helping throughout this research project. Their encouragement and inspiration during my research made this work possible.

I want to extend my gratitude to the people at the Communications Research Centre (CRC) in Ottawa for their unconditional support since the beginning of this project. I would like to acknowledge especially Dr. A. Petosa, S. Rauth, N. Cagnon and D. Lee from the Antenna Design and Development Group (CRC) that kindly offered me their advice and for facilitating part of the equipment used in this project. Thank you to Dr. R. Bultitude for sharing his experience in the propagation area and giving me opportune and intelligent suggestions. I would like to recognize G. Colman and C. Squires for their help, patience and friendly advice while I was working in Ottawa. Last but not least, I would like to thank Dr. N. Wang for his intelligent comments during the writing of this thesis.

Finally, I would like to thank the members of the committee Dr. E. Liu and Dr. P. Yahampath who took the time to read this dissertation.

This research was supported financially by the University of Manitoba, CRC, and Natural Sciences and Engineering Research Council of Canada.

This thesis is dedicated to my wife Carolina.
Despite of the long distance and the endless time apart,
her infinite patience and encouragement,
made everything possible.

TABLE OF CONTENTS

TABLE OF FIGURES

LIST OF TABLES

LIST OF ABBREVIATIONS

AoA	Angle-of-arrival.
AP	Access point.
ar	Aspect ratio.
AZELTI	Azimuth-elevation-time channel sounding platform.
BW	Bandwidth.
CCD	Charged coupled device.
CFA	Constant false alarm.
CIR	Complex impulse response.
c/ph	Cycles per picture height.
CRC	Communications Research Centre.
E-field	Electric field.
EM	Electromagnetic.
h_H	Horizontally polarized component of the CIR.
h_V	Vertically polarized component of the CIR.
f	Image representation of the CIR as function of the AoA.
f_{cst}	Image representation of the CIR after processing.
HPBW	Half-power beam-width.
H-field	Magnetic field.
ISI	Inter-symbol interference.
ISNR	Image signal-to-noise ratio.
LOS	Line-of-sight.
MED	Maximum excess delay.
MPC	Multipath component.
NLOS	Non-line-of-sight.
ph	picture height.
PN	Pseudonoise.

PSF	Point-spread-function.
pw	Picture width.
PWMED	Power weighted mean excess delay.
RMS	Root mean squared delay spread.
SAGE	Space-alternating generalized expectation maximization algorithm.
SLL	Sidelobe level.
SNR	Signal-to-noise ratio.
SS	Spread-spectrum.
TE	Transverse electric.
TM	Transverse magnetic.
ToA	Time-of-arrival.
UWB	Ultra-wide band.
VNA	Vector network analyzer.
WLAN	Wireless local area network.
WPAN	Wireless personal area network.
XPOL	Cross-polarization rejection.

LIST OF SYMBOLS

$\Delta\varphi$	Azimuth angular spread.
$\Delta\theta$	Elevation angular spread.
$\vec{E}$	Electric field vector.
$\vec{e_0}$	Unit vector in the direction of the E-field.
ε_r	Electric permittivity.
ε_0	Permittivity (free space).
μ_r	Relative magnetic permeability.
μ_0	Magnetic permeability (free space).
$\vec{H}$	Magnetic field vector.
$\vec{h_0}$	Unit vector in the direction of the H-field.
$\vec{H}$	Magnetic field vector.
$\vec{r}$	Coordinate vector.
Λ	Lattice structure for the initial sampling.
Σ	Reflection coefficient.
Γ	Lattice structure for the final image.
Γ^*	Reciprocal lattice of Γ.
σ	Conductivity of the material.
σ_{RMS}	RMS delay spread.
T	Transmission coefficient.

1 INTRODUCTION

In the last few years, there has been an increasing interest in the research community in exploring alternatives to provide high performance wireless systems in different environments and mobility scenarios. There are still many reasons to justify more research in this area. Market trends these days have imposed the paradigm of ubiquitous access to integrated services. Therefore, nowadays communication companies and governmental institutions are setting up future technology standards in terms of integration of existing services with new voice, data and multimedia ones pushing the boundaries of wireless communication networks. In order to achieve the high capacity required by the new wireless services it is necessary to exploit the diversity in space, time and polarization present in wireless channels. There has been a growing interest in recent years in the characterization and modeling of wireless channels as an attempt to improve existing models and increase the capacity of wireless links by combining space-time-polarization diversity.

Among the different branches into which the problem of exploiting the wireless channel's diversity can be subdivided, the characterization of indoor scenarios represents a particularly challenging problem. The indoor propagation channels vary from building to building and among locations in the same building. Propagation prediction methods based on software such as ray-tracing methods have been trying to accommodate the

incredibly large and complex variety of effects that create multipaths signals in these environments. There have been few attempts to contrast the results of these predictions against the results of direct channel measurements [76]. However, the inherent difficulty of characterizing the indoor wireless channel has discouraged many researchers from attempting indoor channel measurements. Recently, novel propagation models based on mathematical methods and deterministic simulations were proposed [48], [49] but, to the best of the author's knowledge, no attempts to contrast these models against empirical results have been made due to the complexity of the experiments. Accurate models for indoor propagation are required in order to fully exploit the space, delay and polarization diversity for maximizing the capacity of new wireless systems. These new and accurate models can only be proposed and optimized using channel measurements combined with signal processing techniques in order to upgrade the knowledge of the channel in these propagation channels. The first step in the research of indoor channels is the accurate and complete characterization of the propagation phenomena in space, time, and polarization.

In this dissertation, the results of a new channel sounding campaign designed to characterize the indoor channel in the 5.10-5.85 GHz frequency band are presented. This frequency band is of particular interest because of its usage in indoor wireless LANs (WLANs) [32] and wireless personal access networks (WPANs) [63]. The channel sounding campaign was carried out at the Communications Research Centre (CRC) in Ottawa. The indoor measurement campaign required the development of a novel sounding platform designed to acquire snapshots at programmed directions of the indoor channel with a delay resolution of less than 3 ns. Using these snapshots, the magnitude and phase of the multipath components (MPCs) were characterized as a function of their

azimuth and elevation angle-of-arrival (AoA) with 5° resolution in both angles. The platform was designed to take measurements of the channel in both polarizations in order to study the depolarization of MPCs in these kinds of environment in this frequency band.

1.1 INDOOR CHANNEL CHARACTERIZATION

The characterization of the indoor channel has been investigated in the last few years as a preceding step before the proposal of new propagation models that were based on measurement campaigns [62], [67] in contrast to those based on mathematical models [48], [49]. The advent of broadband applications at millimeter wavelengths for indoor WPANs and WLANs in the last decade [32], [39], [51], [63] was the motivation to renew research in the area of indoor propagation. It is possible to establish a direct relationship between the evolution of the characterization and modeling of indoor channels and the increasing demand for high capacity wireless systems in the last two decades [51]. The increasing research in space, time and polarization diversity to improve the performance of wireless links has determined the trends and improvements in the channel sounding techniques.

1.1.1 TIME CHARACTERIZATION OF INDOOR CHANNELS

In the late '80s and during the '90s, the increasing growth of voice- and data-oriented wireless networks motivated the study of the multipath propagation in diverse indoor environments, i.e. office and industrial environments. The typical parameters extracted from the time-domain measurements are the path loss, the mean excess delay and the root-mean-squared (RMS) delay spread. For this parameter characterization, it is sufficient to measure the received power delay profile. One of the simplest methods used in early indoor characterizations is the direct pulse method. Using this method, Saleh and Valenzuela measured the received power-delay profile at 1.5 GHz in an indoor office scenario and proposed a statistical model for the time-of-arrival (ToA) of MPCs [62]. In this power delay profile model, the MPCs arrive in clusters. The ToA for these clusters and MPCs within each cluster is determined by Poisson law while the MPCs' interarrival time obeys an exponential decaying law. A similar technique was used by Rappaport to characterize indoor channels in factory buildings at 1.3 GHz [58]. In this case, the path loss and delay statistics were measured for different locations and the median and variance of these channel parameters were given. In a later paper [59], Rappaport *et al.* reported their results for the first and second order statistics of the ToA and channel fading for factory environments. In all these cases, it was assumed *a priori* that the phase of MPCs is statistically independent and uniformly distributed in [0°, 360°), since, given the limitations in the direct pulse method, the signal phase variations in time cannot be measured. Another limitation to be considered is that the reception in all cases was made using omnidirectional antennas since the MPCs' AoA was not an issue to consider. Since

the Saleh-Valenzuela model was first proposed in the late '80s, it has had a considerable impact on the research community and it has been considered in other characterization reports of the indoor channel for IEEE 802.11 [27] and IEEE 802.15 [28]. In recent years, the direct pulse technique has been modified to characterize ultra-wide-band (UWB) channels [73] with the addition of a wide-band pulse generator and probe antenna at the transmitter side in order to provide a sounding pulse and a trigger signal for the storage oscilloscope. An excellent discussion about this method by Win and Scholtz can be found in [74].

In contrast to the direct pulse measurement that could only provide the power delay profile of the multipath signal received, other techniques can provide the magnitude and phase of each MPC. Spread-spectrum techniques are among these methods used in the indoor measurement of the time-domain complex impulse response (CIR) of the channel [35], [51], [54], [57]. This technique was used by Bultitude *et al.* to characterize the time-domain parameters in an indoor office environment at CRC in Ottawa [3], [4], [5]. Using this channel sounding method, the dependence of the indoor multipath ToA statistics with the distance between transmitter and receiver and the effect of the indoor clutter was reported in [43]. Bultitude *et al.* proposed in [6] a monotonic relationship for the RMS delay spread and the transmit/receive distance in empty indoor environments. This model can predict the channel delay statistics for static channels in those particular environments and it can be used in deterministic channel simulations, i.e. ray-tracing. However, the measurement results demonstrated that the presence of furniture destroys the predicted monotonic decay making the RMS delay spread independent of the range between transmitter and receiver. In addition, the presence of nearby buildings visible

through windows can effectively enlarge the dimensions of the indoor environment. In summary, it was concluded in this article that ray-tracing simulations can predict the propagation characteristics of a static indoor channel under strict boundary conditions, i.e., empty rooms without windows, but for closer to *real* indoor scenarios, additional complexity in the propagation model is necessary. Another interesting conclusion of this work is the limitation imposed by the channel sounding bandwidth (BW) in the characterization of the channel delay statistics. *Peaks* in the RMS delay spread were measured due to the noncoherent addition of multipaths within the resolvable time binwidth. This may lead to severe performance degradation in communication systems with limited delay resolution [23]. More recently, an extensive measuring campaign combining sliding-correlator channel sounding with different directional and omnidirectional antennas was reported in [35] at 5.3 GHz. The authors concluded that the best performance is achieved using multiple antennas in addition to a combining algorithm instead of using a single directive antenna for non-line-of-sight (NLOS) indoor environments.

One of the simplest and most powerful indoor channel sounding methods consists of the use of vector network analyzers (VNA) to measure the CIR in magnitude and phase. Unlike the direct pulse method that can capture wideband channel variations, the sweep time required by the VNA for each capture restricts its use to static or narrowband channels. Examples of the use of wide-band indoor channel time-domain characterization using VNA can be found in [10], [26], [30]. In recent years, frequency domain sounding techniques has been used to characterize UWB channels [7], [8]. The statistical results for the ToA in all these cases only considered the omnidirectional reception of MPCs which

is a reasonable criterion for the design of point-to-point or point-to-multipoint indoor links where only omnidirectional, linearly polarized antennas are used. Another point to ponder is that in some cases such as [7], the time characterization was made in empty indoor locations that are not representative of the type of indoor scenarios they tried to characterize. Finally, only single co-polarized reception was considered.

1.1.2 SPACE-TIME CHARACTERIZATION IN INDOOR ENVIRONMENTS

The techniques for AoA extraction from a measured arriving signal are Fourier-based [24], [52] and beam-forming methods [55]. The first reported measurement of the indoor propagation that included the AoA of MPCs was made by Lo and Litva in [38]. They used a modified sliding correlator method. In this case, an omnidirectional antenna was utilized at the receiver to measure the CIR at each of four points on a circle around the central location. A 950 MHz CW was modulated using a 40 Mchips/s pseudonoise (PN) sequence and transmitted using an omnidirectional antenna. The signal was post-processed to emulate a *virtual* circular array and the CIR was characterized for each azimuth and elevation angle using beam-forming techniques. The intrinsic problem of this method is the dependence between the radiation pattern sidelobe levels and the scanning angle, introducing errors in the CIR characterization by noncoherent addition of MPCs arriving from undesired angles. The small number of elements in the virtual array also implies a low AoA resolution as a result of a wide antenna main beam. Improvements in this virtual array technique such as more capture points, automatic

receiver antenna location and capture, and different virtual array configurations have been used consistently since then to provide a better angular resolution [47], [16], [75].

After the reported theoretical limits of the channel capacity achievable by using space and time diversity simultaneously [18], the interest in characterizing the joint AoA-ToA statistics of indoor and outdoor wireless channels was renewed. A modification of the wide-band sounding technique was used to characterize and model the joint AoA and ToA on indoor channels by Spencer *et al.* in [66], [68]. In this case, a parabolic dish antenna in the X-band (6.75-7.25 GHz) with a narrow main beam (6° half-power-beamwidth) was rotated to different azimuth angles to capture channel snapshots at discrete angular intervals. If the same experiment setup has to be implemented in indoor environments at a lower frequency, i.e., at 5.2 GHz, the reflector diameter must be about 1.3 m, making it difficult to guarantee that the radiation pattern will remain independent of the scanning angle due to near field distortive effects. Since the sampling is done sequentially, special measures have to be taken to guarantee that the channel is static during the acquisition time. Spencer *et al.* proposed a statistical model by adding the azimuth AoA to the Saleh-Valenzuela model for the ToA of MPCs [67]. For this model the statistical independence of the azimuth AoA and ToA was assumed. The main addition to the Saleh-Valenzuela model is the addition of MPC clusters in the horizontal plane (elevation = 90° with respect to the vertical axis). The location of these MPC clusters was proposed to be uniformly distributed in azimuth and the ToA distribution with respect to the median of clusters was Laplacian. A modified version of this model has been recommended by the IEEE 802.11n Task Force for MIMO channels [27], [51]. The method used by Spencer *et al.* to characterize indoor channels only considered co-

polarized MPCs limited to the neighbourhood of the horizontal plane. A modification of this sounding technique was used to characterize the clustering phenomena in azimuth and elevation AoA for both polarizations in this dissertation and partial results of this research have been reported in [24] and [23].

1.1.3 SUPER-RESOLUTION AND DECONVOLUTION TECHNIQUES

The radiation pattern of the receiver antenna system is an important factor to consider in the implementation of a channel sounder. High sidelobes in the receiver antenna radiation pattern create interference due to the noncoherent combination of MPCs with AoAs different from the main beam. These main-lobe to side-lobe and side-lobe to side-lobe interaction effects cause errors in the AoA detection affecting the spatio-temporal clustering characterization of MPC's clusters. When the radiation pattern is well known, it is possible to minimize the uncertainty in the AoA of MPCs by eliminating undesired effects of the antenna radiation pattern. Deconvolution techniques to eliminate these effects were proposed by Gans *et al.* in [20]. A recursive technique for the elimination of radio frequency interference using the method called CLEAN was proposed by Leshem *et al.* in [37]. CLEAN is a deconvolution algorithm originally used to deblurr astronomical images [29]. Spencer *et al.* post-processed the acquired CIR at different scanning angles using the CLEAN algorithm [66], [67], [68] to improve the angular resolution, similar to what Cramer *et al.* did in [11]. Improvements in this technique were proposed by Bose in [2] to increase the accuracy in the extraction of MPC's AoAs based

on a sequential recursion procedure. Another technique to improve the resolution of the channel parameters is the space-alternating generalized expectation-maximization algorithm (SAGE). This technique, as well as the previous deconvolution methods, is based on the recursive evaluation and subtraction of parameters from the measured signal. However, for the use of SAGE it is assumed that planar waves impinge on the receiver array. Fleury *et al.* proposed the application of the SAGE algorithm to the channel measured using a linear array to improve the AoA resolution [17].

1.1.4 POLARIZATION CHARACTERIZATION IN INDOOR ENVIRONMENTS

The depolarization of electromagnetic waves in indoor environments has been reported from measurements in the early and mid '80s. Polarization diversity systems rely on multiplexing the data streams onto orthogonally polarized channels in order to improve the system capacity. Therefore, the early attempts of polarization characterization were focused on characterizing the total amount of depolarization that occurs between horizontally and vertically polarized signals propagating in indoor and outdoor environments. The cross-polarization of signals is an important measure of the amount of correlation between channels in polarization diversity systems. The difficulty that arises in the characterization of both polarized components of the impinging wave's electric field (E-field) is caused by the radiation pattern used to measure each polarized signal. Therefore, the antenna system selected, along with the sounding technique, are critical factors to be considered. Cox *et al.* measured the indoor and outdoor total

depolarization of signals using electric and magnetic dipoles in [10]. These results were contrasted against those obtained from ray-tracing simulations in [9]. There have been a few attempts to measure the amount of depolarization using diverse antennas [41]. Among them one can mention studies done by Rappaport *et al.* [60], [61] regarding the effects of linearly and circularly polarized antennas on the indoor propagation parameters. Other results were reported by Manabe *et al.* in [42] made at 60 GHz that led to the conclusion that multipath signals are suppressed by using circularly polarized antennas. The first approach to characterizing the joint AoA-polarization was made by Kallioka *et al.* in [33] and a model for the power distribution using these results was presented in [34]. However, to the best of the author's knowledge, there are no results reported for the joint AoA-ToA-polarization characterization for indoor environments.

1.2 PROBLEM DEFINITION

The objective of this work was to characterize the indoor wireless channels with high resolution in ToA and AoA for both received polarizations, using a vertically polarized antenna at the transmitter side. This required the development of a sounding system capable of measuring the indoor propagation with the desired resolution, and the use of super-resolution signal processing techniques to extract the required parameters. The channel parameters were studied in terms of AoA, ToA and polarization effects in two different locations, selected according to their relevance to indoor communications.

The required resolution was determined as follows. The maximum excess delay in indoor channels was reported to be between 200 ns and 300 ns [62], [68]. Hence, the maximum signal capture time had to be chosen considering the maximum excess delays in both chosen locations. The RMS delay spread of the indoor channel had to be characterized as a function of the AoA for those angles of relevant signal strength for both polarizations. Published results using omnidirectional antennas reported median RMS delay spread of 40 ns for office environments [5], [6] and 100 ns for industrial buildings [58]. The typical path length difference reported for indoor office scenarios is less than 90 cm, or equivalently, a multipath delay resolution better than 10 ns [51]. The resolution of the proposed system in azimuth and elevation AoA had to be better than 5° to allow the resolution of small MPCs clusters for each time bin.

The CIR was characterized using the same radiation pattern antenna for both polarizations enabling the comparison between co- and cross-polarized power distribution and temporal statistics. Special measures had to be taken to minimize or eliminate the undesired effects of the radiation pattern. In addition, the near field effects had to be considered when designing the sounding platform antenna in terms of the locations under study.

The results obtained in literature for omnidirectional reception of both polarized components were contrasted with the results obtained from the resolution characterization. The high spatial and temporal resolution enabled the study of the effects of the scatterers in the formation of power clusters as a function of the AoA and ToA of MPCs for both polarizations. The aim was to study the effects of the scatterers in the formation of MPC clusters, and to characterize the depolarization of clusters as a function

of the AoA and ToA. This was undertaken by investigating the power distributions as a function of space and delay, jointly and separately, for both polarized components. The case of omnidirectional reception of both polarization components and their combination were simulated based on the measurements results.

1.3 THESIS ORGANIZATION

This thesis is organized into seven chapters and two thematic appendices. The first chapter contains a study of the evolution of the time, space and polarization characterizations and how they are related to the improvements in capacity performance of wireless systems. The objectives of the thesis are presented here.

Chapter 2 is dedicated to introducing some principles of multipath propagation such as reflection, transmission and scattering of signals in indoor scenarios as a means to supporting the multipath creation phenomena in terms of the physical model. The data model for the joint angle-delay-polarization CIR which is used through out this entire dissertation is presented here. The statistical model for the data thresholding used to discriminate multipath from the signal is introduced in this chapter. Finally, the mean excess delay, RMS delay spread and cross-polarization factor are defined.

In Chapter 3, the different channel sounding techniques are studied in detail and the best method is defined in terms of the indoor channel sounding requirements defined in Chapter 1. The Azimuth-Elevation-Time (AZELTI) platform designed and built for this

project is presented in this chapter. The receiver antenna characterizations for the E- and H-planes as well as the cross-polarization rejection are also presented. Finally, a description of the test locations is given along with descriptive illustrations of the surrounding scatterers.

Chapter 4 explains the CIR reconstruction as a function of the AoA and ToA using the measured snapshots of the indoor channel. The mathematical formulation of the spatial sampling using 2-D lattices is given as a preamble to explain the CLEAN deconvolution algorithm. The procedure to extract the AoA of the dominant MPCs is presented in this chapter.

In Chapter 5, the AoA power distribution results are presented for co- and cross-polarized signals. The clustering locations, their angular spread and the dynamic AoA for both polarizations are compared in terms of their excess delays. Finally, the mean excess delay and RMS delay spread are studied for both polarizations and the results of the characterization in both locations are contrasted.

In Chapter 6, the cross-polarization phenomenon in both indoor locations selected for this study is explained in terms of the scatterers' distribution. The azimuth and elevation cross-polarization distribution is compared for both locations. Finally, the performance of a receiver in terms of the system bandwidth for the omnidirectional reception of co- and cross-polarized components based on the measured results is studied.

Chapter 7 contains the conclusion for this research and recommendations to be considered for future work.

2 THE INDOOR CHANNEL MODEL

2.1 INTRODUCTION

The design of communication systems for operation in indoor environments requires taking into account the propagation characteristics that are imposed on the transmitted signal. An accurate model of the indoor channel based on an improved understanding of the propagation problems in these scenarios will improve the performance of high capacity communication systems. In some cases, the indoor channel limitations can be seen as barriers for the achievable capacity but, as it will be seen later, it can be advantageous for communication systems based on space, time and polarization diversity. In this chapter, the mathematical model for the multipath channel will be introduced. The fading model for the indoor channel will be presented taking into account the 3-D distribution of scatterers and obstacles that surround the receiver. Interaction with the commonly found indoor clutter, walls and diverse scatterers creates delayed and attenuated copies of the transmitted signal as a result of the reflection, transmission and scattering of the electromagnetic (EM) waves as illustrated in Figure 2.1. In Section 2.2,

an introduction to the propagation phenomenon that creates multipaths signals and their relationship with the small scale fading will be given. The creation of cross-polarized signals after reflections from indoor obstacles, i.e. walls, floors, ceilings, and other materials, will be discussed in Section 2.2. This phenomenon will be characterized in detail in Chapter 6 for the studied indoor scenarios. The mathematical signal model as a function of the azimuth and elevation angles and the signal delay will be presented in Section 2.4, and the data thresholding method used in the identification of MPCs will be discussed in Section 2.5. The excess delay and polarization parameters used in the channel characterization through out this dissertation will be introduced in Section 2.6.

2.2 MULTIPATH PROPAGATION IN INDOOR ENVIRONMENTS

Modeling and characterization of indoor propagation are challenging tasks given the physical constraints imposed on the multipath signal reception. The physical phenomena that give rise to the creation of delayed echoes of the transmitted signal that are received with different attenuations, at different delays and angle-of-arrivals (AoAs) are [57]:

- Reflection: A plane EM wave that impinges upon a discontinuity between the medium in which it is propagating (i.e. air) and a second medium (i.e. walls, floors, ceilings), whose dimensions are large compared to the wavelength of the incident wave, is partially reflected back to the medium where it is propagated.

- Transmission: Under the same boundary conditions applied to the reflection of an EM wave on a planar surface, the part of the EM wave that does not *bounce back* into the first medium is transmitted into the second medium. Depending on the second material's dielectric properties, part of the EM wave energy is dissipated. This process explains the transmission of significant parts of the incident EM wave through walls, floors, and ceilings enabling NLOS links. However, in other cases, the transmission of EM waves causes undesired interference among floor levels and access point (AP) coverage areas in indoor WLANs.

- Diffraction: When obstacles with sharp edges such as a wall corner or material wedges are in the radio path between transmitter and receiver, then secondary EM waves are created, therefore, reception around corners is possible even though there is no line-of-sight (LOS) path available.

- Scattering: This phenomenon occurs when the dimensions of the obstacle are small compared to the wavelength of the traveling EM wave. It also depends on the number of these obstacles and their 3-D distribution around the receiver. Scattered waves are produced by rough surfaces, small objects, or by other irregularities in the channel.

The creation of multipath signals is highly dependent on the dielectric properties of the obstacles, their physical shape, and the magnitude, phase, frequency and polarization of the impinging wave. For instance, it is expected that a short excess delay spread would be observed between MPCs due to the proximity, the amount, and the topology of scatterers in the receiver's surrounding. It is the proximity of obstacles in the signal path that causes EM distortive effects on the receiver and transmitter radiation patterns, making identifying MPCs accurately even harder.

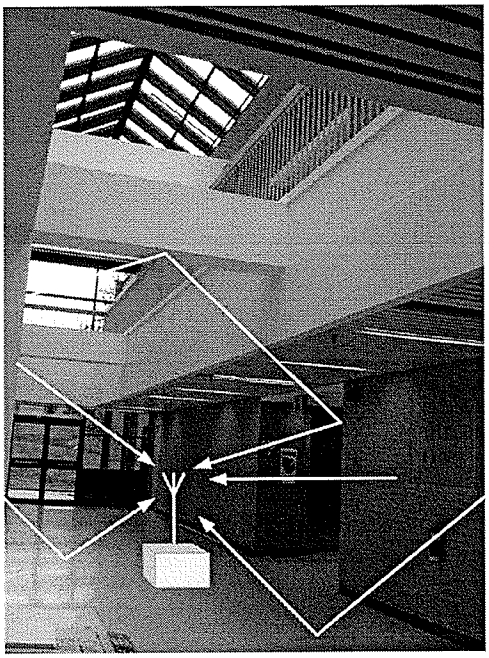

Figure 2.1. An example of the multipath propagation phenomena in indoor environments.

The received signal is the superposition of the individual MPCs created by reflection and scattering of the transmitted wave, which after arriving with different phases and attenuations may be added constructively or destructively resulting in signal fading. It is clear that the receiver antenna radiation pattern has an impact on the received signal due to the selective noncoherent addition of MPCs arriving from distinct AoAs.

In this study the focus is on scenarios in which the transmitter, receiver and surrounding environment are static. The fading then depends almost entirely on the scatterers' distributions and their EM properties. The fading in indoor environments is commonly known as fast-fading since small changes in the receiver location produce abrupt changes in the received power. This is caused by the coherent addition of scattered MPCs in a complex propagation environment like most indoor scenarios. In contrast,

slow-fading channels are common in other propagation scenarios, typically outdoor environments, where there is long-term variation in the mean value of the received signal [54].

2.3 PLANE WAVE PROPAGATION

In order to understand the reflection and transmission of a plane wave after interacting with obstacles with diverse dielectric properties, the physical process and characteristics of materials that intervene in the creation of multipath signals in indoor scenarios need to be understood. Expressions for plane waves as functions of the electric and magnetic fields can be obtained solving the Maxwell's equations in an unbounded region. Usually designated as $\vec{E}$ and $\vec{H}$, the electric field (E-field) and magnetic field (H-field) dependence on the position and time for the plane wave propagating in an arbitrary direction are

$$\vec{E}(\vec{r},t) = \vec{e_0} A\cos(\omega t - \vec{k}\cdot\vec{r} + \phi) \tag{2.1}$$

and

$$\vec{H}(\vec{r},t) = \vec{h_0}\frac{A}{\eta_d}\cos(\omega t - \vec{k}\cdot\vec{r} + \phi) \tag{2.2}$$

where $\vec{e_0}$ and $\vec{h_0}$ are unit vectors in the directions of polarization of $\vec{E}$ and $\vec{H}$, respectively, $\omega = 2\pi f$, where f is the wave frequency, k is the wavenumber vector in the xyz coordinate system defined as $\vec{k} = k_x\,\vec{x_0} + k_y\,\vec{y_0} + k_z\,\vec{z_0}$, such that $k_i = \omega/v_i$, where v_i is

the velocity of propagation in the medium in the $\vec{x_0}$, $\vec{y_0}$, and $\vec{z_0}$ directions, ϕ is the initial phase, r is the location vector in xyz, A is the magnitude of the E-field, and η is the wave impedance of the medium.

The relative permittivity (ε_r) and the relative permeability (μ_r) of the material where the wave is propagating is related to the wavenumber k_i and the impedance of the medium by

$$k_i = \omega\sqrt{\varepsilon_r\varepsilon_o\mu_r\mu_o} \tag{2.3}$$

and

$$\eta = \sqrt{\frac{\mu_r\mu_0}{\varepsilon_r\varepsilon_o}} \tag{2.4}$$

where ε_o is the permittivity of a vacuum and μ_o is the magnetic permeability also of a vacuum. The electric and magnetic fields can be represented with complex exponentials more conveniently as

$$\vec{E}(\vec{r},t) = \mathrm{Re}\left\{\vec{E}(\vec{r})\exp(j\omega t)\right\} \tag{2.5}$$

and

$$\vec{H}(\vec{r},t) = \mathrm{Re}\left\{H(\vec{r})\exp(j\omega t)\right\} \tag{2.6}$$

where

$$\vec{E}(\vec{r}) = \vec{e_0}A\exp(-j\vec{k}\cdot\vec{r}+\phi) \tag{2.7}$$

and

$$\vec{H}(\vec{r}) = \vec{h}_0 \frac{A}{\eta} \exp(-j\vec{k} \cdot \vec{r} + \phi) \tag{2.8}$$

The propagation direction of a plane wave with arbitrary polarizations for $\vec{E}$ and $\vec{H}$ in the *xyz* reference system as shown in Figure 2.2 is defined by the Pointing vector as

$$\vec{P} = \frac{1}{2} \mathrm{Re}\left\{\vec{E} \times \vec{H}^*\right\} \tag{2.9}$$

where $\vec{H}^*$ represents the complex conjugate of the magnetic field phasor and $\times$ represents the vector product. Since the E- and H-fields are orthogonal, the direction of propagation, which is the direction of the Pointing vector, is given by the direction of the wavenumber vector $\vec{k}$, i.e.

$$\vec{e}_0 \times \vec{h}_0 = \vec{k} / \left|\vec{k}\right| \tag{2.10}$$

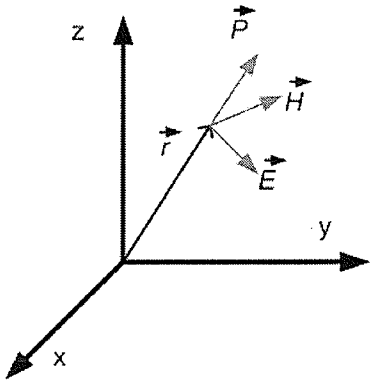

Figure 2.2. Pointing vector.

2.3.1 REFLECTION AND TRANSMISSION OF PLANE WAVES

A plane wave that is propagating through a boundary between two mediums with different dielectric properties is partially reflected back into the first medium and partially transmitted into the second medium. The necessary condition for this to happen is that the dimensions of the planar obstacle have to be much larger than the wavelength. For instance, this condition is largely satisfied by floors and walls commonly found in indoor environments. Figure 2.3 illustrates the process for a planar wave propagating in the *xy* plane, where $\vec{k}$, $\overrightarrow{k_R}$, and $\overrightarrow{k_T}$ are the wavenumber vectors for the incident, reflected, and transmitted waves, respectively. In order to satisfy the boundary conditions for the electric and magnetic fields at $x = 0$, the incident and reflected wavenumber vectors projection in the *xy* plane must be the same [1]. Figure 2.4 shows a graphical interpretation of this boundary condition where it is clear that the incidence angle, θ, must be the same as the reflection angle, θ_R. The familiar Snell's law can be deduced from this boundary condition after writing the *x* components of the wavenumber vectors as a function of the planar wave angles

$$\sin\theta = \sin\theta_R = \sqrt{\varepsilon_r}\sin\theta_T \tag{2.11}$$

or, as a function of the two mediums' EM properties,

$$\sqrt{\mu_1\varepsilon_1}\sin\theta_R = \sqrt{\mu_2\varepsilon_2}\sin\theta_T \tag{2.12}$$

where μ_i and ε_i are the magnetic permeability and permittivity for the medium $i = \{1, 2\}$, respectively. The amplitudes and propagation directions of transmitted and reflected plane waves can be obtained using the Snell's law.

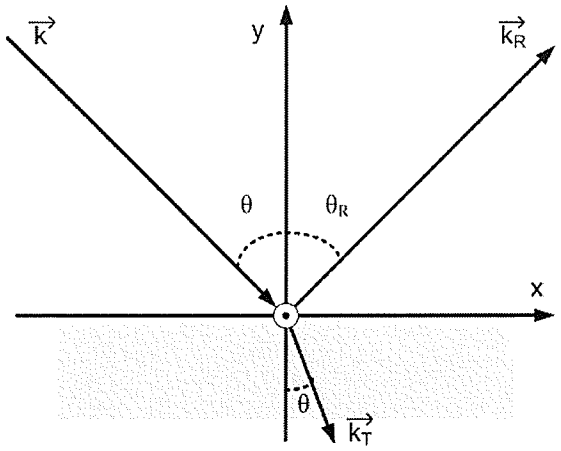

Figure 2.3. Transmission and reflection in a planar boundary.

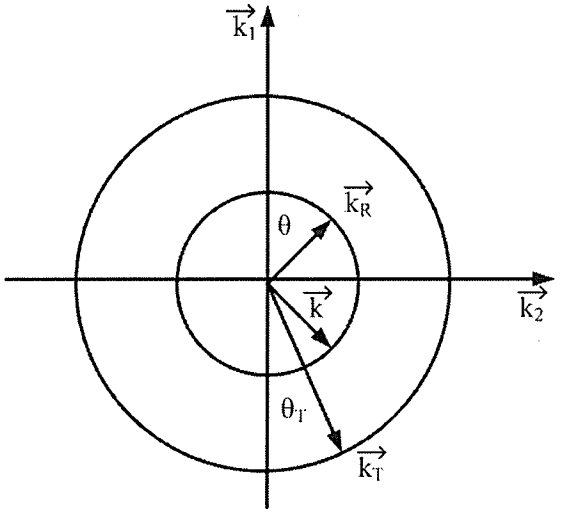

Figure 2.4. Graphical interpretation of Snell's law in the wavenumber vector plane.

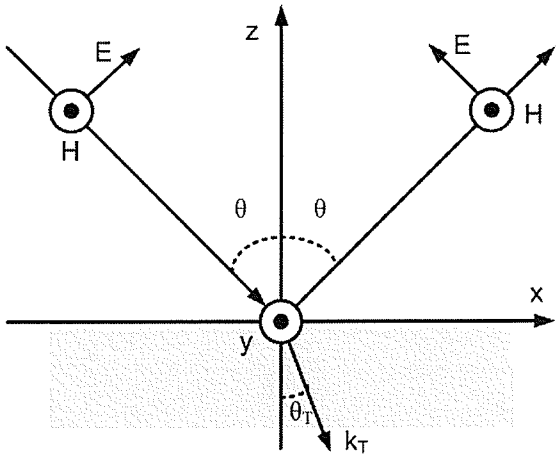

Figure 2.5. Reflection and transmission of a TM polarized plane wave on the planar boundary between materials.

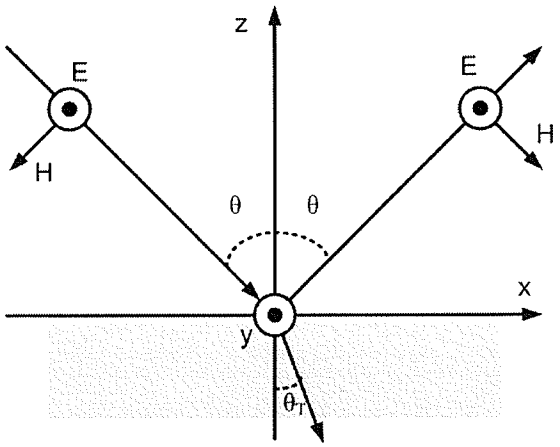

Figure 2.6. Reflection and transmission of a TE polarized plane wave on the planar boundary between materials.

This problem of a plane wave on a planar boundary between materials can be studied by identifying the two polarization cases for the incident wave:

- TM: H-field transverse to the plane of incidence (Figure 2.5); and
- TE: E-field transverse to the plane of incidence (Figure 2.6).

The plane of incidence contains the wavenumber vector and the normal to the planar boundary between materials simultaneously. Given the coordinate system used in Figures 2.4 and 2.5, if the z axis is considered pointing upwards, then the planar surface is in the xy plane. Consequently, the TM case can be seen as a wave that has both vertical and horizontal polarized components of the E-field arriving from a medium (i.e. air) at a planar discontinuity such as a floor or ceiling. In the TM case, the wave is partially reflected back to the medium and partially transmitted into the material. The change in polarization and magnitude for both orthogonally polarized components of the E-field explains the phenomenon called depolarization. The characterization of this phenomenon is introduced in Section 2.6.2. Considering the same coordinate system, the TE case represents the propagation of a horizontally polarized wave. As it can be seen in Figure 2.6, the E-field polarization is not changed after the reflection but its magnitude may change. This simple model for the interaction between a plane wave and a surface can be used to explain the interactions between walls, floors, ceiling and others planar surface whose dimension is several wavelengths.

The expression that relates the reflection coefficient (Σ) to the relative dielectric constant for the TE case is [1]

$$\Sigma_{TE} = \frac{|E_R|}{|E|} = \frac{\cos\theta - \frac{\eta_2}{\eta_1}\cos\theta_T}{\cos\theta + \frac{\eta_2}{\eta_1}\cos\theta_T} \tag{2.13}$$

where $|E|$ and $|E_R|$ are the incident and reflected E-fields, respectively, and η_i is the wave impedance of the medium i as defined in (2.4).

For the TM case, the reflection coefficient is given by

$$\Sigma_{TM} = \frac{|E_R|}{|E|} = \frac{\frac{\eta_2}{\eta_1}\cos\theta - \cos\theta_T}{\frac{\eta_2}{\eta_1}\cos\theta + \cos\theta_T}. \tag{2.14}$$

The transmission coefficients (T) are related to the reflection coefficients in both cases by

$$T = 1 + \Sigma. \tag{2.15}$$

The EM properties of most materials exhibit variations with the frequency that can be a problem for characterizing the indoor environments using short pulses considering the large BW required. Since the reflection and transmission coefficients depend on the dielectric properties of the materials involved in these processes, short duration pulses may be distorted after the interaction with these materials [44]. The dielectric properties of different materials have been characterized historically for several single frequencies and in recent years, after the increasing interest in UWB communications, the frequency dependence of various materials commonly found in building has been studied [45]. The complex expression for the dielectric constant is given by

$$\varepsilon_r = \varepsilon'_r - j\varepsilon''_r = \varepsilon'_r - j\frac{\sigma}{\omega\varepsilon_0} \tag{2.16}$$

where σ is the conductivity of the material. The imaginary part of ε_r represents the energy absorbed by the dielectric material. An additional problem in characterizing the dielectric properties of materials of interest such as walls, floors, ceilings, etc., is the variations in

their compositions that change their absorptive and reflective behaviour in the frequencies of interest. For instance, due to the high dielectric constant of water, the amount of water present in bricks, concrete, and ground floors will determine their EM properties, therefore channel characterization is highly dependent on the location.

2.4 THE MULTIPATH SIGNAL MODEL

The bandpass transmitted signal can be modeled following [56] as

$$s(t) = \mathrm{Re}\{s_l(t)\exp(-j2\pi f_o t)\} \tag{2.17}$$

where s_l is the lowpass signal and f_o is the carrier frequency. The signal defined in (2.17) is transmitted and, after being scattered, is received as the coherent addition of delayed and attenuated multiple lowpass signals. At a given AoA, defined by the azimuth and elevation AoAs, φ and θ, respectively, the received signal can be represented as

$$r(\varphi,\theta,t) = \sum_{k=1}^{N(\varphi,\theta,t)} \alpha_k(\varphi,\theta,t)\exp(-j2\pi f_0 \tau_k(\varphi,\theta,t))s_l(t-\tau_k(\varphi,\theta,t)) \tag{2.18}$$

where $N(\varphi,\theta,t)$ is the number of multipaths, $\tau_k(\varphi,\theta,t)$ is the ToA of the k^{th}-multipath, and $\alpha_k(\varphi,\theta,t)$ is the channel gain coefficient for the k^{th}-MPC arriving at τ_k. In case of a time-varying channel, N, τ_k and α_k not only depend on the AoA but also on time. However, in the case studied here, the channel is considered static. Therefore, the channel gain, the number of MPCs and their delay are considered functions of the AoA only. The bandpass received signal can be expressed as follows

$$r(\varphi,\theta,t) = \int_{-\infty}^{\infty} h(\varphi,\theta,\tau)s_l(t-\tau)d\tau \tag{2.19}$$

where $h(\varphi,\theta,\tau)$ is the time-invariant CIR as a function of the AoA defined as

$$h(\varphi,\theta,\tau) = \sum_{k=1}^{N(\varphi,\theta)} \beta_k(\varphi,\theta)\delta(t-\tau_k(\varphi,\theta)) \tag{2.20}$$

where β_k is the complex channel gain for the MPC arriving with delay $\tau_k(\varphi,\theta)$ that can be written as follows

$$\beta_k(\varphi,\theta) = \alpha_k(\varphi,\theta)\exp(-j2\pi f_0\tau_k(\varphi,\theta)). \tag{2.21}$$

In order to completely characterize the propagation in any environment, the magnitude ($\alpha(\varphi,\theta)$) and phase ($-j2\pi f_0\tau_k(\varphi,\theta)$) of the CIR have to be measured.

2.5 IMPULSE RESPONSE ESTIMATION

In the channel measurement the received signal (2.18) is distorted by noise, which impacts negatively on the quality of the channel estimate. The valid MPCs are discriminated from the measured impulse response defining the appropriate signal threshold. The CFA thresholding proposed by Sousa in [62] provides a suitable method. The presence of additive white Gaussian noise (AWGN) with a variance σ_N^2 was assumed, which is reasonable in the environments where the experiment took place. The envelope of the signal magnitude can be modeled as Rayleigh distributed random variable with probability density function (pdf) given by

$$p(x) = \frac{x}{\sigma_N^2} \exp\left(\frac{-x^2}{2\sigma_N^2}\right) \tag{2.22}$$

The probability of having one single false alarm, defined as a peak of noise incorrectly detected as a MPC, can be expressed as

$$P(X > x_{th}) = \exp\left(\frac{-x_{th}^2}{2\sigma_N^2}\right) \tag{2.23}$$

where x_{th} is the CFA threshold. One single false alarm in the total number of samples is equivalent to

$$P(X > x_{th}) = \frac{1}{NM} \tag{2.24}$$

where N is the number of samples per channel snapshots and M represents the total number of channel snapshots. In our case, $N = 401$ and $M = 72 \cdot 25 = 1800$. From (2.23), the signal threshold is

$$x_{th} = 3.766\sigma_N \tag{2.25}$$

where σ_N is the noise magnitude estimation. When x is equal to the median of the impulse response magnitude μ_x over all samples, setting the probability $P(X > \mu_x) = 0.5$ leads to

$$\sigma_N = \frac{\mu_x}{\sqrt{\ln(4)}} = 0.85\mu_x \tag{2.26}$$

The noise magnitude was estimated over the total number of channel samples for both polarizations.

2.6 PARAMETER CHARACTERIZATION OF THE INDOOR CHANNEL

The main objective of this project is to gather relevant and accurate information of the indoor propagation channel in terms of AoA, ToA and signal polarization. In this section, the direction, temporal, and polarization variables chosen to study the indoor channel will be presented.

2.6.1 TOA PARAMETERS

The temporal dispersion of the channel was investigated by the calculation of the root-mean-squared (RMS) delay spread (σ_{RMS}), and the power-weighted mean excess delay (PWMED). These parameters are widely used in the literature [57] to describe the statistical measure of the channel time dispersion. The PWMED and σ_{RMS} can be expressed as

$$\text{PWMED}(\varphi,\theta) = \frac{\sum_{k=1}^{N} P_k(\varphi,\theta)\left(\tau_k^{(\varphi,\theta)} - \tau_o^{(\varphi,\theta)}\right)}{\sum_{k=1}^{N} P_k(\varphi,\theta)} \tag{2.27}$$

and

$$\sigma_{RMS}(\varphi,\theta) = \sqrt{\frac{\sum_{k=1}^{N} P_k(\varphi,\theta) - \left(\tau_k^{(\varphi,\theta)} - \tau_o^{(\varphi,\theta)}\right)^2}{\sum_{i=1}^{N} P_k(\varphi,\theta)} - \tau(\varphi,\theta)^2} \tag{2.28}$$

where P_k and τ_k are the power and time delay of the k^{th} MPC as a function of the AoA, respectively, and τ_0 is the time delay of the first valid MPC with (φ, θ) AoA detected using the data thresholding defined in Section 2.5. The characterization of the delay statistics as a function of the AoA for two cases of indoor propagation will be presented in Chapter 5.

2.6.2 POLARIZATION PARAMETERS

The cross-polarization coupling (*XPOL*) is used to quantify the amount of received power that is received in a polarization state orthogonal to its original transmitted mode [9]. This coupling effect may happen due to interactions with the environment, i.e., walls, floors and indoor clutter after reflections, transmissions and diffractions of the transmitted signal. When vertically polarized antennas are used at both sides of the link, which is common practice in indoor communications, the *XPOL* may be used as a measure of the amount of power that arrives at the receiver location as horizontally polarized MPCs and is therefore undetected. The *XPOL* as a function of the AoA and delay is defined as

$$XPOL(\varphi,\theta,\tau)=\frac{P_h(\varphi,\theta,\tau)}{P_v(\varphi,\theta,\tau)} \tag{2.29}$$

where P_h and P_v are the total received power due to horizontally and vertically polarized MPCs, respectively. Early studies performed at lower frequencies are not well suited to describe the behaviour of indoor channels at frequency bands and data rates of interest

nowadays [44]. Ray-tracing simulations at UHF frequencies reported that, when vertically polarized antennas are used at both sides of the link, cross-polarization losses may be ignored [18]. It will be seen that, for the frequencies used in this study, this conclusion is true only for AoAs restricted to the horizontal plane. In Chapter 6, the cross-polarization characterization as a function of the azimuth and elevation AoAs of two distinct indoor channels will be presented.

2.7 SUMMARY

In this chapter, the physical processes that creates multipath signals for indoor propagation were reviewed. The reflection and transmission coefficients were introduced for the two cases of interaction with planar boundaries materials, TE and TM, and their relationship with the dielectric properties of the material commonly found in indoor scenarios. The change in the polarization of the E-field was identified as a result of the reflection of plane waves at dielectric surfaces. The frequency dependence of the dielectric properties of materials that results in a distortive effect on wide band signals was described. All of these effects influence the characterization of indoor wireless channels. The multipath signal model that is used in the analysis for the characterization of the results was presented in Section 2.4. Finally, the mathematical expressions for the characterization of the MPCs' delay and polarization in terms of the AoA were presented in this chapter. The expressions presented here are used in the extraction of parameters

for the joint AoA-ToA characterization of indoor channels, whose results are presented in Chapter 5, and to study the creation of cross-polarized MPCs and its dependence on the AoA, whose results are introduced in Chapter 6.

3 INDOOR CHANNEL SOUNDING

3.1 INTRODUCTION

In this chapter, the different channel sounding techniques that were explored will be presented. The selection of the most suitable method to acquire the complex channel samples was determined by the delay resolution imposed by the indoor channel and by the need to characterize the channel for different AoA and polarization with the same spatial response. In Section 3.2, the requirements for the channel sounding system are analyzed in detail. The viability of the direct pulse method, the sliding correlator technique and the frequency domain direct channel measurement are contrasted in Section 3.3. The sounding platform designed for the measurement campaign whose results are presented in this dissertation is presented in Section 3.4. The indoor locations chosen to be characterized are described in Section 3.5. Finally, the data acquisition procedure and calibration procedures are presented in Sections 3.6 and 3.7.

3.2 REQUIREMENTS FOR THE CHARACTERIZATION OF THE INDOOR CHANNEL

Different channel sounding techniques can be used to characterize indoor wireless environments. However, certain restrictions are imposed by the propagation physics in this kind of scenario, making some techniques more attractive than others depending on which channel parameters are going to be measured. The goal of this dissertation is to characterize the indoor channel propagation in terms of the AoA and ToA for co- and cross-polarized signals, collecting quantitative values for parameters that help the development of improved spatio-temporal models. The inherent difficulties of indoor environments such as time resolution in the scale of tens of nano seconds and multipath AoA resolution on the order of less than ten degrees for both polarizations impose strict design specifications on the channel sounder technique.

Typically, the arrival time of delayed copies of the transmitted signal, or *echoes*, is on the order of 5 ns in office and residential environments, which is equivalent to less than 1.5 m total propagation path difference. Saleh and Valenzuela reported excess delays of 200 ns as a result of early measurements [62]. This value was updated to 150 ns after more recent measurement campaigns made in similar types of indoor scenarios [66]. These results depend on factors such as the scatterers' distribution and composition, relative location of transmitter and receiver, floor plan, etc. In addition, the proximity of

scatterers to the receiver and transmitter is critical in terms of the near-field effects on the antennas' patterns.

The power delay profile can be classified as *dense* or *sparse* channels as defined by Molisch in [44]. Dense channels are commonly encountered in environments with high number of scatterers surrounding the receiver. In these dense channels, the interarrival time of MPCs is smaller than the resolvable time binwidth. In contrast, for sparse channels, the interarrival time of echoes is larger than the resolvable binwidth which could lead several consecutive binwidths without significant power. Since the temporal binwidth is given by the inverse of the channel bandwidth, the categorization of the channel into dense or sparse depends not only on the propagation properties of the environment, but also on the channel bandwidth considered in the characterization.

Two different NLOS locations with respect to a common receiving point were subjects of this study: an office environment and an auditorium. The main features to measure in both propagation scenarios, which determine the selection and design specification for the channel sounding platform, can be summarized as follows:

- The channel joint AoA-ToA complex impulse response has to be measured for both polarizations at the receiver location;
- The study is limited to vertically polarized transmitted signals;
- The cross-polarization of MPCs and its dependence on the AoA must be measured;

- The chosen frequency range for the channel characterization is 5.10-5.85 GHz due to its relevance to current and future high-speed WLAN applications;
- The proximity and distribution of scatterers surrounding the transmitter and receiver in both locations determine a MPC temporal resolution better than 5 ns;
- Magnitude and phase of MPCs must be measured in order to estimate the effects of coherent vs. non-coherent multipath combination at the receiver; and
- The channel must be characterized with a resolution better than 10° in azimuth and elevation in order to be able to use the CIR snapshots to reconstruct a high resolution channel representation (Chapter 4).

3.3 VIABILITY STUDY OF THE DIFFERENT CHANNEL SOUNDING TECHNIQUES

The channel sounding techniques considered for this experiment can be grouped in three categories [57]:

- Direct pulse channel sounding;
- Spread spectrum sliding correlator sounding; and
- Frequency domain channel sounding.

The selection was determined by the indoor channel characteristics and the accuracy required in characterizing these parameters. In our case, the spatial and temporal multipath distribution had to be measured. Consequently, an antenna system was required to scan the indoor channel in different directions, minimizing the distortion due to the coherent addition of multipath arriving from distinct AoAs. The other important requirement involved the independent measurement of both orthogonally polarized MPCs. Finally, the specification of temporal resolution and capture time had to match the propagation specifications of indoor environments already mentioned.

3.3.1 DIRECT PULSE SOUNDER

One of the simplest, although not widely used, channel sounding techniques is the direct multipath magnitude vs. delay measurement [42]. This radar-like technique consists of the transmission of a modulated train of pulses with duration of T_b s and rate of $1/T$ Hz. The received multipath signal is then amplified and demodulated using an envelope detector with a BW of at least $2/T_b$ Hz. The resultant baseband signal can be displayed and stored using a sampling oscilloscope. Figure 3.1 shows a diagram of the direct pulse channel sounding system. The signal received is the channel impulse response convolved with the baseband pulses. When it is available at the instrument location, the oscilloscope can be triggered using the baseband train of pulses generated at the transmitter side, thereby avoiding loss of synchronization due to signal blockage or interference. Averaging the signal provides a direct measure of the magnitude of the received multipath signal as a function of the delay.

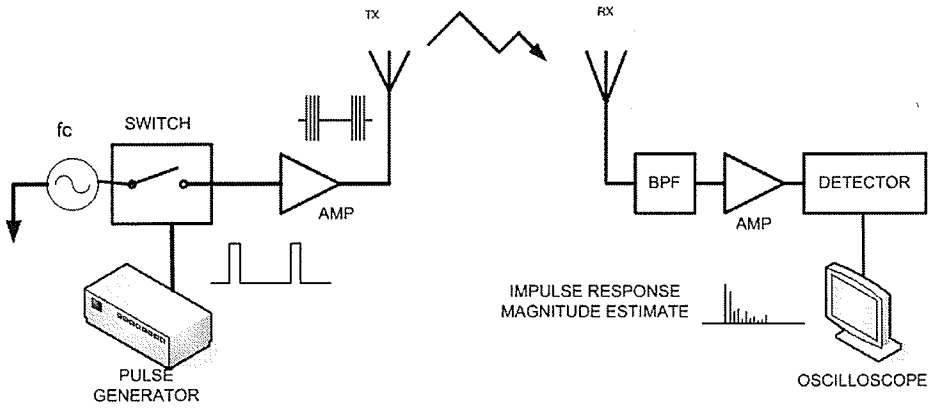

Figure 3.1. Direct pulse channel sounding technique.

The delay resolution of this method is given by T_b while the signal capture time is given by the pulse train period T. According to the propagation characteristics of indoor channels, it is necessary to generate a signal with T_b shorter than 5 ns and T on the order of 200 ns to properly characterize the channel. In addition to these specifications for the sounder signal, wideband detectors and oscilloscopes are also required. This method was used by Saleh and Valenzuela [62] to measure the indoor propagation channel in office environments at 900 MHz.

Despite the evident simplicity of this radar-like system, which is its main advantage, this method is not widely used. The most important disadvantage is the use of wideband receivers, which decrease the signal-to-interference ratio (SIR) thereby significantly reducing the sensitivity of the system. The phase of the received signal cannot be measured, but this limitation can be overcome by replacing the envelope detector with a coherent one. Another obstacle for this method lies in the generation of short pulses with enough energy to overcome the high path losses typically found in indoor environments [42].

3.3.2 SPREAD SPECTRUM SLIDING CORRELATOR SOUNDING TECHNIQUE

This technique is based on the direct-sequence spread spectrum (DSSS) technique to disperse a continuous wave (CW) signal over a large bandwidth by mixing it with a baseband pseudo-noise (PN) signal. The signal is received and de-spread using a PN sequence with a slightly slower chip rate. Whenever both PN sequences are aligned, maximal correlation occurs and the received signal can be de-spread and the envelope of the de-spread signal can be displayed on an oscilloscope (Figure 3.2). The signal detected is the channel impulse response convolved with the baseband PN signal. On the other hand, when both PN sequences are misaligned, the received signal is spread again by mixing it with the PN sequence generated at the receiver side and therefore most of the signal is eliminated by the narrowband filter in cascade with the receiver mixer. By adjusting the receiver chip rate, signal alignment will occur at shifted times delays, producing a temporal scanning of the received multipath signal. This technique was used by Bultitude [3], [5] to characterize the indoor channel scenario similar to the one that was chosen for our experiment.

One of the advantages of using this technique is that the signal can be detected by a wideband mixer in cascade with a narrowband receiver, eliminating the need for wideband receivers. Therefore, the dynamic range of the system is improved in comparison with the direct pulse method by reducing the noise and interference. The processing gain of the system is given by

$$P_{gain} = \frac{2f_c}{f_b} \tag{3.1}$$

where f_b and f_c are the PN chip frequencies at the receiver and transmitter, respectively. Depending on the values of f_b and f_c in (3.1), the physical coverage can be increased for the same transmitter power, or equivalently, the required transmitter power for a given area can be reduced.

There are some obstacles the implementation of this technique. The multipath amplitudes at different delays are not acquired in real time. So, when the coherence time of the channel is small, consecutive multipaths might be measured after the channel has changed. Similarly, the sweep time implies that the phase of different multipaths is measured at different times. Again, if the channel changes during the acquisition time, the readings are likely to be invalid. However, in the case where the channel is static, which can be assumed as a good approximation for the channel measured in this study, the sliding correlator technique can still be applied. The complexity of the hardware needed to build a spread spectrum channel test bed with the required temporal resolution was a critical factor in the implementation of this method.

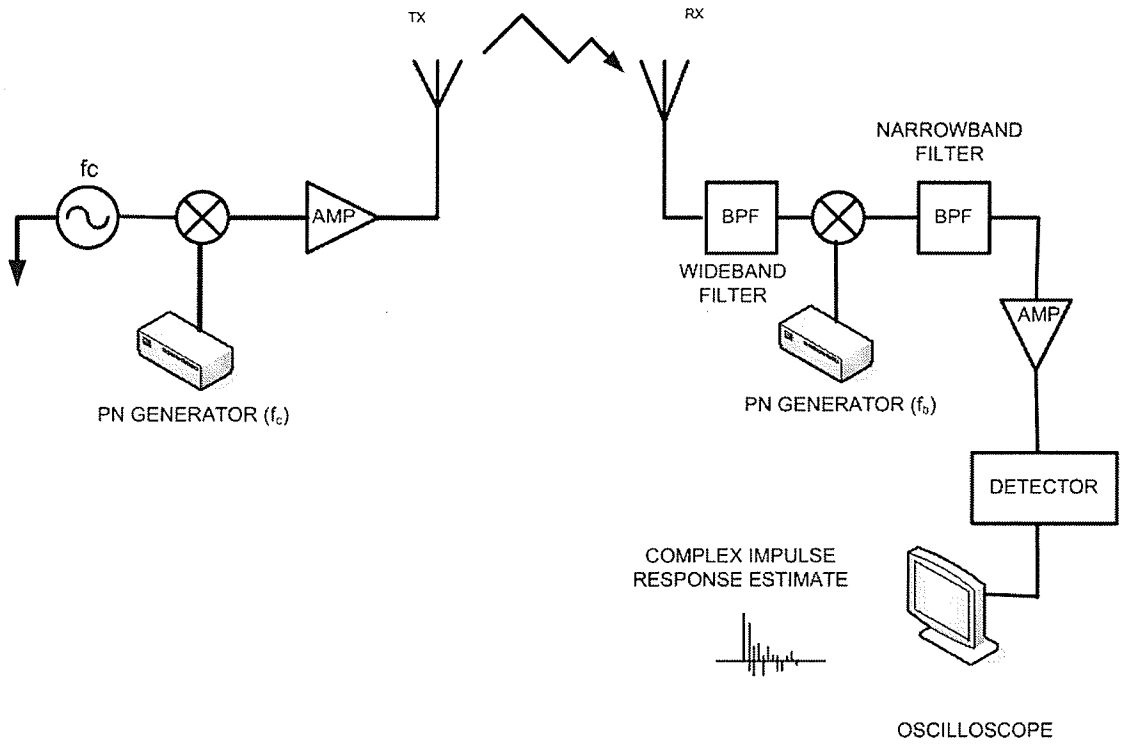

Figure 3.2. Spread spectrum sliding correlator sounding technique.

3.3.3 FREQUENCY DOMAIN CHANNEL SOUNDING TECHNIQUE

The next sounding technique considered is based on the measurement of the CIR in the frequency domain. The time domain impulse response can be obtained by postprocessing the frequency domain data. In this case, the transmissivity S_{21} parameter is measured in the frequency domain using a VNA as shown in Figure 3.3. A CW is swept in discrete steps over the chosen frequency band while the received multipath signal is detected by the same instrument. The magnitude and phase of the received signal are

compared with the transmitted CW and the CIR is then estimated for each discrete frequency step.

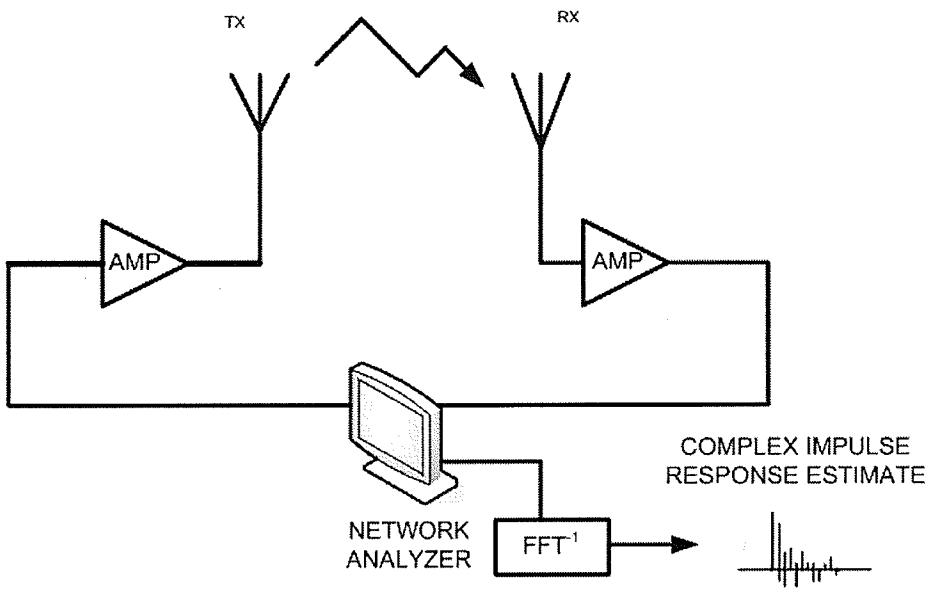

Figure 3.3. Frequency domain channel sounding technique.

The main advantage of this method lies in its inherent simplicity. The VNA acts as the receiver and transmitter, and provides synchronicity between input and output ports. However, in order to ensure a valid reading, it is crucial to calibrate the system properly. The complex channel gain is directly measured by the instrument, which means that amplitude and phase information can be retrieved directly. One inherent problems of the method is the limited achievable measurement range, since the transmitter and receiver have to be hardwired to the VNA. The frequency sweep rate has to be adjusted to be fast enough to complete a measurement within the channel coherence time. This can be done by reducing the number of frequency steps or by reducing the frequency range sweep, reducing the total capture time or the multipath delay resolution, respectively.

This technique allows the accurate measurement of both magnitude and phase with the temporal resolution required to characterize the indoor channel. In this study, the channel is static, therefore the sweeping time and the number of frequency step, is not a limiting factor. Thus, the number of frequency steps can be sufficiently high to match the specifications for the signal excess delay. Note that the frequency step size determines the maximum capture time which, in this case has to be larger than 200 ns as a consequence of the delay expected between transmitter and receiver locations (Section 3.1).

3.3.4 EFFECTS OF THE RECEIVER ANTENNAS ON THE INDOOR CHANNEL MEASUREMENT

The antenna radiation pattern leads to distortion in the reception by weighting the MPCs arriving differently, depending on the AoA. In addition, high multipath delay resolution requires a high BW. Note that an antenna with a BW of at least 500 MHz is necessary to obtain ~4 ns time resolution after applying a window to the time-domain signal in order to reduce the sidelobe effects, a process called windowing. This *windowing* increases the effective time binwidth, decreasing the delay resolution. Furthermore, the antennas suitable for the task normally have slightly different radiation patterns at different frequencies making the problem even worse.

The characterization of the AoA for the multipath signals can be achieved by using highly directional antennas to scan the indoor environment [21]-[23], [66], synthetic aperture radar techniques [31] or antenna arrays [29]. The synthetic aperture radar uses a single antenna that is mechanically moved to different positions in a *virtual array*. The

signal captured at each position is post-processed to scan the main beam to the desired direction. In order to obtain valid results, it is necessary to assume that the channel remains static during the whole capture cycle. For a real array, the signal received by each antenna element of an array is also weighted and then combined to achieve the scanning of the main beam towards the desired AoA. However, the main difference with the synthetic aperture radar method is that the processing occurs in *real time* which allows the capture of fast changing channels. However, a large number of antenna elements are required to achieve resolutions on the order of less than tens of degrees, which can be an obstacle at certain frequencies for indoor measurements due to the physical dimensions of the arrays. The electronic scanning of the main beam when using arrays creates sidelobes in undesired directions, resulting in signal distortion due to the coherent addition of interfering MPCs coming from different AoAs. The use of directive antennas mechanically oriented towards different AoAs offers the advantage of guaranteeing a *direction-independent* radiation pattern, provided that the antenna dimensions are small enough to minimize interactions with the indoor clutter. At higher frequencies the physical dimensions of the antenna are smaller and it is more likely that an antenna with the BW required for the temporal resolution specified can be found.

One approach to diminish the antenna distortive effects in the measured signal is deconvolution of the radiation pattern. The CLEAN algorithm [1], [42], [66] and its variants [2] were proposed in previous works to determine the AoA of MPCs with high resolution and to eliminate the erroneous location of MPCs. Another approach is using an array of antennas, whether *real* or *virtual*, instead of a single antenna [42]. This is the typical scenario in which the SAGE algorithm is used to extract MPCs from the complex

weighted combination of the received signal by each antenna element. Both approaches assume planar wave fronts at the receiver side.

3.4 SELECTION OF THE BEST CHANNEL SOUNDING METHOD

After weighing the advantages and disadvantages of the different techniques against the specified requirements (Section 3.1), the frequency domain sounding technique was chosen to characterize the AoA vs. the ToA of the indoor multipath channel. The CIR is measured in the frequency domain by means of a VNA shown in Figure 3.4. The only addition to the method was the capability of mechanically scanning a narrow beam antenna to the desired directions. The positioning platform built for that purpose was designated as AZELTI, an acronym of Azimuth-Elevation-Time channel sounding platform. The time resolution achieved using this method was better than 3 ns, allowing the resolution of multipaths with a path difference as short as 90 cm. A block diagram of the channel sounder is depicted in Figure 3.5.

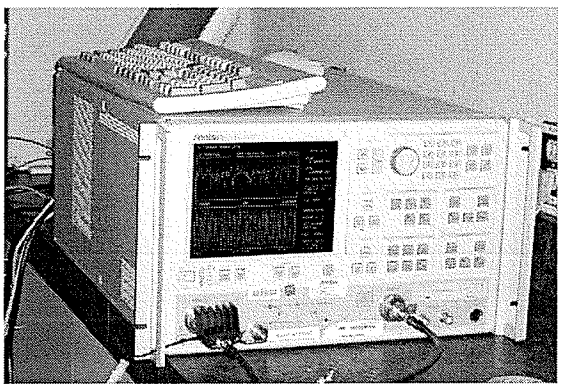

Figure 3.4. Anritsu 37347c vector network analyzer.

The use of a mechanically scanned antenna guarantees the same spatial response independent of the scan angle. Hence, the main advantage of selectively capturing snapshots by mechanically scanning the receiver antenna resides fundamentally in the reduction of interference caused by MPCs coming from undesired AoAs that would interfere with the desired signal. Using other scanning techniques, distortions in the measured signals due to undesired sidelobes in the radiation pattern as a function of the scanning angle make it more difficult to obtain a correct measurement of the CIR. This angle invariant antenna response that is only a function of the sample frequency is maintained as long as the planar incident wavefronts assumption is valid (Section 2.3). This consideration eases the postprocessing of the measured CIR, allowing the reconstruction of a high resolution representation of the indoor radio channel for vertical and horizontal received polarizations.

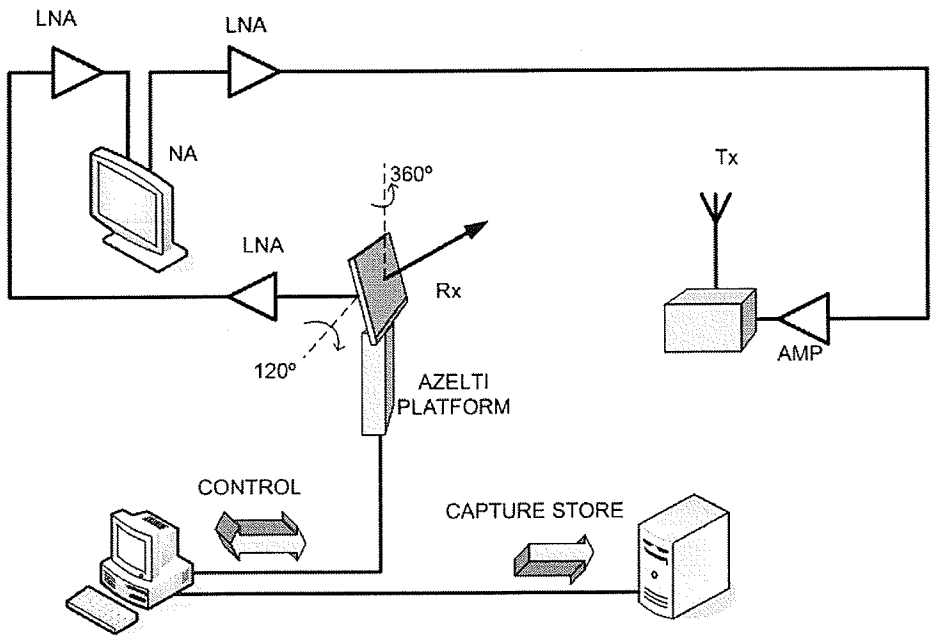

Figure 3.5. Channel sounding setup.

In order to minimize the likelihood of false readings during the channel measurement, the AZELTI platform was built using polyvinyl chloride (PVC), wood and silica, reducing the interactions between the platform and the measured electric field at the desired frequencies (Figure 3.6). Table 3.1 summarizes the specifications for the channel sounding method described in this section.

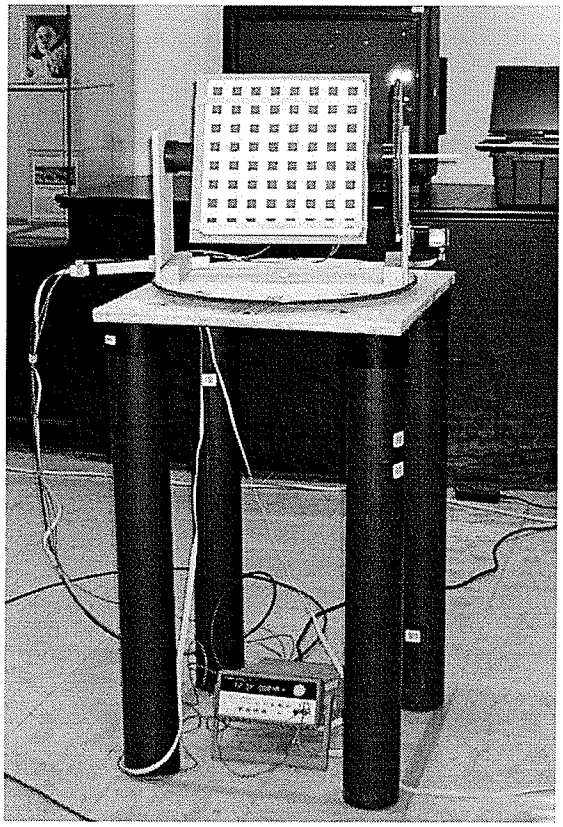

Figure 3.6. AZELTI acquisition platform showing the planar array antenna mounted in the positioning platform.

Table 3.1. Channel sounding specifications.

Frequency Sweep Range	5.100-5.850 MHz
Frequency Sweep Step	1.875 MHz
Azimuth Sample Step	5°
Elevation Sample Step	5°
Azimuth Scanning Range	0°-355°
Elevation Scanning Range	25°-155°
Elevation Used Sample Range	30°-150°
Number of Samples	400 samples
Binwidth	~3 ns
Windowing	Blackman-Harris (1 term)
Maximum Excess Delay Resolution	533 ns
CIR Average	5 channel snapshots
Sweep Time	5 s

3.4.1 TRANSMITTER AND RECEIVER ANTENNAS

The vertically polarized biconical antenna shown in Figure 3.7(a) was used as the transmitter antenna providing an omnidirectional illumination of the indoor environment. The BW of this antenna covers the frequency range of 2-10 GHz. A CW was transmitted from the chosen test locations, indicated in Figure 3.11 as locations A and B. The CW was swept across the BW of interest in 1.875 MHz frequency steps.

The receiver patch antenna was a square planar array of 8 by 8 elements with a pencil-like radiation pattern, 10° half-power beamwidth (HPBW), -20 dB sidelobe levels, and 1 GHz BW. The receiver antenna is illustrated in Figure 3.7(b). The antenna characterization was done by the CRC's Advanced Antenna Technologies division in an anechoic chamber for frequencies ranging from 4.850 GHz to 5.850 GHz with 50 MHz steps (Appendix A). The co-polarized planar array antenna radiation pattern in the E- and H-planes as functions of frequency is illustrated in Figure 3.8. In these figures, 0° is the direction parallel to the plane of the array and 90° indicates the direction perpendicular to the center of the array. The receiver antenna exhibits a cross-polarization rejection better than 20 dB for the range of scanning in both planes in the frequency range of interest (Figure 3.9).

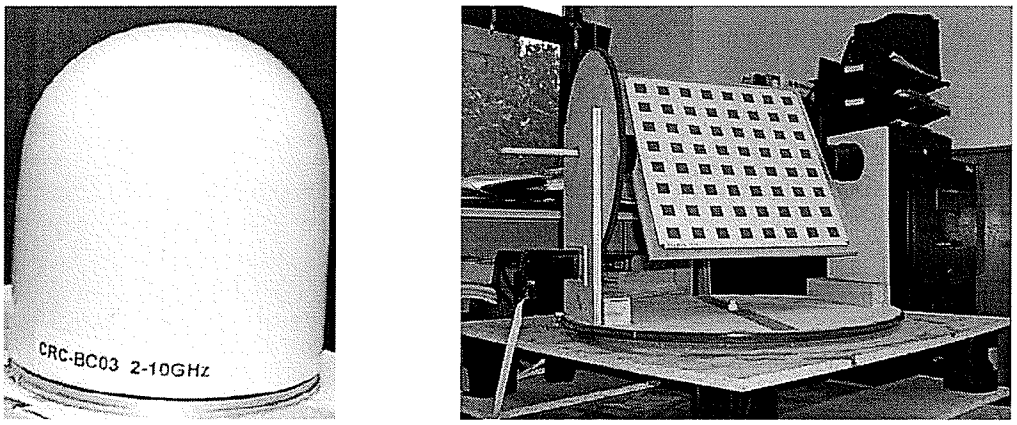

Figure 3.7. (a) Transmitter antenna (biconical, omnidirectional), (b) Receiver antenna (8x8-elements planar array, directive).

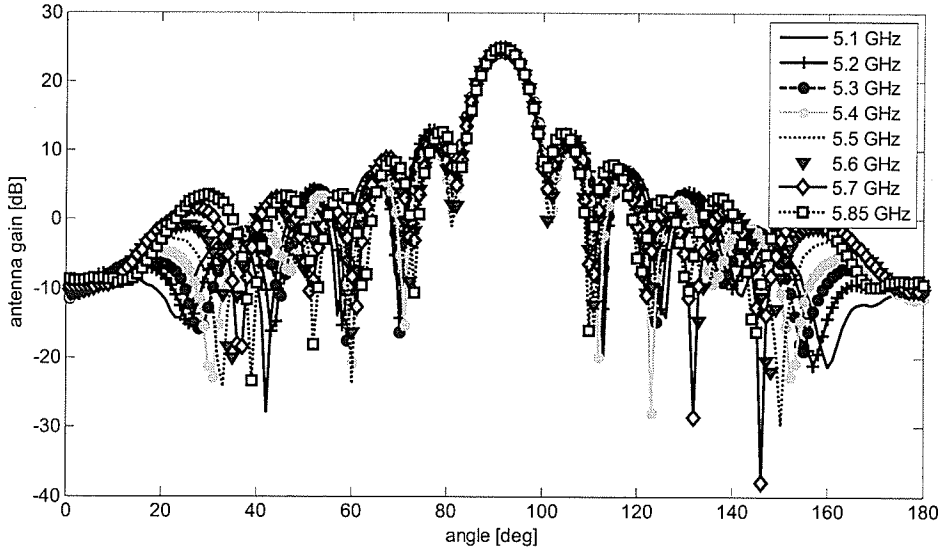

(a) E-plane.

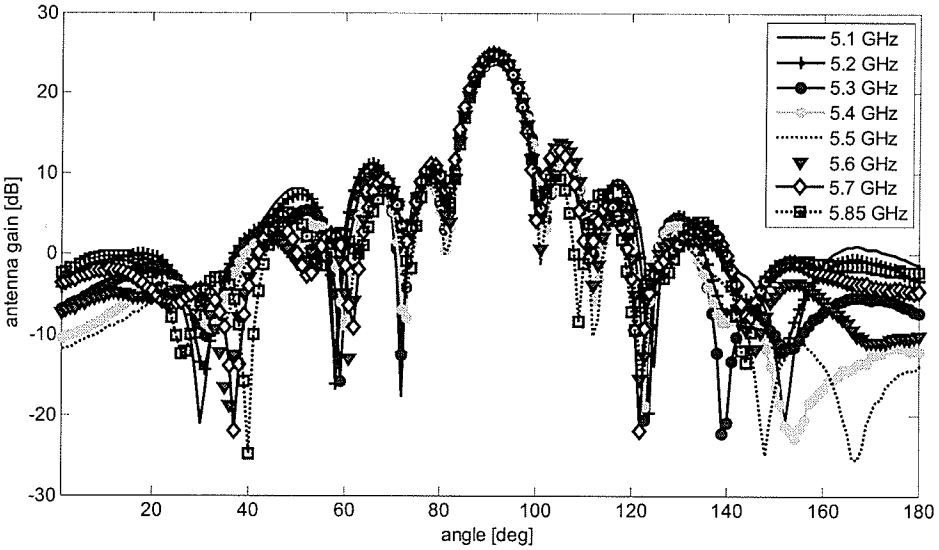

(b) H-plane.

Figure 3.8. Receiver antenna radiation patterns.

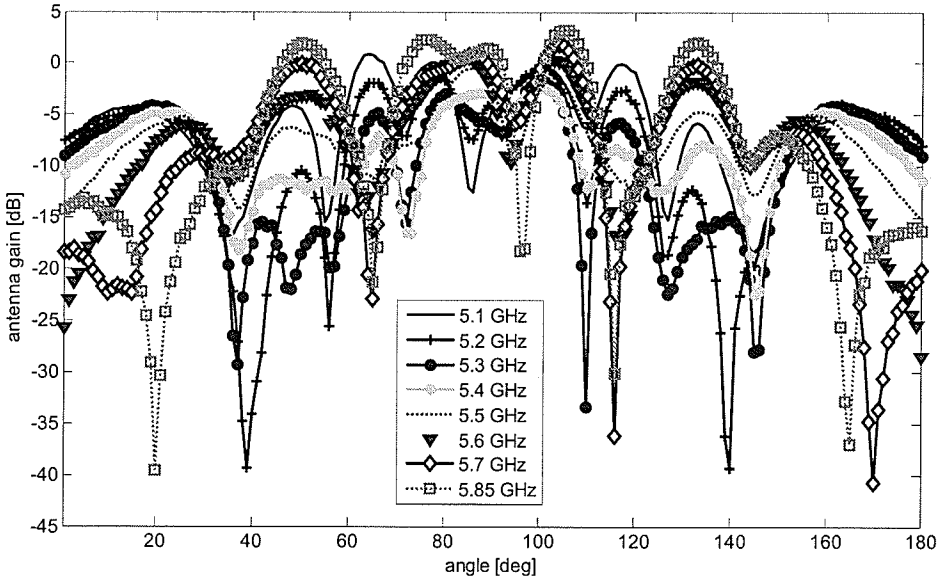

(a) Cross-polarization rejection (E-plane).

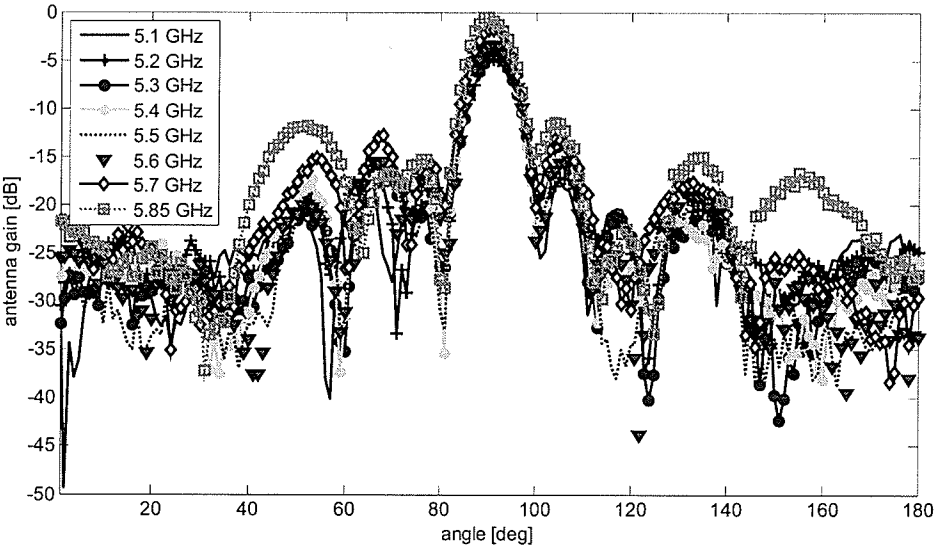

(b) Cross-polarization rejection (H-plane).

Figure 3.9. Receiver antenna cross-polarization rejection.

Special consideration was made to diminish the near-field effects caused by the indoor clutter in the receiver surroundings. Figure 3.13 shows details of the scatterers' distribution in the receiver location and their relative distances to the antenna. Based on simulation results [53] it was possible to characterize the receiver antenna near-field limits as a semi-spherical area of 90 cm radius surrounding the planar array. The location of any possible scatterers around the receiver in the main lobby was far beyond that threshold for the chosen scanning angles. Thus, it was assumed that the shift invariance of the antenna radiation patterns was maintained for all the scanning angles.

At the receiver side, a PC-controlled system positioned the wideband antenna to the desired azimuth (φ) and elevation (θ) angles. In the system of coordinates used shown in Figure 3.10, $\theta = 90°$ corresponds to the horizontal plane *xy*. The scanning was performed from 0° to 355° in φ and from 30° to 150° in θ, both in steps of 5° for both polarizations. The electric field in θ and φ directions were measured and used by the VNA to calculate the magnitude and phase of the CIR in both orthogonal directions.

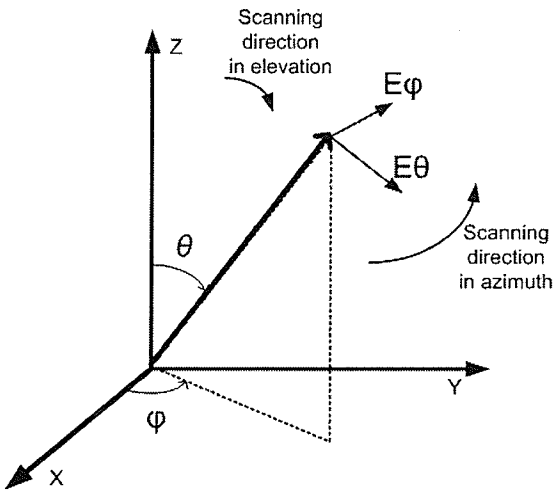

Figure 3.10. Reference system for the CIR acquisition.

3.5 MEASUREMENT LOCATIONS

The two NLOS locations chosen for this experiment are shown in Figure 3.11. The selection of location A was made based on the distribution of potential scatterers around the receiver area while location B was chosen to study the propagation from a typical office space scenario.

Location A is an auditorium with folded metallic chairs and plenty of potential scatterers. On the other hand, location B is a fully furnished office space which represents a completely different environment for radio propagation. Heating ducts, pipes and electric wires run above the ceiling. Double layer plywood, concrete and brick walls, steel reinforced concrete columns as well as typical office equipment are present close to transmitter location B. Dozens of metallic folded chairs are present in transmitter location A. The receiver area of influence is depicted in Figure 3.12 while details of the main sources of scattering are indicated in Figure 3.13(1)-(6). The distinctive characteristic of a real indoor scenario in comparison with a simulated environment commonly used in ray-tracing simulations lies in the effects of many potential scatterers such as indoor clutter, structural details, etc. In order to have maximum control over the variables that could affect the channel measurement, the tests were conducted during the weekend when the traffic of personnel in the test area was minimum.

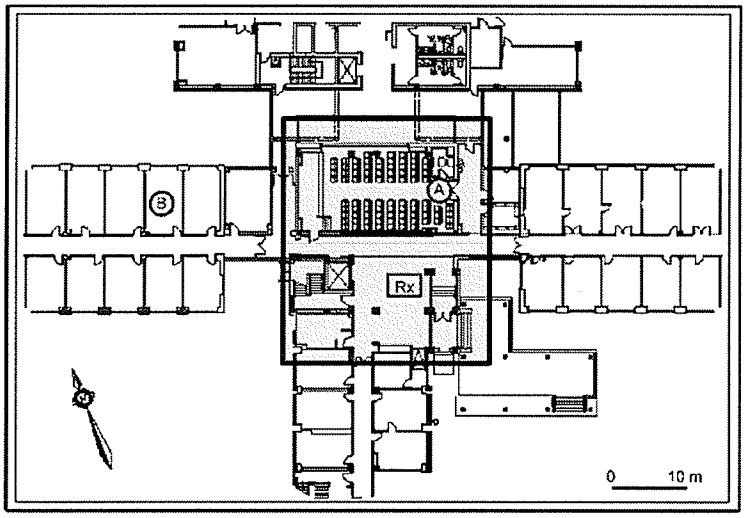

Figure 3.11. Receiver location (Rx) and transmitter locations A and B. The receiver area of influence is highlighted.

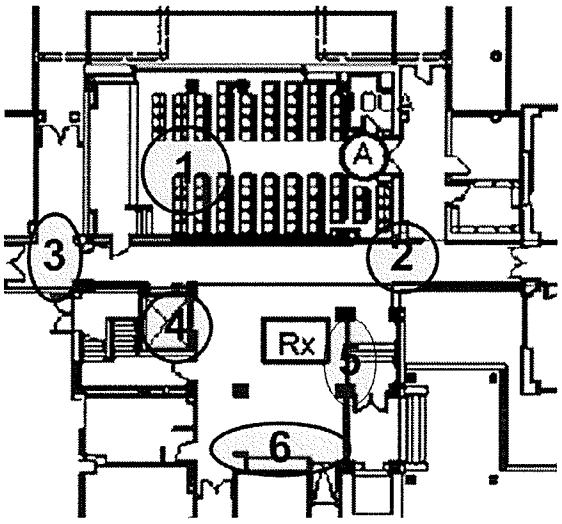

Figure 3.12. Receiver area, highlighting some of the areas of interest.

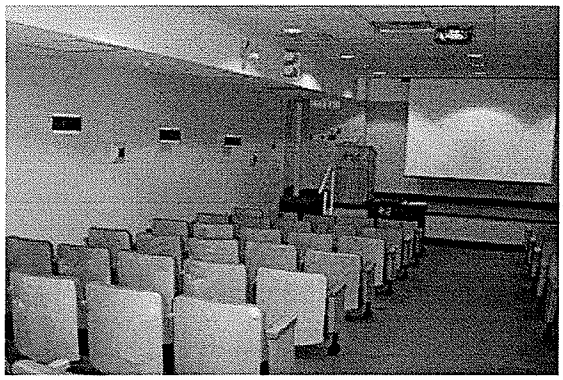

(1). Details of metallic folded chairs inside the auditorium (Location A).

(2). Hallway that connects the auditorium and the main lobby where the AZELTI platform was located.

(3). Hallway that connects the office (Location B) and main lobby.

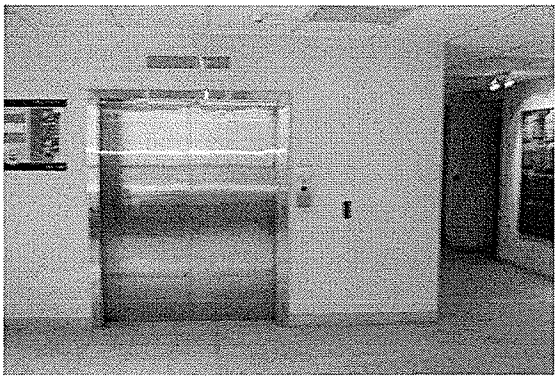

(4). Elevator metallic doors (2.45 m from the receiver) and hallway corner to offices.

(5). Front wall (4.15m from the receiver) with metallic plaques that separates the main lobby from the auditorium (Location A).

(6). Back wall (3.25 m from the receiver) that separates main lobby from a washroom where metallic scatterers are located.

Figure 3.13. Details of the scatterers shown in Figure 3.12.

3.6 DATA ACQUISITION

Five channel snapshots were acquired at each look angle, and then stored automatically. The whole process was monitored remotely to reduce the chances of perturbing the channel measurement. The snapshots of the channel were acquired at half of the HPBW, obtaining four correlated sets of realizations of the CIR. These data set is further used to extrapolate a high resolution spatial-temporal estimation of each CIR using deconvolution techniques (CLEAN) and 2-D signal processing (Chapter 5).

The indoor channel was scanned two times, once for each polarization. The time invariance of the channel guarantees the validity of the reading for each polarization and AoA. Vertically and horizontally polarized components of the CIR were obtained from the two readings for each AoA. The horizontally polarized component was directly measured by the AZELTI platform with the receiver antenna in a horizontal polarization position (TE polarized plane wave). However, the vertically polarized component of the CIR was estimated from the elevation component of the measured CIR (TM polarized plane wave). The relationship between those magnitudes can be expressed as follows

$$\begin{bmatrix} h_V \\ h_H \end{bmatrix} = \begin{bmatrix} \sin\theta \\ 1 \end{bmatrix}^T \begin{bmatrix} h_\theta \\ h_\varphi \end{bmatrix} \tag{3.2}$$

where h_V and h_H are the vertical and horizontal components of the CIR, respectively, h_θ and h_φ are the measured elevation and azimuth components of the CIR, respectively, as

shown in Figure 3.10. In this context, it is not necessary to transform the measured signal from a spherical coordinate system into a rectangular one. The horizontally polarized component is directly measured as a function of the AoA by means of physically scanning the antenna and only a correction due to the projection of the vertically polarized component over the planar array is necessary. Hence, for $\theta = 90°$, the vertically polarized component is measured directly as a function of the scanning angle.

The CIR snapshots in the frequency domain were used to obtain the time domain impulse response as a function of each AoA scanned. Figures 3.14 and 3.15 show the channel frequency and time domain response, respectively, for $\theta = 90°$ and $\varphi = 0°$ for Location A. The data thresholding used in the experiment to discriminate MPCs was the CFA method adapted from the method proposed by Sousa [62]. The signal thresholding method is explained in Section 2.5.

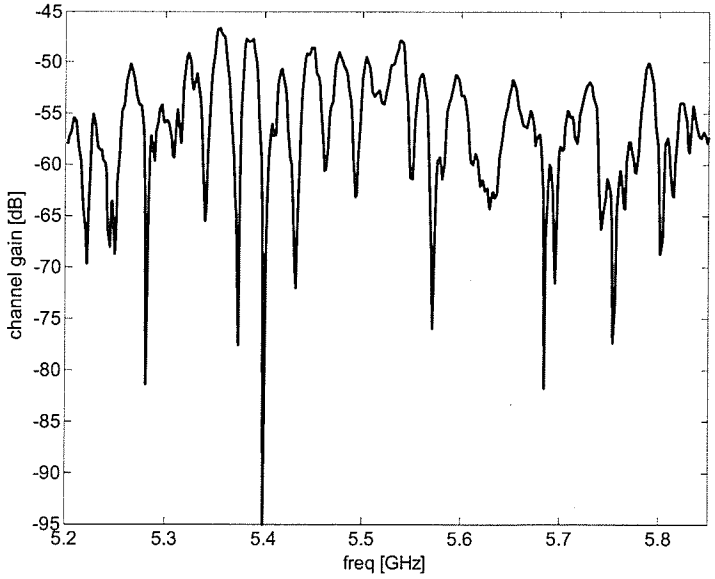

Figure 3.14. Frequency-domain measured channel gain for Location A at $\theta = 90°$ and $\varphi = 0°$.

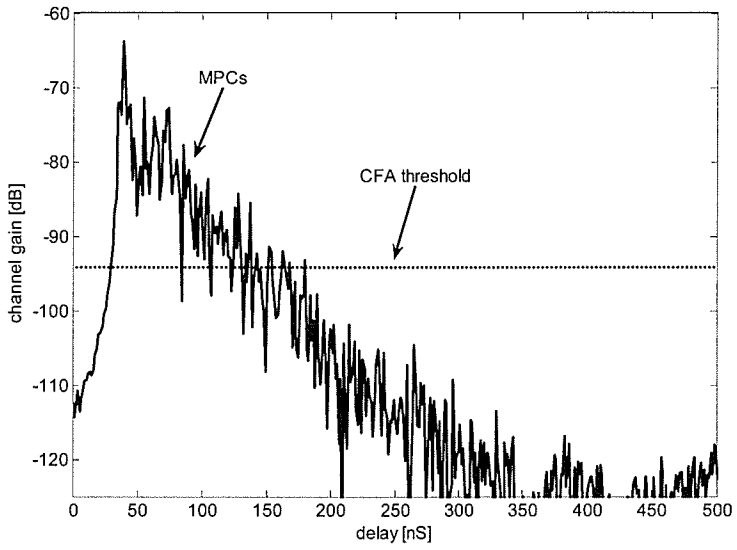

Figure 3.15. Time-domain estimated channel gain for Location A at $\theta = 90°$ and $\varphi = 0°$.

3.7 CALIBRATION

Hardware calibrations followed by a data calibration were performed before the start of the channel measurement. The hardware calibration involved calculating the delay compensation for coaxial cables, amplifiers, attenuators, and connectors used to connect transmitter and receiver platform to the VNA. Figure 3.16 shows the short circuit calibration connections. The antenna gains were characterized individually for the operative frequency range. In order to simulate the free space attenuation and, at the same time, to protect the VNA from a power overload during the calibration process, attenuators of 30 dB (location A) and 60 dB (location B) were used as pass-through connections between transmitter and receiver lines. These attenuators were characterized

individually and their frequency responses were used to compensate the CIR measurement afterwards.

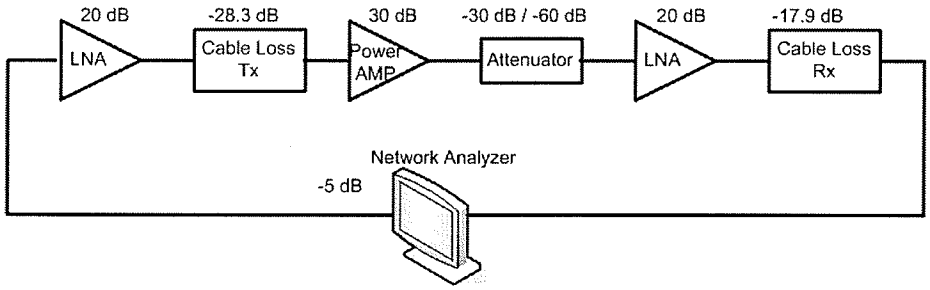

Figure 3.16. Network analyzer hardware calibration scheme.

The data calibration was made in LOS at the receiver final location. This strategy was adopted since location of the transmitter and receiver antennas and the scatterers around the receiver impact the measurement results.

3.8 SUMMARY

In this chapter the channel platform specifications in terms of the characterization of indoor channels were discussed. The different viable techniques used in the literature were contrasted against the requirements and from this analysis the AZELTI platform was designed and built. The transmitter antenna was selected to provide an omnidirectional, linearly polarized illumination of the locations selected for the test. In contrast, the receiver antenna was selected by its *pencil-like* radiation pattern. The

receiver's radiation pattern in the frequency band of interest was presented for E- and H-plane as well as its cross-polarization rejection performance. The calibration of the sounding platform was discussed and the data model for the complex impulse response as function of the scanning angle was presented.

4 RECONSTRUCTION OF THE CHANNEL RESPONSE ESTIMATE

4.1 INTRODUCTION

The large amount of information obtained after the measurement of the indoor wireless channel can be organized as a sequence of *images* representing the CIR as a function of the angle of arrival (AoA) and delay. This strategy facilitates organizing and processing the acquired data more efficiently enabling the posterior analysis and extraction of channel parameters from the analysis of the generated images. Previous studies based on measurement campaigns reported that MPCs appear in joint spatio-temporal clusters [66]. The precise characterization of these power clusters will help to improve the proposed space-time models for indoor channels [48], [49]. However, the images obtained from the direct measurement of the CIR usually suffer from artifacts

caused by the physical limitations of the capturing device, which in this case is the receiver antenna. Examples of these physical limitations are unacceptably high sidelobe levels (SLLs) and excessively wide HPBW, both contributing to the distortion of the power pattern image. The mainlobe-to-sidelobe and sidelobe-to-sidelobe interactions introduce errors in the estimation of individual MPC's AoA leading to the shape distortion, incorrect location, or even cancellation of multipath clusters.

In this section, a technique for the reconstruction of an estimation of the CIR using a correlated set of channel samples will be introduced. The proposed method is a modification of the techniques used to estimate the channel response based on the deconvolution algorithms in [66], [67], [68]. While these previous attempts to estimate the AoA of MPCs were limited to the horizontal plane, the technique proposed is applied to 2D-datasets representing the azimuth-elevation AoA of multipath signals captured using the AZELTI platform (Section 3.4). Other deconvolution techniques were used in attempts to estimate the AoA of signals reflected from the targets, for radar-like applications [2]. The innovation of the approach chosen in this project lies in the use of a correlated set of data samples or images representing the complex channel response in both azimuth and elevation angles to estimate the indoor CIR. The number of samples of each data set is limited by the physical constraints of the acquisition sensor, i.e. the receiver antenna. Even though the number of samples of each image is insufficient to estimate the CIR with high resolution, the proposed procedure uses the combination of a set of channel realizations that, after post-processing, provides a more accurate joint AoA-ToA MPCs distribution. The post-processing consists of the upsampling and elimination of the undesired effects of the antenna that *blurred* each image. The

procedure developed to process the data acquired with the AZELTI platform can be summarized in three main conceptual parts:

- The upsampling of the image set, generating a new set of images blurred by both the antenna aperture size and the non-ideal antenna spatial response;
- The deconvolution of the antenna pattern of each image of the upsampled set to eliminate the *blurring* effects and to identify the AoA location of MPCs that were shadowed by the noncoherent addition of interference; and
- Finally, the reconstruction of a single image representing the CIR estimate.

The techniques presented here are not restricted to indoor channel reconstruction and have applications in diverse radio image processing problems such as the reconstruction and identification of radar target images [2] and microwave imaging [70].

In Section 4.2, the use of lattice structure to model image sampling is described; this is used in Section 4.3 to reconstruct an estimate of the CIR along with the introduction of the CLEAN procedure. In Section 4.3.3, a method to update the feedback coefficient at each recursion of the deconvolution procedure is presented. Thanks to this optimization of the CLEAN algorithm, the computation time and the likelihood of errors in the resultant MPC's AoA estimate were reduced. Examples of the application of this technique are given in Section 4.4, and possible alternate approaches for the estimation method are proposed in Section 4.5.

4.2 IMAGE GENERATION BASED ON THE MEASURED DATA SETS

The acquired samples of the channel power pattern consist of a set of 24 by 72 samples in elevation and azimuth angles, respectively. Figure 4.1 shows a representation of the 2-D channel gain at 5.10 GHz. There are 400 of these images covering the frequency band of interest (5.10-5.85 GHz) in frequency intervals of 1.875 MHz.

The scanning device spatial response, in this case represented by the receiver antenna radiation pattern, is shown in Figure 4.2 using a linear scale. In terms of the image processing, the antenna spatial response is going to be referred to the point-spread-function (PSF) in this analysis. As the receiver location was chosen by its relative distance to scatterers that could distort the antenna pattern due to near field effects, therefore, the shift-invariance of the PSF was guaranteed by the radiation pattern invariance with respect to the scanning angle (Section 3.4.1). However, the antenna exhibits variations in SLL and HPBW in the frequency range of interest as shown in Figure 4.3. Each image, which is associated to a different sample frequency, is processed independently. Therefore, a different PSF was employed to process each image depending on the sample frequency. The shift-invariance property of the PSF holds for each image regardless of its frequency dependence. It is important to remark that the PSF maintains its central symmetry along the BW of interest, acting as a zero-shift filter, thereby complex signals maintained their phases and only their magnitudes changes.

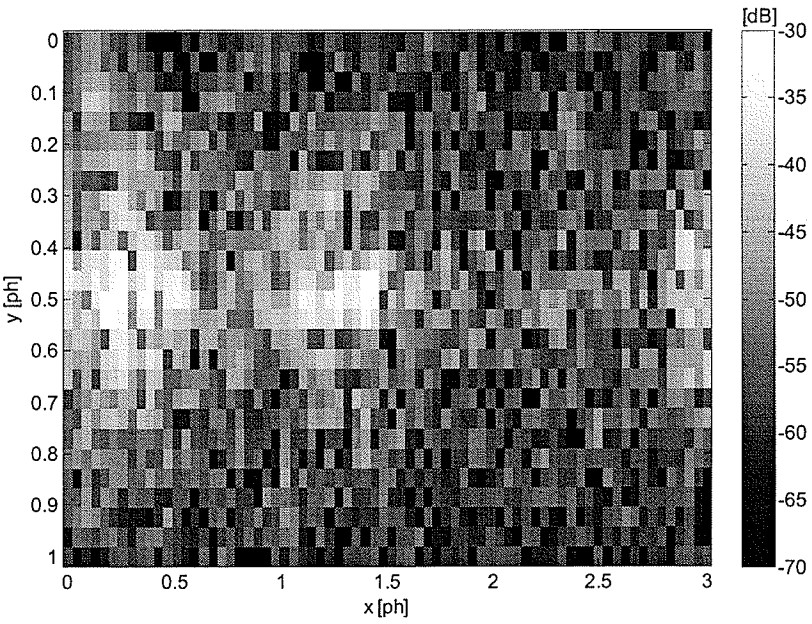

Figure 4.1. CIR as a function of the angle of arrival at 5.10 GHz.

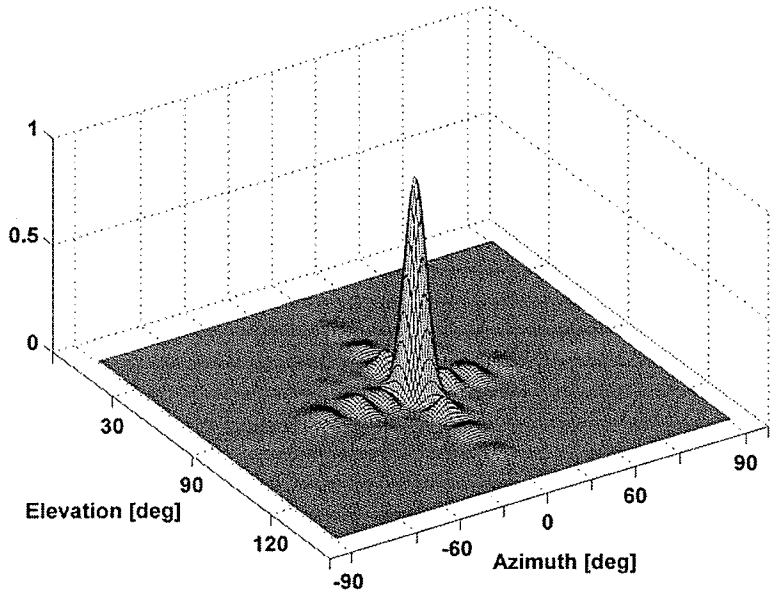

Figure 4.2. PSF as a function of the AoA at 5.10 GHz (linear scale).

In order to be consistent with the image processing literature, the chosen units for the images dimensions is in picture heights (*ph*). The aspect ratio (*ar*) of an image is a dimensionless magnitude that can be defined as the ratio between the picture width (*pw*) to the picture height (*ph*) as

$$ar = \frac{ph}{pw} \tag{4.1}$$

where *ph* and *pw* are the picture height and width, respectively, in the same arbitrary units. The lattice will be used as the mathematical model for the sample structure (Appendix B). A comprehensive treatment of the lattice theory and its application in the sampling of multi-dimensional signals is given by Dubois [14] and also by Wang [71]. A rectangular lattice with a sample spacing equivalent to 5° in both azimuth and elevation angles can be used to model the sampling structure used to capture each image, i.e.,

$$\Lambda = LAT(V) = \left(\begin{bmatrix} X & 0 \\ 0 & Y \end{bmatrix} \right) \tag{4.2}$$

where Λ represents the lattice, $X = Y = 1/24\,ph$ represent sample spacing in picture height units of the channel taken over 360° (72 samples) and 120° (24 samples) in azimuth and elevation, respectively. Therefore, an image $ar = 360°/120° = 72/24 = 3$ will be maintained during the whole analysis. Note that, in order to make the visualization of the results clearer, the scale of the x and y axis is not the same in the images, given the impression of having $ar = 1$; however, the labeling for both axis clearly indicates the 3:1 relationship in *ph* units. A gray scale was chosen to represent the power at each sample point in the image, which has a dynamic range or image signal-to-noise ratio (ISNR) of

40 dB. Each sample point is correlated with the surrounding samples as a consequence of the receiver antenna aperture. The goal is not only to enhance the image representation of the measured data sets but to use these samples to generate a new image based on radio propagation principles and minimize possible errors in the estimation at the same time.

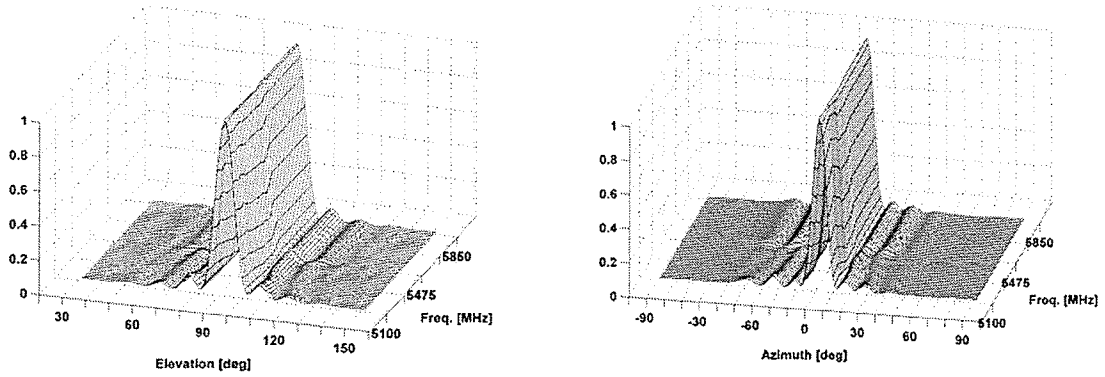

(a) E-Plane **(b) H-Plane**

Figure 4.3. Receiver antenna radiation patterns in the frequency range of 5.10-5.85 GHz (linear scale).

4.3 IMAGE RECONSTRUCTION

The spatial response of the capture sensor is symmetric $X = Y = 1/24\,ph$ (or equivalently, 5°) (Figure 4.4), in terms of the scanning lattice. In this study, the physical property that determines the sensor aperture is determined by the antenna HPBW. The scanning was performed using a rectangular lattice with X separation between samples. Since a pair of multipaths cannot be resolved when the difference in their relative AoAs is smaller than the PSF HPBW, the minimum spatial sample rate is determined by the

physical antenna aperture. This limitation can be explained by analyzing the PSF response relative to the sample structure Λ. When two sampled MPCs are close in Λ, let's say $(x+n_1, y+n_2)$, where $2 \geq |n_{1,2}| \geq 1$, the complex channel response measured is the result of the noncoherent addition of MPCs with distinct AoAs attenuated according to the PSF spatial response. For instance, the measured CIR when the AZELTI platform is scanned to a particular AoA will be the noncoherent combination of the signal arriving at (x, y) plus the undesired components at (n_1, n_2) attenuated according to their position relative to the center. Furthermore, the immediately adjacent samples, $(x\pm1, y\pm1)$, are correlated with the previous measurement due to the overlapping of the main beam of the PSF. In other words, the new samples will contain some of the previous adjacent samples noncoherently combined with the desired CIR for that AoA or sample point. This phenomenon is equivalent to an image captured by a charge coupled device (CCD) sensor with a capture area larger than the sample structure, e.g., an out-of-focus camera lens. The equivalent result in both examples is an image *blurred* by the effects of the capturing device. The interference problem described here takes into account the undesired interference of MPCs due to the main beam of the PSF. However, the sidelobes of the PSF in some cases can also be an additional cause of undesired interference during the capture process. This is not the case of the antenna selected for this experiment as can be seen from Figures 3.8 and 3.9. The deconvolution technique presented in Section 4.3.2 provides a method to mitigate the sidelobe and main lobe interference effects in the measurements.

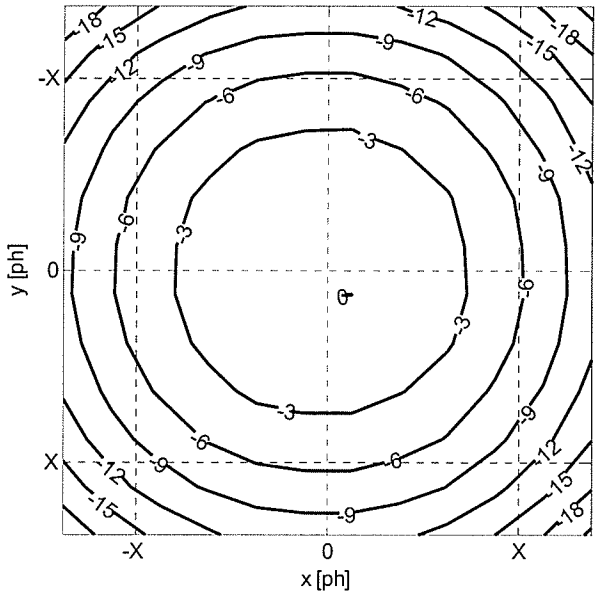

Figure 4.4. PSF in the space domain indicating the capturing sensor (receiver antenna) response in dB with respect to the main beam center (x,y) = (0,0) for Λ.

The oversampling undesired effect can be eliminated if, instead of considering a single image, the samples are de-interleaved into several sublattices with a smaller sampling density or equivalently with more spaced samples. Then, the problem is reduced to obtaining information from a set of independent images that each represents a distorted description of the CIR. Since the main beam response decays to -6 dB for X (Figure 4.4) and to about -20 dB for 10° (Figure 3.8) or $2X$ in terms of the lattice, it is possible to say that interleaving the image by one sample, the new images would consists of CIR samples that have very low correlation with their neighbours. Hence, four identical shifted sublattices of Λ can be defined for the purposes of independent image reconstruction; each of them represents a partial characterization of the CIR. Another reason to have $2X$ (10°) channel sample separation is related to the capability to correctly

identify the dominant MPCs in the iterative deconvolution process that will be explained in detail in Section 4.3.2. The sample sublattices in which the image will be decomposed can be expressed as

$$\Lambda_1 = LAT(V_1) = LAT\left(\begin{bmatrix} 2X & 0 \\ 0 & 2X \end{bmatrix}\right) = LAT\left(\begin{bmatrix} Z & 0 \\ 0 & Z \end{bmatrix}\right) \tag{4.3}$$

and, the shifted versions with respect to the original sampling structure Λ,

$$\Lambda_2 = LAT(V_2) = \begin{bmatrix} X \\ 0 \end{bmatrix} + LAT(V_1) \tag{4.4}$$

$$\Lambda_3 = LAT(V_3) = \begin{bmatrix} 0 \\ X \end{bmatrix} + LAT(V_1) \tag{4.5}$$

$$\Lambda_4 = LAT(V_4) = \begin{bmatrix} X \\ X \end{bmatrix} + LAT(V_1) \tag{4.6}$$

where $\Lambda_{1\text{-}4}$ are the sublattices, and the sample spacing for each sublattice is $Z = 2X = 1/12$ ph. Hence, the sample density of each sublattice $\Lambda_{1\text{-}4}$, defined as $det(\Lambda_{1\text{-}4})$ (Appendix B), is $1/4^{th}$ of the sample density of Λ. A comparison between the sublattices is shown in Figure 4.5. Each image defined on the sublattices $\Lambda_{1\text{-}4}$, will be upsampled to a higher density lattice, Γ, in order to achieve a 1° sampling rate in azimuth and elevation angles, or equivalently, a sample spacing of $X' = 1/120$ *ph* (Section 4.3.1). From each of these upsampled images, the PSF will be deconvolved after identifying the location of the MPCs in order to mitigate the effects introduced by the antenna radiation pattern (Section 4.3.2). The resultant set of reconstructed images will be added together to allow the interaction of interleaved complex samples.

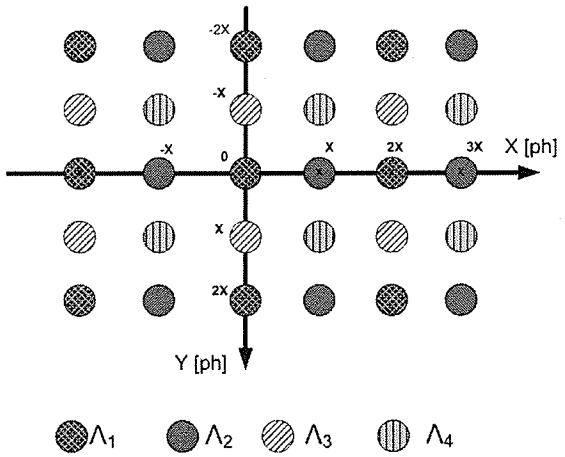

Figure 4.5. Sublattice sampling structures in which the original image is split indicating the sampling points that corresponds to $\Lambda_{1\text{-}4}$.

The proposed CIR reconstruction method is summarized in Figure 4.6 where f is the original image based on the captured data. The blocks labeled Λ_i, $i = \{1,2,3,4\}$, symbolize the reorganization of the data set into four, nonoverlapped images defined over each Λ_i lattices. The next blocks labeled with $\uparrow 10$ represent the upsampling of each image tenfold on each dimension. The blocks labeled CLEAN symbolize the deconvolution of the PSF. Finally, the channel response estimate, f_{est}, is the result of the noncoherent addition of the complex set of interleaved, deblurred images. Note that, f is used as the true CIR elsewhere.

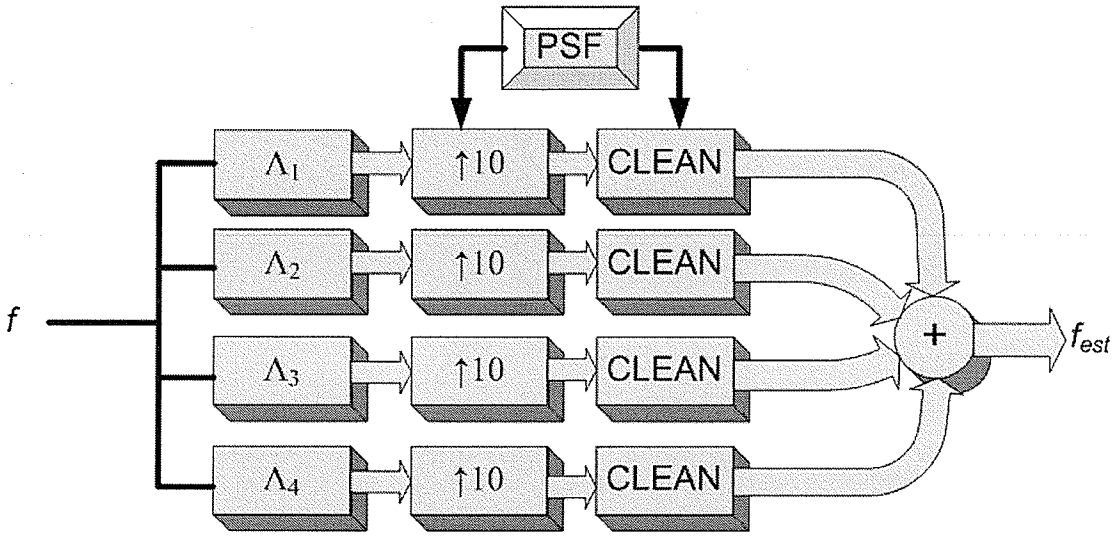

Figure 4.6. Block diagram of the CIR data set reconstruction.

4.3.1 UPSAMPLING OF THE INTERLEAVED DATA SETS

As described in the previous section, each image in Λ_i is used to reconstruct a CIR estimate for each of the 400 images, one per sample frequency. Note that the spatial frequency response of the resultant data set, which is treated as an image, is unknown at this point since the image will be the result of the noncoherent combination of four independent images generated *a posteriori*. Therefore, for the upsampling process it is assumed that each image is ideally limited to the low-pass frequency response of the PSF, which is the only parameter known at this point of the reconstruction. This assumption is important in the upsampling process to guarantee no aliasing effects in the resultant upsampled image. The 2D discrete Fourier transform for a signal defined on a lattice is defined in Appendix B as well as the reciprocal lattice for the frequency analysis.

The upsampling process consists of two parts:

- The interleaving of the image defined in each sublattice $\Lambda_{1\text{-}4}$ with zeros to new higher density lattices $\Gamma_{1\text{-}4}$ in order to obtain a sample density equivalent to 1° separation per sample; and

- The convolution of the signal on each nonzero sample point with a scaled version of the PSF in order to spread the energy over the neighbouring sample points of $\Gamma_{1\text{-}4}$ while maintaining the same total power.

As a result of the antenna spatial response, the complex signal detected at every sample point is the result of the noncoherent combination of MPCs coming from angles close to the scanning direction. In the upsampling process presented here, the complex signal, properly weighted by the PSF, is considered coming not from the particular sample point (x, y) but as the noncoherent combination of the spread signal coming from all the neighbouring lattice points in $\Gamma_{1\text{-}4}$. In other words, the result of sampling using the same sensor in the new higher density lattice $\Gamma_{1\text{-}4}$ for each interleaved point defined in the sublattices $\Lambda_{1\text{-}4}$ will be the same as the original collected complex value. The lattice $\Gamma_{1\text{-}4}$ can be expressed as

$$\Gamma = LAT(\Gamma) = LAT\left(\begin{bmatrix} X/10 & 0 \\ 0 & X/10 \end{bmatrix}\right) = LAT\left(\begin{bmatrix} X' & 0 \\ 0 & X' \end{bmatrix}\right) \quad (4.7)$$

where the sampling rate $X' = X/5 = Z/10$. Since the sublattices $\Lambda_{1\text{-}4}$ in which the original image has been divided have sample rate of $X' = 2X = 1/12$ *ph* as defined in (4.3)-(4.6), the new superlattices have $X' = 1/120$ *ph* sample rate, or in other words, one sample per degree in φ and θ. Figure 4.7 shows the rectangular sampling structure defined for the final image and Figure 4.8 shows the reciprocal lattice defined in Appendix B for the

spatial frequency analysis, where *c/ph* denotes cycles per *ph* and u and v are the horizontal and vertical spatial frequencies, respectively.

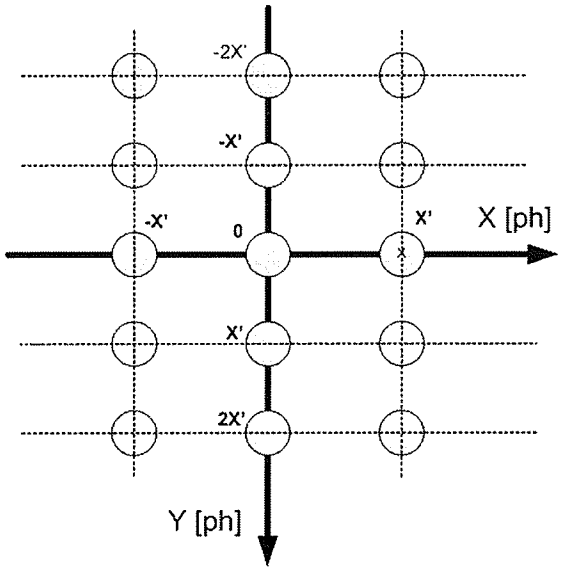

Figure 4.7. Sampling structure defined on lattice Γ_1 where the spatial sampling rate is X' = Z/10.

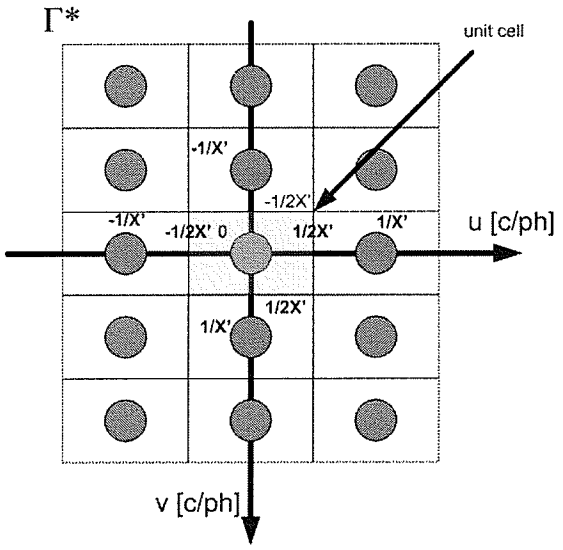

Figure 4.8. Reciprocal lattice defined for lattice $\Gamma_{1\text{-}4}$ indicating the unit cell in terms of X' = Z/10.

In the upsampling process, the complex signal of each non-zero valued sample point in Γ will be spread into the surrounding sample points defined by the new, high-density

lattice. This process could lead to aliasing if the PSF contains high spatial frequency components that overlap the neighbouring unit cells. The Fourier transform of the PSF is shown in Figure 4.9 indicating the 3 dB cut-off frequency with respect to the reciprocal lattice Γ^* for the u and v, horizontal and vertical spatial frequencies, respectively (Appendix B). Since the high spatial frequency components are delimited to the unite cell, which is defined for a rectangular lattice Γ as the area in Γ^* limited by $(u,v) \leq 1/2X'$. As can be seen in Figure 4.9, the PSF acts as a low-pass filter within the unit cell of the higher density reciprocal lattice, therefore there is no danger of aliasing. The PSF frequency response, indicated $H(u,v)$, and its relative location in the unit cell of Γ^* is illustrated in Figure 4.10. Note that the frequency distribution pattern is repeated periodically over all the points in the reciprocal lattice, however, for simplicity, only the one centered at (u,v) = (0,0) is represented.

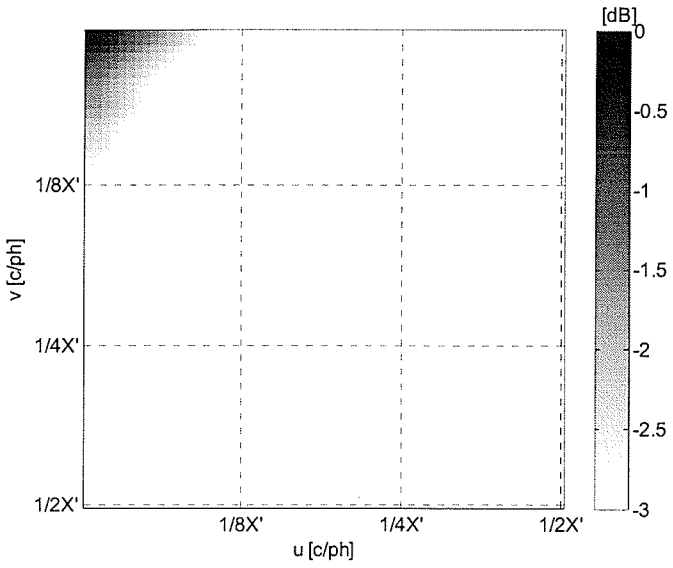

Figure 4.9. Fourier transform of the PSF at 5.10 GHz on the reciprocal lattice Γ^*.

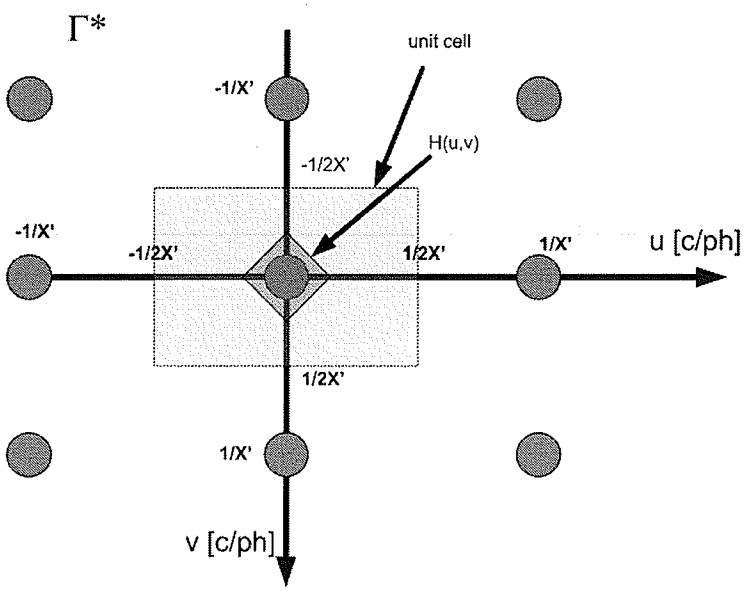

Figure 4.10. PSF frequency response.

The complex value at each nonzero sample point of the superlattices $\Gamma_{1\text{-}4}$ can be modeled as

$$g_i = \sum_{r \in \Lambda_i} f[r] \tag{4.8}$$

where f is the original image defined on Λ, r is the set of vectors (x, y) that belong to the sublattices $\Lambda_{1\text{-}4}$ that are included in the superlattices $\Gamma_{1\text{-}4}$. The signal upsampling in the superlattices is defined by the 2D discrete convolution of the scaled PSF on Γ as follows

$$s_i[r] = c\sum_k g_i[k]h[r-k] = c(g_i * h) \tag{4.9}$$

where "*" represents the 2D convolution, s_i is the upsampled image, $i = \{1, 2, 3, 4\}$ is the index that corresponds to the image defined on the sublattices $\Lambda_{1\text{-}4}$, g_i is defined in (4.8), r and k are vectors defined on the sampling structure $\Gamma_{1\text{-}4}$, h is the PSF and c is the weighting coefficient to equalize the energy after spreading. Since the intensity of each

sample is due to the coherent addition of signals according to the PSF spatial response, the upsampling has to maintain the total power in the new spread area. The PSF scaling factor c is obtained using

$$c = \frac{1}{\sum_{r \in \Gamma_i} |h(r)|^2} \tag{4.10}$$

where $|h[r]|^2$ is the antenna gain at r in Γ_i (i = 1, 2, 3, or 4). Figure 4.11 shows the results of applying the upsampling tests on the image. Note that an extra sample was included in the first and last lines of the image from the measurements in order to minimize border effects after the convolution with the PSF. These extra samples were eliminated at the end of the image reconstruction process.

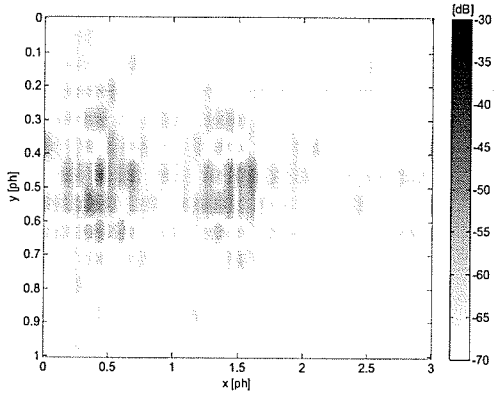

(a) Image 01 (Γ_1)

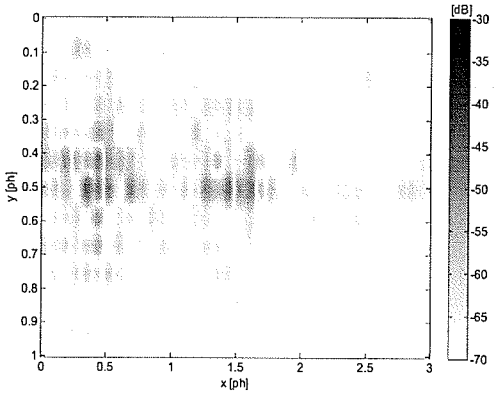

(b) Image 02 (Γ_2)

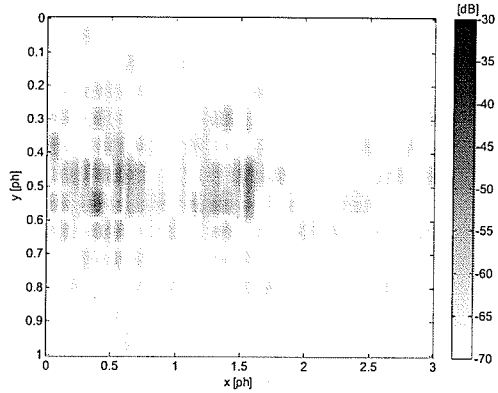

(c) Image 03 (Γ_3)

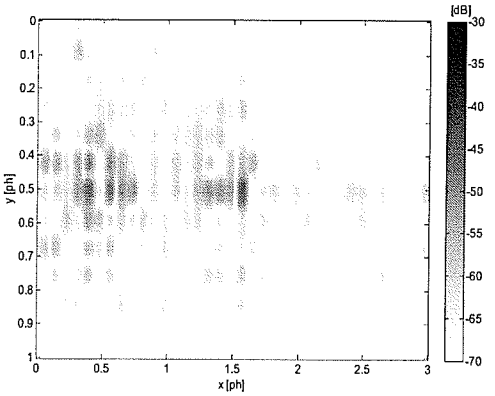

(d) Image 04 (Γ_4)

Figure 4.11. Example of upsampled images for the sampling lattices $\Gamma_{1\text{-}4}$.

4.3.2 DECONVOLUTION OF THE PSF USING THE CLEAN METHOD

Once the four correlated upsampled estimations of the CIR were obtained, the undesired effects of the PSF were minimized using the CLEAN method. Originally developed for deblurring astronomical images [29], the CLEAN algorithm has been used to reduce the effect of errors introduced by the antenna in the characterization of channels [66]-[68] and radio image processing [2].

The CLEAN deconvolution method is a recursive procedure that can be summarized as follows:

1. Calculate the noise threshold of the image. In this particular application, this can be done by establishing the multipath threshold using the CFA method [65] and estimating the remaining noise level directly from the image.

2. Define the maximum number of iterations K.

3. Find the maximum point $r_{\max} = (x_{max}, y_{max})$ in the power density image, $|s_{max}|^2$.

4. Match the maximum point with its complex value, $|s_{max}|exp(j\Phi)$, and store its magnitude, phase and location in the image, (x_o, y_o).

5. Subtract a shifted version of the PSF from the original image, weighted by the complex value in the maximum location found in step 3. Create a new image.

$$s' = \sum_{i=1}^{M}\sum_{j=1}^{N} s[i,j] - \mu(s_{\max})h[i-x_0, i-y_0] \tag{4.11}$$

where μ is a coefficient used in each iteration to control the amount of the complex signal s_{max}, weighted by the PSF, that is subtracted from each sample point (x, y) of the image, M and N are the number of samples in x and y, respectively, and h is the PSF.

6. Compute the target mass of the new image as

$$T = \sum_{i=1}^{M} \sum_{j=1}^{N} |s'[i, j]|^2 \tag{4.12}$$

7. If the target mass of the new image, which is the total signal power remaining after the noncoherent elimination of the maximum multipath, is lower than the noise threshold estimated in step 1, or the maximum number of iterations K is reached, then finalize the iteration. Otherwise, repeat the procedure starting from step 3 using the residual image, s'.

8. Store the residual image $R = s'$ after the last iteration.

9. After arriving at the stop condition, generate a new image (s_{ideal}) using the complex values stored at each recursion and padding with zeros. Replace the original antenna radiation pattern by an ideal PSF (h_{ideal}). The main beam of the original PSF is used in some cases as the ideal PSF. In other cases, a PSF with Gaussian spatial response is used due to its low-pass behaviour, avoiding the possibility of spatial aliasing by introducing high frequency components in the restored image. Convolve the clean image with the chosen ideal PSF and add the residual image:

$$s_{CLEAN} = s_{ideal} * h_{ideal} + R \tag{4.13}$$

where s_{ideal} is the reconstructed signal using the detected complex MPCs for each corresponding sample point, or equivalently, for each AoA, h_{ideal} is the ideal PSF replacing the antenna radiation pattern and R is the remaining signal after the successive iterations. Note that the signal measured is given by

$$g[x,y] = f[x,y] * h[x,y] + n \tag{4.14}$$

where g is the measured signal from the sampling structure Λ, f is the previously detected CIR, h is the PSF, which, in this case is the antenna radiation pattern, and n is the noise always present in all images. The noise level is present in the whole deconvolution process and it is reinserted after identifying each signal component at the end of the recursion in the form of the residual image.

In order to avoid the appearance of high spatial frequencies which would result from applying a rectangular window to the PSF to extract the main beam, a Gaussian response ideal PSF was used to replace the antenna response in the reconstruction. The Gaussian PSF response has the property of being simultaneously concentrated in space and frequency [15]. The 2D-Fourier transform of the ideal PSF can be expressed as follows

$$H(u,v) = \frac{c}{d(\Gamma)} 2\pi r^2 \exp(-2\pi(u^2+v^2)r^2) \tag{4.15}$$

where $d(\Gamma)$ is the sample density in the lattice Γ defined as the determinant of the lattice matrix representation, which in this case is $diag(X/5)$, c is the DC gain, and r is a constant parameter used in the design. The space-domain Gaussian PSF can be expressed as

$$h_{ideal}[z] = c\exp(-|z|^2 / 2r^2) \tag{4.16}$$

where z is a (x,y) vector in Γ, and r was defined in (4.15). The Gaussian PSF was designed for the unit cell of the reciprocal lattice Γ^* (Section 4.3.1). The limits for the unit cell in Γ^* is given by $(u,v) \leq 1/2X'$ *c/ph* and, given that the sampling rate in Γ is $X' = 1/120$ *ph*, the unit cell limits are $(u, v) \leq 60$ *c/ph*. A 3dB cut-off frequency was chosen in 30 *c/ph* to be conservative in the design. The result is shown in Figure 4.12 for frequency response and in Figure 4.13 for the spatial response.

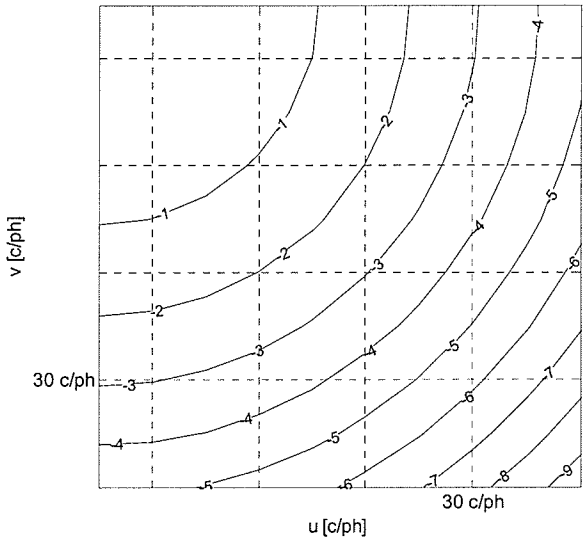

Figure 4.12. Frequency response of the Gaussian PSF.

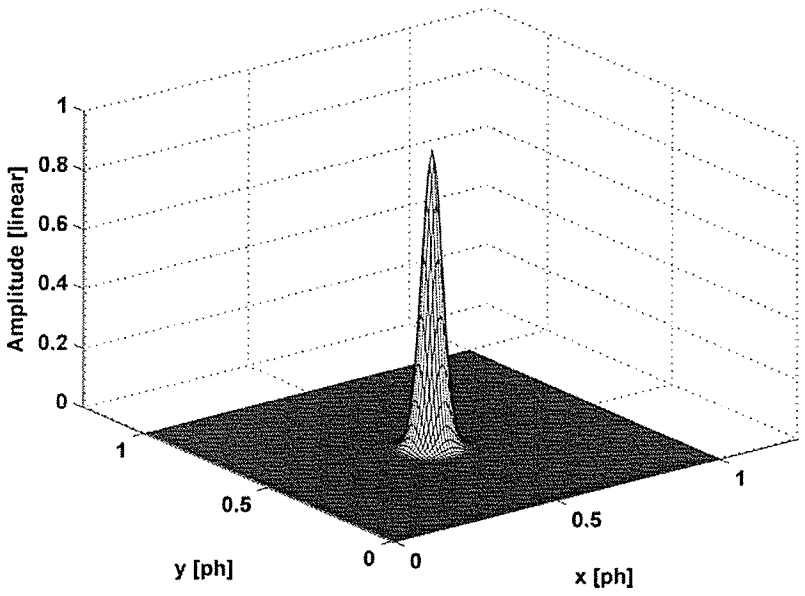

Figure 4.13. Spatial response of the Gaussian PSF.

4.3.3 THE CLEAN FEEDBACK COEFFICIENT

The feedback coefficient μ can be updated at each iteration in order to control the amount of signal subtracted from the image. By choosing a constant feedback coefficient, an excessive proportion of the signal may be subtracted, ending the iterative process too soon, or, in the other extreme, if an insufficient signal proportion is removed, more recursions will be required to finish the iterations. An early convergence of the algorithm leads to the creation of artifacts in the image as a result of the improper cancellation of the strongest multipath at each recursion. On the other hand, when the signal subtracted at each recursion step is insufficient, the poor cancellation of MPCs causes the appearance of false maxima

that are mistaken for real multipaths at the next recursion, creating artifacts in the image again.

The target mass calculated for the new image at the end of each iteration can be defined as follows

$$T(\mu) = \sum_{i=1}^{M}\sum_{j=1}^{N}\left|s[i,j] - \mu(s_{\max})h[i-x_0, j-y_0]\right|^2 \tag{4.17}$$

where s is the resultant image of the previous recursion or the original image in case of the first recursion, $s_{\max}$ is the strength of maximum norm point in the image, (x_0, y_0) are the coordinates of the maximum strength value, N and M are the maximum number of samples in x and y, respectively and μ is the feedback coefficient. Expanding expression (4.17), the target mass as a function of μ can be written as

$$\begin{aligned} T(\mu) = \sum_{i=1}^{N}\sum_{i=1}^{M}\Big(&\left|s[i,j]\right|^2 - \mu(s[i,j]s^*_{\max} + s[i,j]^* s_{\max})h[i-x_0, j-y_0] + \\ &+ \mu^2\left|s[i,j]\right|^2\left|h[i-x_0, j-y_0]\right|^2 + \mu^2\left|s[i,j]\right|^2\left|h[i-x_0, j-y_0]\right|^2\Big). \end{aligned} \tag{4.18}$$

Taking the derivative of (4.18) with respect to μ and equating to zero, the optimal feedback coefficient expression can be obtained. The updating expression for the feedback coefficient μ is given by

$$\mu_{opt} = \frac{\sum_{i=1}^{N}\sum_{j=1}^{M}(s[i,j]s^*_{\max} + s[i,j]^* s_{\max})\left|h[i-x_0, j-y_0]\right|^2}{2\sum_{i=1}^{N}\sum_{j=1}^{M}\left|s[i,j]\right|^2\left|h[i-x_0, j-y_0]\right|^2}. \tag{4.19}$$

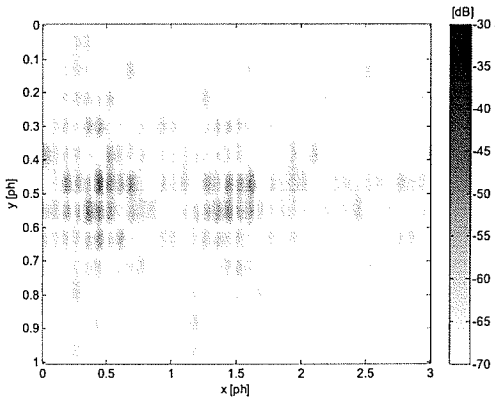

(a) Image 01 (Γ_1).

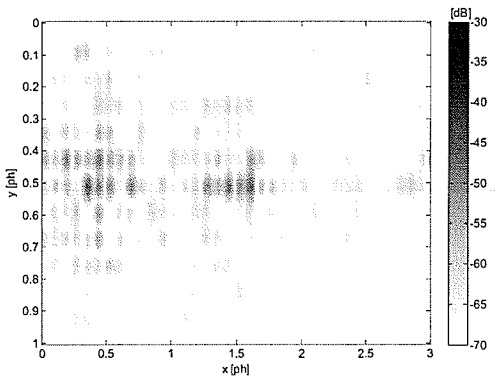

(b) Image 02 (Γ_2).

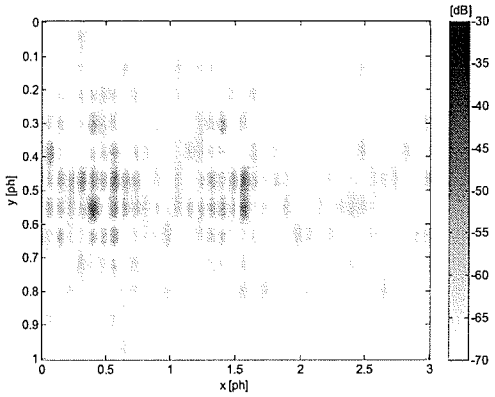

(c) Image 03 (Γ_3).

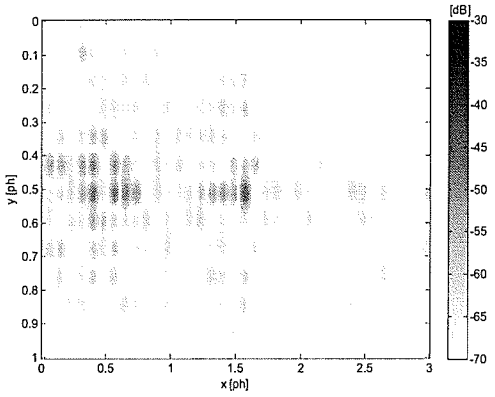

d) Image 04 (Γ_4).

Figure 4.14. Results of applying the CLEAN method to the images on $\Gamma_{1\text{-}4}$.

4.4 RECONSTRUCTION RESULTS

The CLEAN algorithm was applied to each of the four reconstructed images generated using the procedure described in Section 4.3 to extract the location and intensity of the maximum absolute points. After the image splitting and the individual upsampling (Figure 4.11), the CLEAN algorithm was applied to each image and the results are shown in Figure 4.14. The deconvolution process minimized the correlation between images caused by the PSF and consequently, they could be considered as independent realizations of the indoor channel results of four, non-overlapped lattices. Finally, the noncoherent addition of the four complex valued data sets allows the interaction between multipaths arriving with different AoAs. From the comparison between the original and the resultant images, Figures 4.15(a) and (b), respectively, it becomes evident the appearance of structural details in terms of power clusters.

The image processing described was applied to each of the 400 images corresponding to each sample frequency and the final signal was used to create the image representation of the indoor CIR as function of azimuth, elevation and delay. Some examples of the image enhancement that allowed us to improve the accuracy in the channel parameter estimation are shown in Figures 4.16 and 4.17.

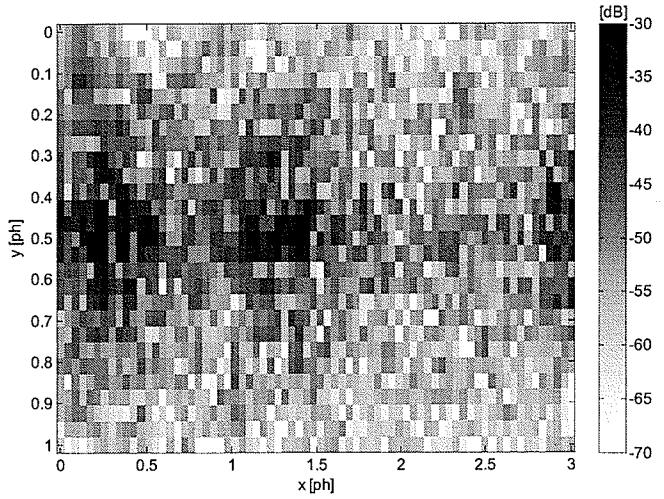

(a)

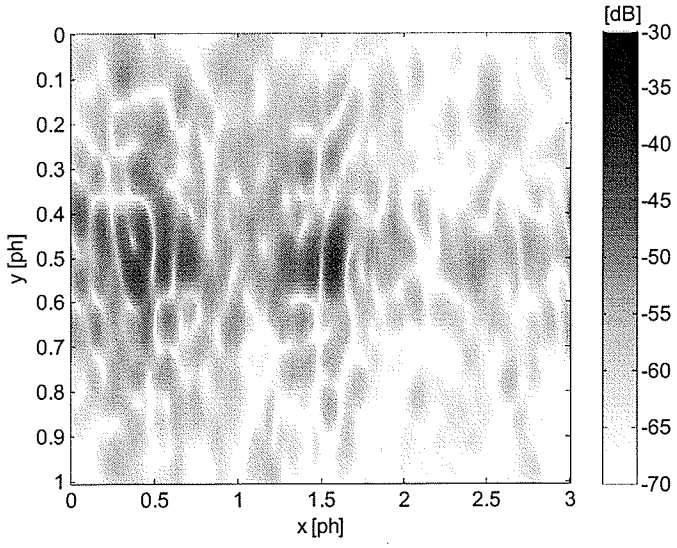

(b)

Figure 4.15. Power pattern distribution at 5.10 GHz as a function of the AoA (a) before and (b) after the channel response estimate.

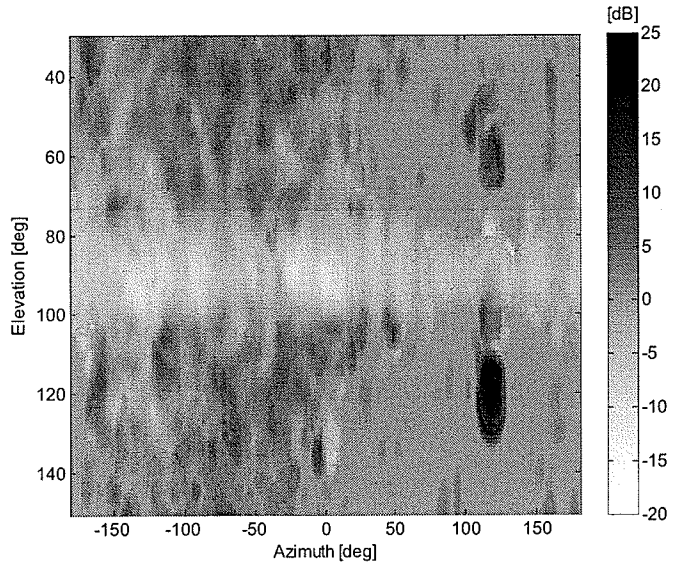

(a)

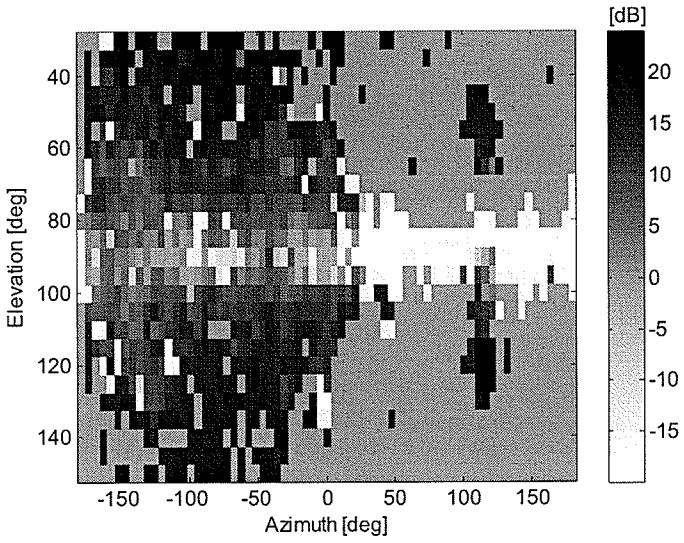

(b)

Figure 4.16. Cross-polarization distribution as a function of the AoA (a) before and (b) after the channel response estimate reconstruction.

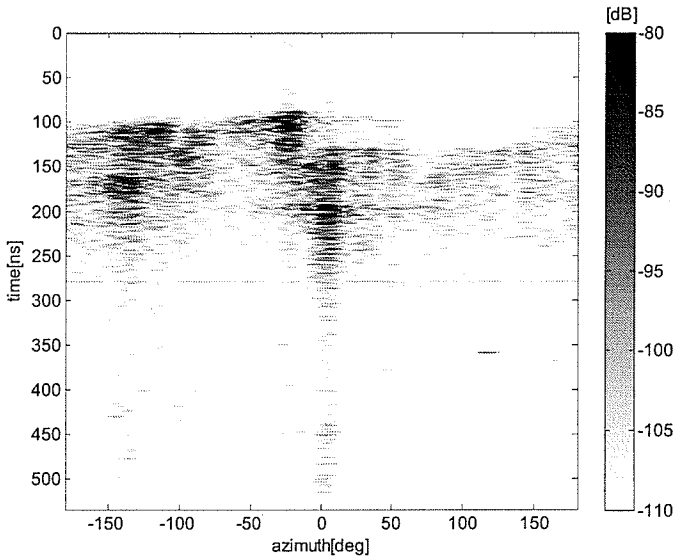

Figure 4.17. Azimuth vs. delay power pattern for 90° elevation and vertical polarization for the transmitter location A.

4.5 CONCLUSIONS AND ALTERNATIVE IMAGE PROCESSING TECHNIQUES

A variation of the CLEAN process, called sequential CLEAN, was also tested. This deconvolution technique is based on the detection of the K maximum strength points in the image at each iteration. The CLEAN method is performed in parallel on these K potential branches, finalizing the process when the first survival branch crosses the noise threshold. The idea is to overcome some limitations in the conventional CLEAN processing that could lead to errors in the identification of target points. The sequential CLEAN may lead to better performance in terms of the results but the computational complexity and, consequently, the processing time, increases exponentially with the number of branches considered. The

conventional and the sequential CLEAN algorithms were compared for this application, and it was seen that the conventional CLEAN algorithm with the feedback coefficient upgrading strategy outperforms the sequential CLEAN. Note that the PSF in this case is relatively good in terms of distortions in the image. It is left for future study to evaluate the performance of both deconvolution strategies on data sets obtained with different antenna radiation patterns.

It is also left for future studies to investigate the capabilities of these image reconstruction techniques to mitigate the effects of the antenna near-field on this type of indoor channel characterization. Furthermore, having an estimation of the PSF variation as function of the AoA may allow the application of these deconvolution techniques in situations where the shift-invariance property of the PSF does not hold.

5 JOINT TOA-AOA CHARACTERIZATION OF INDOOR CHANNELS

5.1 INTRODUCTION

The ToA characterization of a wireless channel is a fundamental part of the design and performance determination of high-speed wireless systems. For instance, the search range of rake receivers can be associated with the mean excess delay of a channel. Furthermore, the maximum transmission data rate of a channel without equalization can be estimated using the root mean squared (RMS) delay spread [57], [77]. The delay statistics are highly dependent o the indoor environment in terms of the scatterers' distribution around the receiver and their composition. The receiver antenna radiation pattern is also a factor to consider in the delay statistics [42]. In our experiment, the received signal was processed offline to remove the effects of the antenna pattern as discussed in Section 4.3.2, and then the ToA was determined for each AoA. Thus, the mean excess delay and the RMS delay spread were accurately characterized as a function of the AoA for both

polarizations and the influence of the scatterers' spatial distribution on the results could be studied.

The joint AoA-ToA characterization of the channel is studied by means of the instantaneous power distribution in Section 5.2 for different elevation angles and polarizations. As it was previously stated, location A can be characterized as a dense channel while location B is an example of sparse channel for the same sampling temporal resolution. The results show that horizontally polarized MPCs originate in reflections from the floors and ceilings surrounding the receiver area [23]. In contrast to the common assumption that co-polarized MPCs outside the horizontal plane can be neglected [62], [66]-[68], the angle-selective characterization of the channels shows clusters with significant power near the vertical elevation angles ($\theta = 40°$ and $120°$). The instantaneous results for the power distribution as a function of AoA are presented in Sections 5.2.1 and 5.2.2 while the clustering angular spread and distribution for both polarizations is left for the next chapter. The mean excess delay and RMS delay spread characterizations are presented in Section 5.3 for different AoAs and polarizations.

5.2 Power Distribution for Co- and Cross-Polarized MPCs

The joint ToA-AoA power pattern is important for studying the effects of the signal depolarization on the maximum excess delay. The results clearly show the correlation

between the elevation AoA, the creation of depolarized multipaths and the ToA statistics of the indoor channel. In this section, the propagation is studied for an omnidirectional vertically polarized transmitter antenna located in the auditorium (location A) and in an office (location B), whose locations are indicated in Figure 3.11. The received signal in the main lobby, whose relative location with respect to the transmitter is indicated in Figure 3.12, is measured for different AoAs and for both E-field polarizations: vertical (co-polarized) and horizontal (cross-polarized). The delay resolution used in this experiment allows the identification of MPCs with relative excess delays as small as 2 ns.

5.2.1 LOCATION A

The auditorium is a location prone to the creation of scattered multipath signals in different directions (Figure 3.13(1)) around the transmitter area. This signal scattering near the transmitter creates multipath signals coming from diverse elevation angles, some of them close to the vertical ($\theta \sim 30°$ and $\sim 150°$). These multipath signals originate the cross-polarized signals in the receiver area by reflections from the floors and ceilings of the lobby area (Figure 3.12). However, the multipath signals that arrive at the receiver from elevation angles outside the horizontal plane ($\theta = 90°$) were already subject to one or more reflections from walls and floors and, at least, one transmission through the wall that separates the auditorium and the lobby (Figure 3.13(5)). Hence, these signals arrive with much more attenuation than those echoes coming after a smaller number of interactions with the surrounding environment. The relative importance and AoA of multipath signals can be illustrated by comparing the received power distribution for

$\theta = 30°$ as a function of the azimuth AoA and the delay for cross-polarized signals shown in Figure 5.1(a) against the co-polarized power distribution shown in Figure 5.1(b). In these figures $\varphi = 0°$ is the azimuth angle normalized with respect to the virtual LOS between receiver and transmitter. In the first case, shown in Figure 5.1(a), a large number of power clusters is received coming from $-100° \leq \varphi \leq 150°$ around the receiver, however their relative power is about 20 dB less than the maximum received power of co-polarized signals shown in Figure 5.3(b).

The MPC clustering phenomenon in delay vs. azimuth AoA is shown in Figures 5.1-5.4 for 30°, 60°, 90°, and 120° elevation AoAs, respectively, for both polarizations of MPCs: horizontal (cross-polarized) and vertical (co-polarized). The location and relative strength of cross-polarized clusters of MPCs was pointed out in Figure 5.1(a) but it is important to mention the relative absence of co-polarized power clusters for the same elevation angle ($\theta = 30°$) as shown in Figure 5.1(b). This absence of co-polarized clusters for the same azimuth AoA indicates that the cross-polarized signals are horizontally polarized echoes which vertical counterpart was attenuated below the detection threshold. The co-polarized power clusters become more significant for elevation AoAs closer to the horizon ($\theta = 90°$). Finally, for elevation AoAs below the horizontal plane, the cross-polarized power clusters are important in comparison with the co-polarized clusters as shown in Figure 5.4 for $\theta = 120°$. For $\theta > 125°$, no power clusters were measured for either polarization states. It is worth mentioning that cross-polarized signals are present at all four elevation angles presented here (Figure 5.1(a)-5.4(a)) while the co-polarized signals arrive only with elevation AoAs around the horizontal plane (Figure 5.2(b) and Figure 5.3(b)).

The maximum excess delay (MED) is an indication of the total temporal spread of the signal or, in other words, the ToA of the last valid MPC normalized with respect to the first MPC arrival. The maximum duration signals were measured for both polarizations for azimuth AoAs around the direction of the receiver-transmitter ($-50° \leq \varphi \leq 50°$). The results for the MED for location A are shown in Table 5.1. Even though the co-polarized signals have the maximum duration in the horizontal plane, the cross-polarized signals present less variation in the MED.

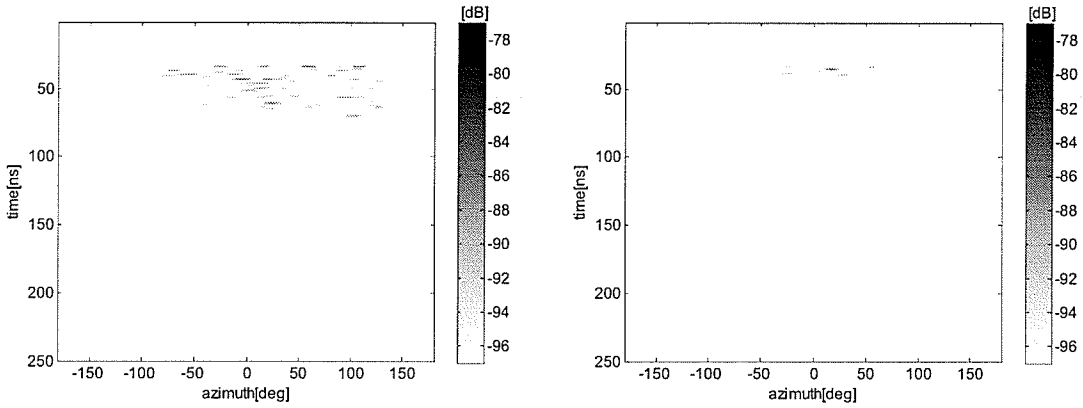

(a) Horizontal (cross-polarized). **(b) Vertical (co-polarized).**

Figure 5.1. Channel gain as functions of the azimuth AoA and the ToA (location A): 30° elevation.

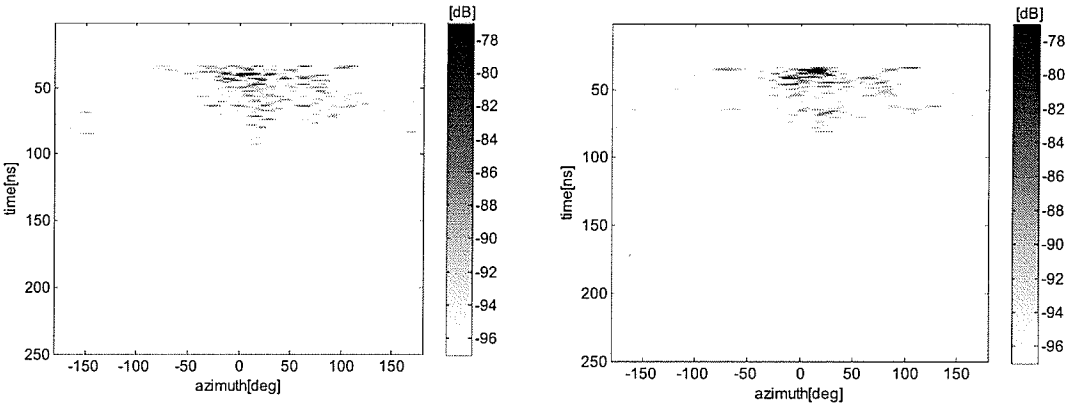

(a) Horizontal (cross-polarized). **(b) Vertical (co-polarized).**

Figure 5.2. Channel gain as functions of the azimuth AoA and the ToA (location A): 60° elevation.

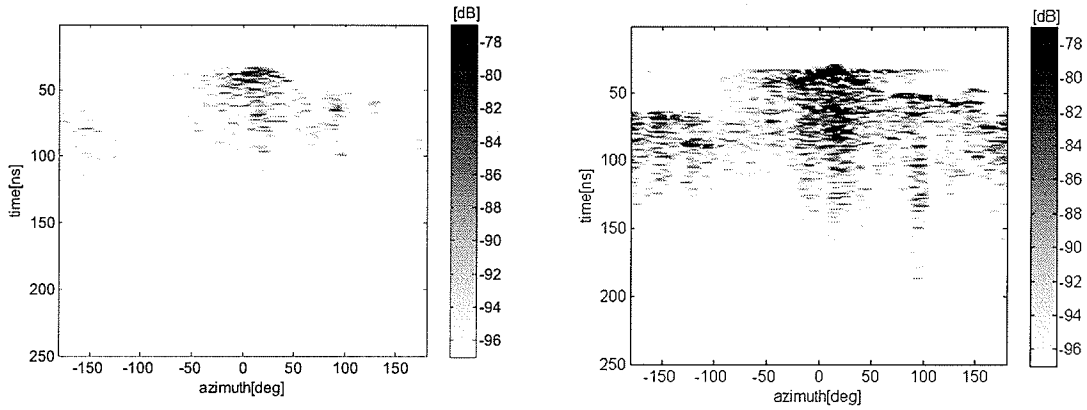

(a) Horizontal (cross-polarized). **(b) Vertical (co-polarized).**

Figure 5.3. Channel gain as functions of the azimuth AoA and the ToA (location A): 90° elevation

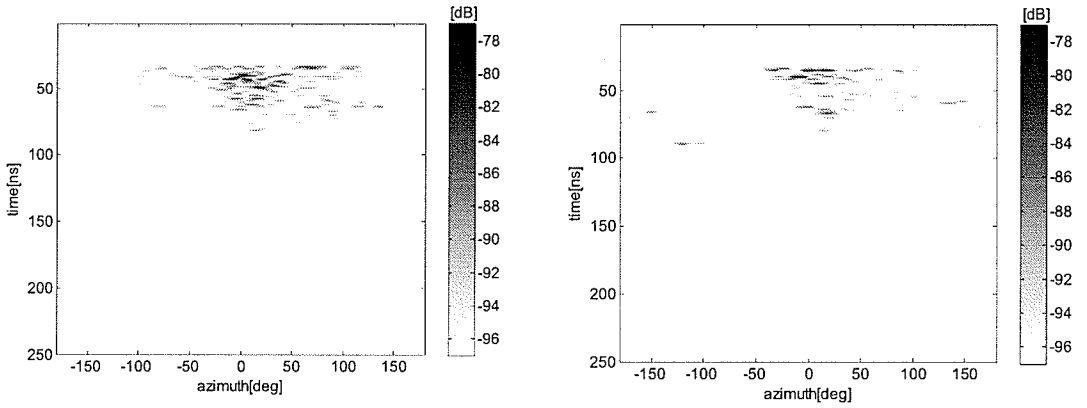

(a) Horizontal (cross-polarized). **(b) Vertical (co-polarized).**

Figure 5.4. Channel gain as functions of the azimuth AoA and the ToA (location A): 120° elevation.

Table 5.1. Maximum excess delay (location A).

Elevation AoA	Maximum Excess Delay	
	Cross-polarized	Co-polarized
30°	49 ns	7 ns
60°	75 ns	50 ns
90°	87 ns	175 ns
120°	60 ns	50 ns

The polarization dependence of the AoA is shown by the azimuth-elevation AoA power distributions in Figure 5.5-5.7 for 30, 50, and 75 ns delays. One observation is that MPCs appear in clusters, not only in the azimuth and delay as was reported in earlier measurements [42], [62], [66], but also in elevation for both polarizations. It is interesting to note that initially the power distribution for both polarizations presents a large spread in the elevation AoA. The MPCs that arrive at the receiver site with smaller delays, such as those represented in Figure 5.5, are the scattered signals that travel the shortest distance and therefore have the smallest number of interactions with the surrounding obstacles. For instance, both polarization components are located around $\varphi = 0°$, which represents the direction of the transmitter. Thus, the elevation angle spread in the wavefronts can be explained by first and second order interactions with the environment, which leads to significantly more power than the later arrivals, i.e., transmission through walls and transmission plus reflections coming from the floors and ceilings. The more delayed the multipaths, the more localized are the co-polarized MPCs in the horizontal

plane (Figure 5.6(b) and 5.7(b)) while the cross-polarized components retain the elevation angle spread for all the excess delay (Figure 5.6(a) and 5.7(a)).

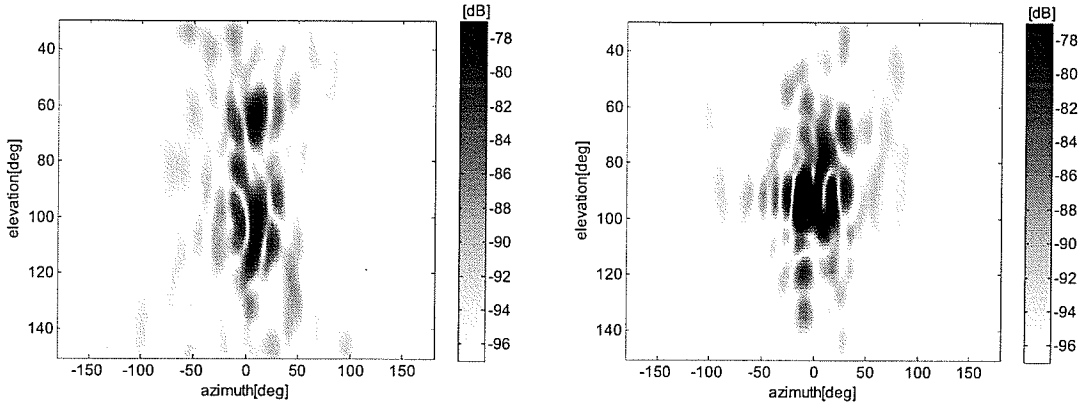

(a) Horizontal (cross-polarized). **(b) Vertical (co-polarized).**

Figure 5.5. Channel gain as a function of the AoA (location A): 30 ns delay.

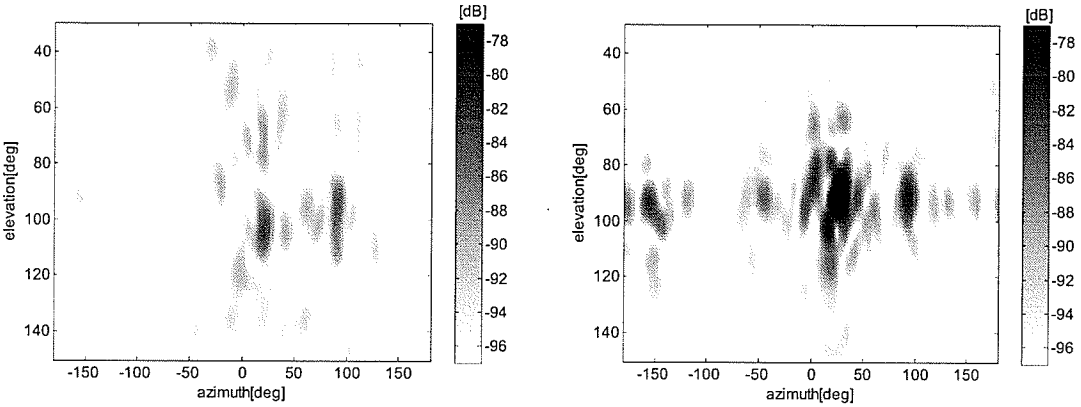

(a) Horizontal (cross-polarized). **(b) Vertical (co-polarized).**

Figure 5.6. Channel gain as a function of the AoA (location A): 50 ns delay.

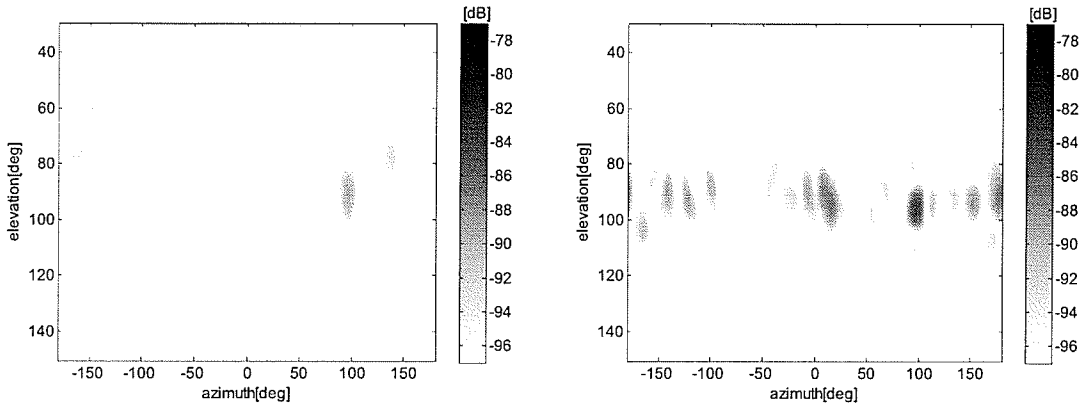

(a) Horizontal (cross-polarized). **(b) Vertical (co-polarized).**

Figure 5.7. Channel gain as a function of the AoA (location A): 90 ns delay.

5.2.2 LOCATION B

The signal propagation when the transmitter is located in the office and the receiver is in the main lobby (Figure 3.11) differs from that when the transmitter was in the auditorium (location A) for both polarizations. Figures 5.8-5.11 compare the MPC clusters as a function of the azimuth AoAs and MPCs' delay for 30°, 60°, 90°, and 120° elevation angles. The co- and cross-polarized MPCs detected in location B are mostly the depolarized components of the same multipath signals. The same location for cross- and co-polarized power clusters in azimuth and delay for different elevations shows that both polarized signals are part of the same depolarized multipath signal. In contrast to what is observed for location A (Figures 5.5(a)-5.7(a)), the cross-polarized signals appear mainly for $60° \leq \theta \leq 120°$ as shown in Figures 5.8(a)-5.11(a). The observed depolarization phenomenon can be explained by the different propagation processes that dominate for each transmitter location. Since the different delayed echoes of the transmitted signal

have to travel along the hallway that connects the transmitter to the receiver location, the received MPCs are the result of interactions with a different environment. The hallway walls act loosely as a waveguide that favours the co-polarized components. Hence, the resultant MPCs that arrive at the receiver area are co-polarized and mostly concentrated on the horizontal plane since de-polarized multipaths are attenuated long before arriving. The remaining horizontally polarized components are the result of interactions with floors, ceilings and other scatterers in the surroundings of the receiver [23].

The MED observed in location B for both polarizations are shown in Table 5.2. The larger MED observed for co-polarized components in comparison with those observed for location A can be explained by the indoor topology that favours the propagation of vertically polarized signals enabling late echoes to be received as valid MPCs.

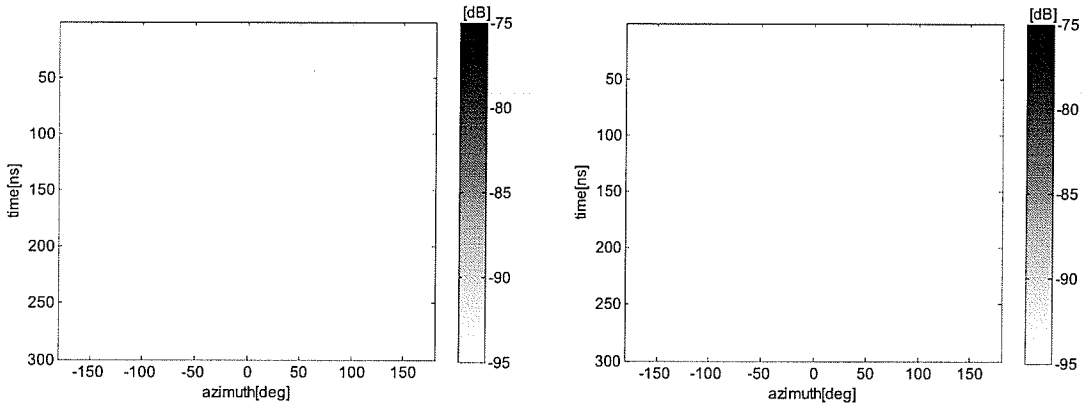

(a) Horizontal (cross-polarized). (b) Vertical (co-polarized).

Figure 5.8. Channel gain as a function of the azimuth AoA and the ToA (location B): 30° elevation.

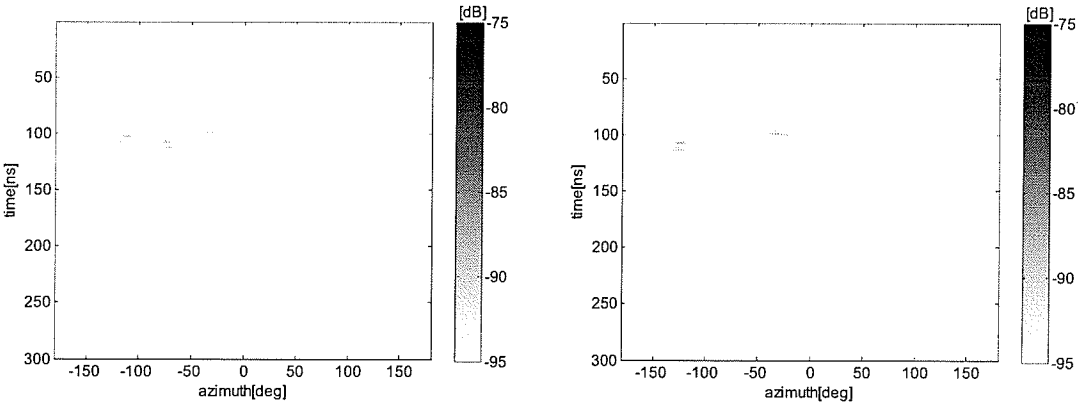

(a) Horizontal (cross-polarized). (b) Vertical (co-polarized).

Figure 5.9. Channel gain as a function of the azimuth AoA and the ToA (location B): 60° elevation.

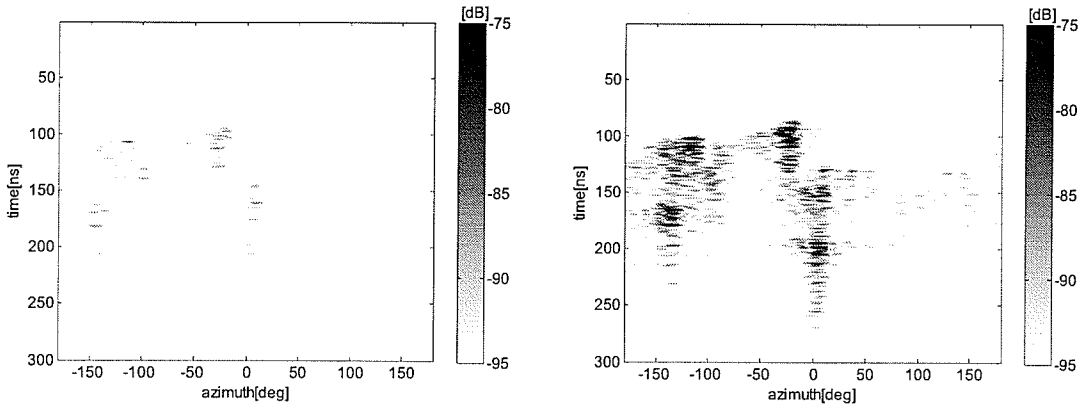

(a) Horizontal (cross-polarized). (b) Vertical (co-polarized).

Figure 5.10. Channel gain as a function of the azimuth AoA and the ToA (location B): 90° elevation.

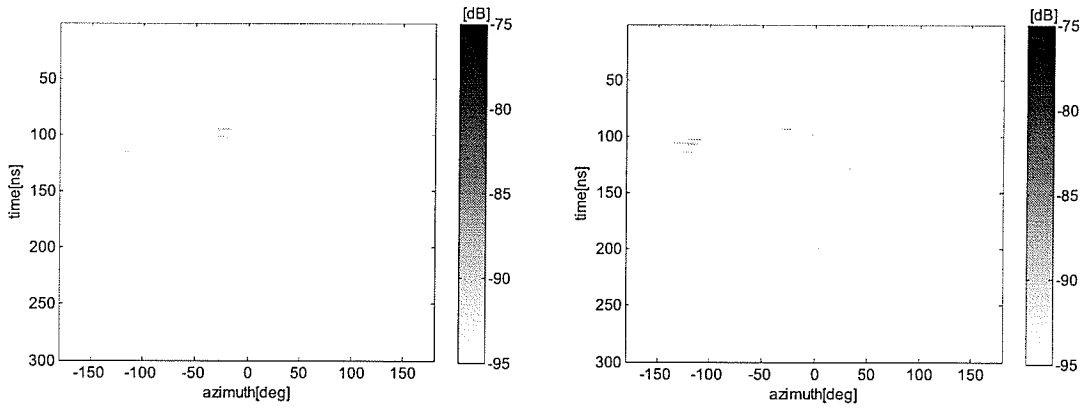

(a) Horizontal (cross-polarized). (b) Vertical (co-polarized).

Figure 5.11. Channel gain as a function of the azimuth AoA and the ToA (location B): 120° elevation.

Table 5.2. Maximum excess delay (location B).

Elevation AoA	Maximum Excess Delay	
	Cross-polarized	Co-polarized
30°	10 ns	NA
60°	18 ns	62 ns
90°	110 ns	225 ns
120°	25 ns	125 ns

The azimuth vs. elevation AoA power distributions, shown in Figures 5.12-5.14, exhibit similar propagation mechanisms to those observed for location A (Figures 5.5-5.7). The first MPC to arrive shows a larger spread in elevation AoA than the other multipaths. The cross-polarized MPCs are grouped in clusters with elevation AoAs above and below the horizontal plane while co-polarized MPCs tend to concentrate in clusters centered in the horizontal plane for larger excess delays.

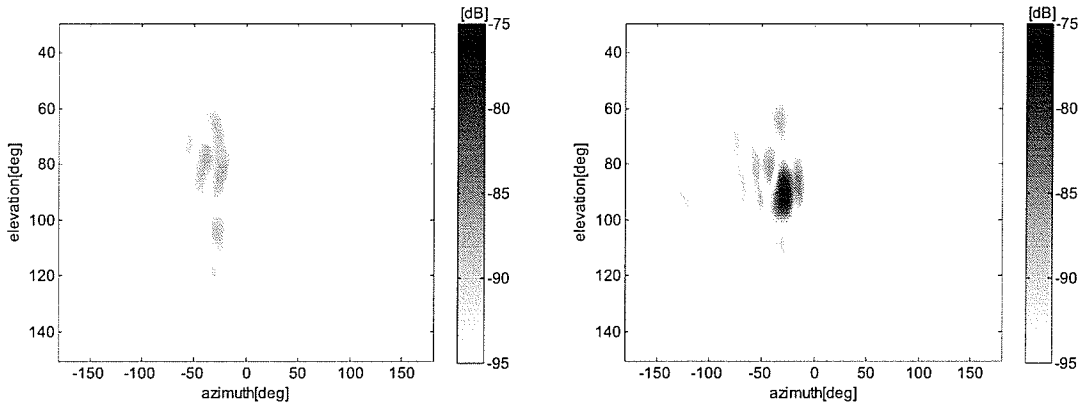

(a) Horizontal (cross-polarized). **(b) Vertical (co-polarized).**

Figure 5.12. Channel gain as a function of the AoA (location B): 95 ns delay.

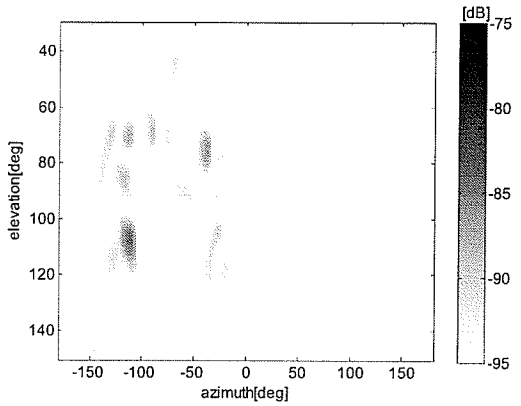

(a) Horizontal (cross-polarized).

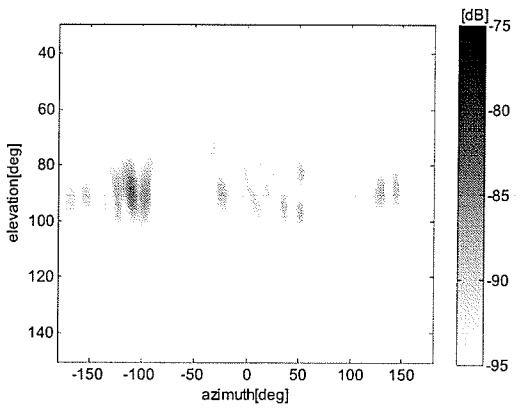

(b) Vertical (co-polarized).

Figure 5.13. Channel gain as functions of the AoA (location B): 120 ns delay.

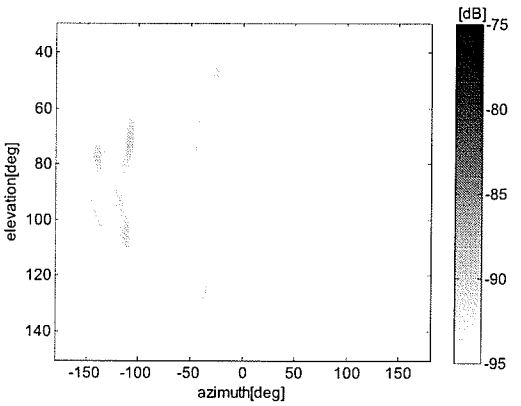

(a) Horizontal (cross-polarized).

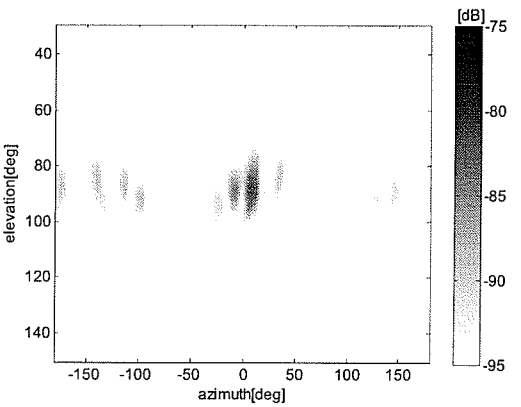

(b) Vertical (co-polarized).

Figure 5.14. Channel gain as a function of the AoA (location B): 150 ns delay.

5.3 TOA CHARACTERIZATION

The performance degradation in a digital communication system can be estimated by characterizing certain measures of the severity of the multipath propagation. The

PWMED defined in (2.27) can be used to characterize the temporal dispersion of MPCs. Wideband systems performance can be compromised by intersymbol interference (ISI). The RMS delay spread, sometimes referred to as the *power weighted* delay spread, defined in (2.28) can be used as a quality factor to determine the maximum transmission data rate in a channel without equalization [77]. In the previous section, the joint AoA-ToA channel gain results for both polarizations were explained in terms of the distinct propagation characteristics of each transmitter-receiver indoor location. In this section, the results for the MPCs' ToA statistics for both transmitter locations and polarizations are characterized by means of the PWMED and the RMS delay spread. The analysis was performed for $\theta = 30°, 60°, 90°, 120°$, and $150°$ and $-180° \leq \varphi \leq 180°$.

5.3.1 LOCATION A

The mean excess delay is shown in Figure 5.15 for both polarized signals. It was observed that the PWMED for cross-polarized signals is more uniformly distributed as a function of the azimuth AoA than that for co-polarized signals which shows a minimum around $\varphi = 0°$. The same observation can be made for the RMS delay spread estimation shown in Figure 5.16. A high PWMED indicates that the MPCs arrive with relatively similar power along the total signal excess delay as is shown in Figure 5.17(a) and (b) for $\theta = 90°$ and $\varphi = 0°$, labeled H1 (cross-polarized) and V1 (co-polarized), respectively. The channel gain normalized with respect to the maximum signal level for both polarizations in location A is indicated in Figure 5.19 as a function of ToA for cases H1 and V1, respectively. In both examples, the MPCs' levels do not demonstrate the exponential

decreasing envelope observed for $\varphi = 100°$ as shown in Figure 5.18(a)-(b) for H2 and V2, respectively. For the considered elevation angles, the co-polarized signals are constrained in clusters with different delays around $-50° < \varphi < 50°$ (Figure 5.1(a)-5.4(a)), which implies that the values of the PWMED and the RMS delay spread should be restricted to those azimuth angles. The appearance of isolated clusters for elevation angles outside the horizontal plane in the case of co-polarized signals could lead to anomalous estimations of the ToA statistics. This is the case for the PWMED and RMS delay spread for $-150° < \varphi < -100°$ and $\theta = 60°$ in Figure 5.15 and Figure 5.16 that can be tracked to the low power co-polarized clusters for those AoAs from Figure 5.11.

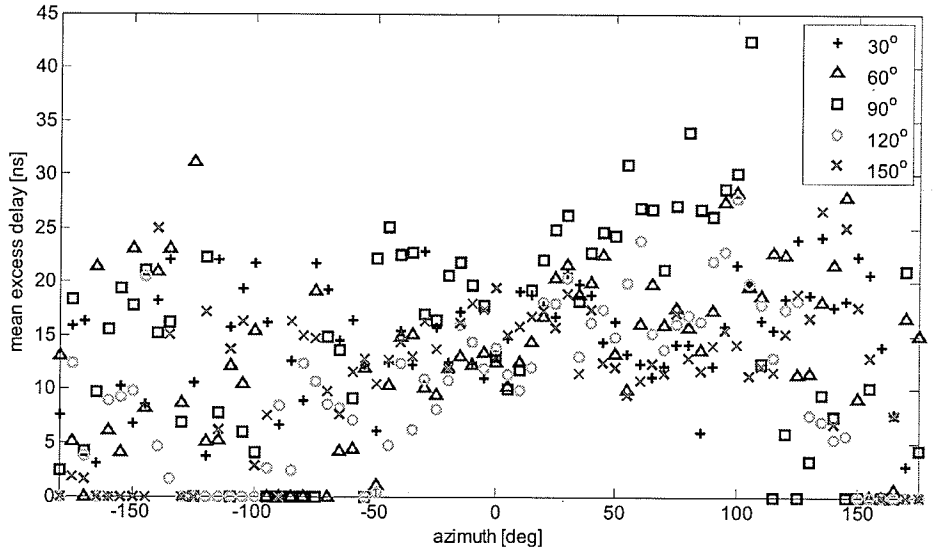

(a) Horizontal (cross-polarized).

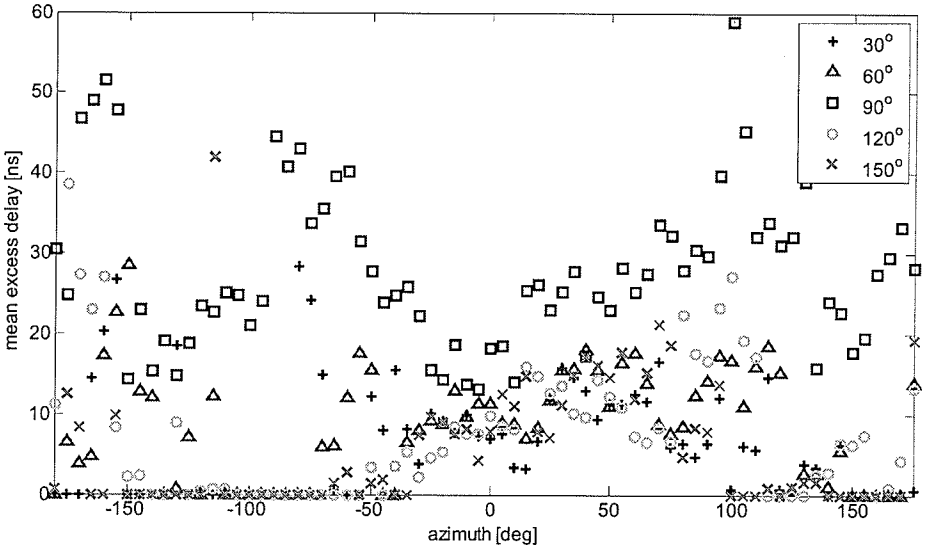

(b) Vertical (co-polarized).

Figure 5.15. Mean excess delay for different elevation angles (location A).

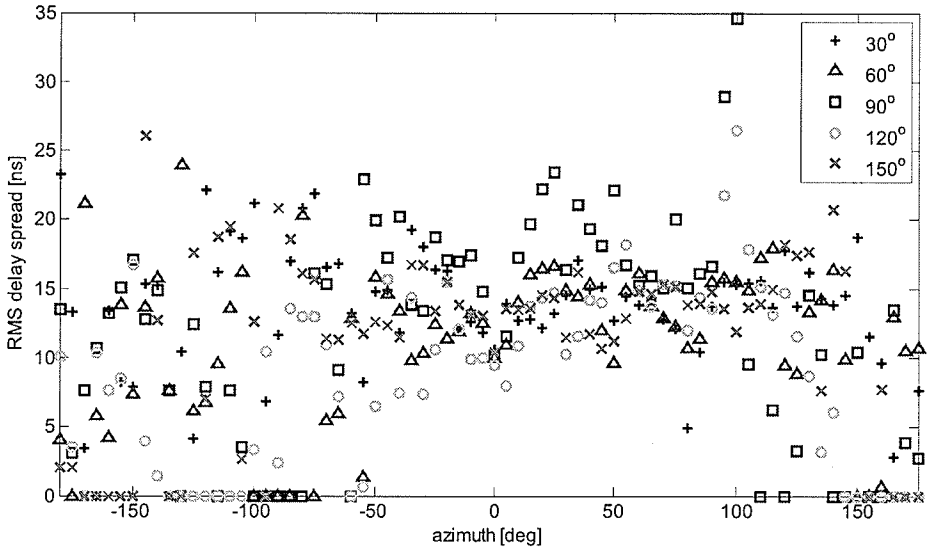

(a) Horizontal (cross-polarized).

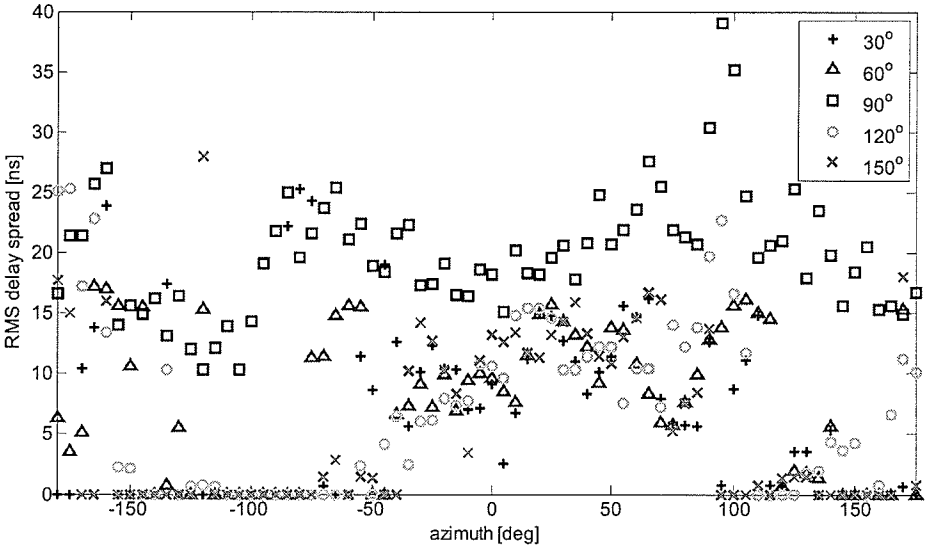

(b) Vertical (co-polarized).

Figure 5.16. RMS delay spread for different elevation angles (location A).

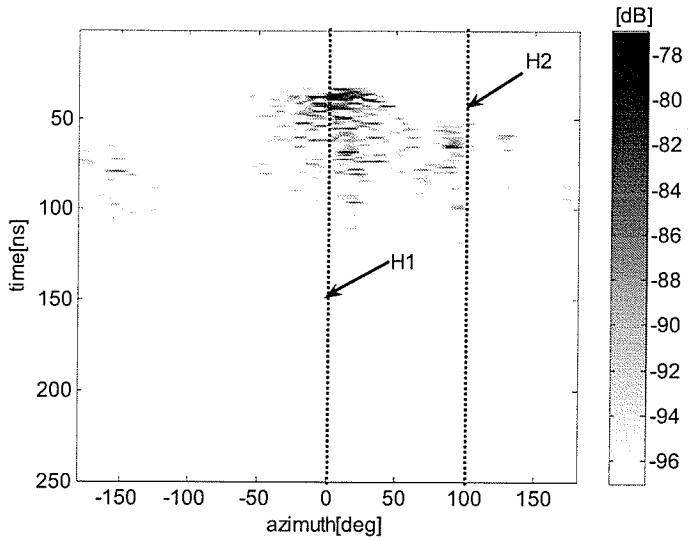

(a) Horizontal (cross-polarized).

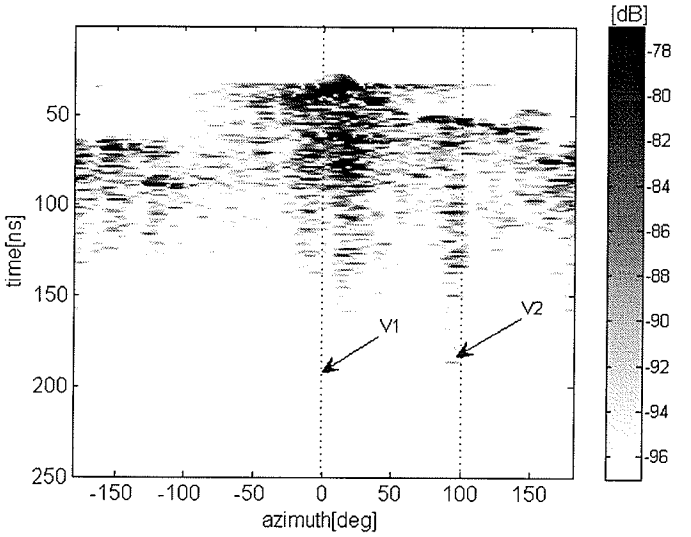

(b) Vertical (co-polarized).

Figure 5.17. Channel gain as a function of the azimuth AoA and the ToA for location A.

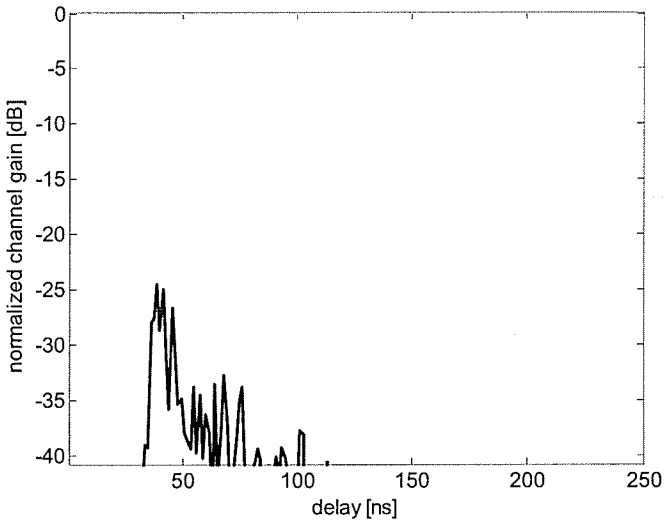

(a) H1: horizontal (cross-polarized).

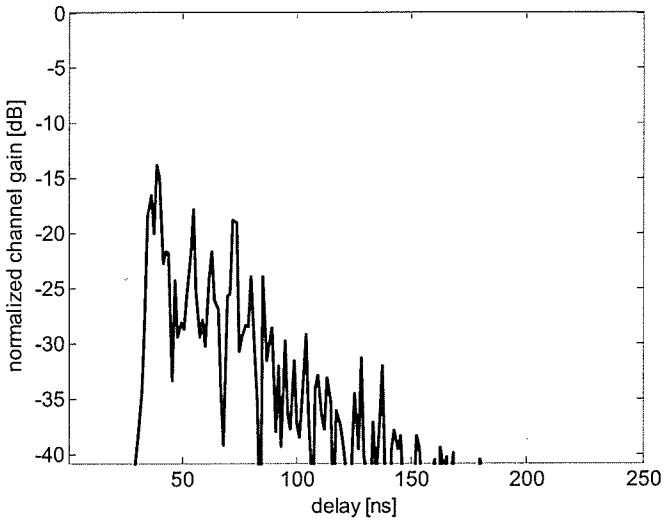

(b) V1: vertical (co-polarized).

Figure 5.18. Normalized channel gain for location A at $\varphi = 0°$ and $\theta = 90°$ showing the exponentially decaying envelope.

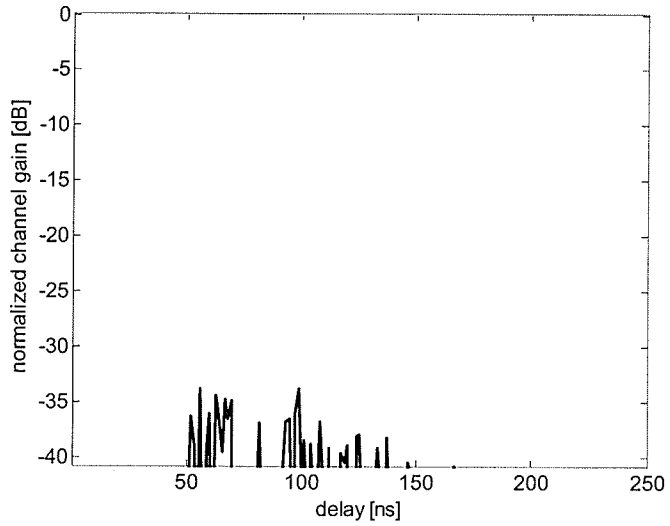

H2: horizontal (cross-polarized).

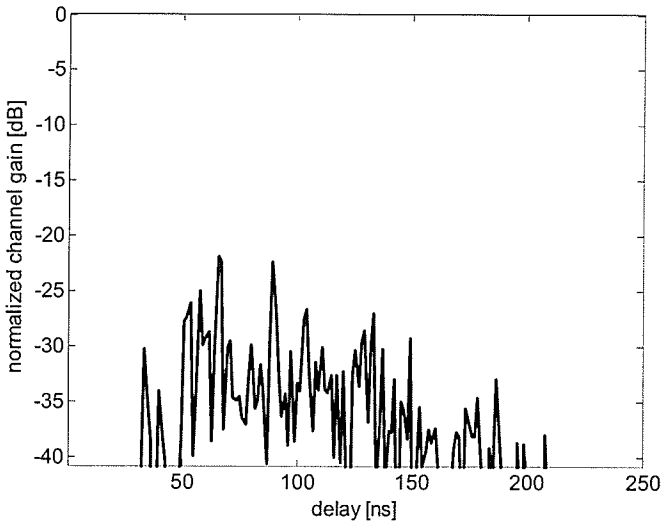

(b) V2: vertical (co-polarized).

Figure 5.19. Normalized channel gain for location A for the maximum PWMED and RMS delay spread located at $\varphi = 100°$ and $\theta = 90°$.

5.3.2 LOCATION B

In the analysis of the observations in Section 5.2.2, it was shown that the co-polarized signals are limited fundamentally to the clusters around the horizontal plane for this propagation scenario. Furthermore, it is seen in Figures 5.12(b)-5.14(b) that the co-polarized MPCs in this location arrive in clusters limited to $60° < \theta < 120°$, and from Figures 5.9(b)-5.11(b), that the main co-polarized clusters are located in $-150° < \varphi < 50°$. The first difference with location A (Section 5.3.1) is that the PWMED for cross-polarized MPCs, as shown in Figure 5.20, is not uniformly distributed in azimuth for different elevation angles but instead follows the same pattern as the co-polarized MPCs. This can be explained by the high correlation between co- and cross-polarized MPCs in this scenario. As it was shown in Section 5.2.2, in this case cross-polarized multipaths are mostly the horizontally polarized components of the same depolarized signal. The maximum PWMED shown in Figure 5.20(a)-(b) for cross- and co-polarized signals, respectively, are located approximately at $\varphi = 5°$ and $\varphi = -140°$ and around $\theta = 90°$. The same AoAs can be verified for the maximum RMS delay spread as shown in Figure 5.21. In order to study these peaks in PWMED and RMS delay spread, the time-domain channel gain for $\theta = 90°$ and $\varphi = 5°/-140°$ are indicated in Figure 5.22 with H1-H2 and V1-V2 for horizontal and vertical polarizations, respectively. As in the previous section, the channel gain was normalized with respect to the maximum MPCs power for location B. It can be seen from Figure 5.23 that more than one cluster with similar power appear consecutively in both polarized signals for $\varphi = -140°$ explaining the high PWMED and

the RMS delay spread. The same analysis can be made for $\varphi = 5°$ as seen in Figure 5.24, where the largest MPCs arrive in clusters separated by tens of ns. Note that in the case of co-polarized MPCs at $\varphi = 5°$ and $\theta = 90°$ (Figure 5.24(b)), the MPC clusters are separated about 100 ns, which coincide with the estimated PWMED.

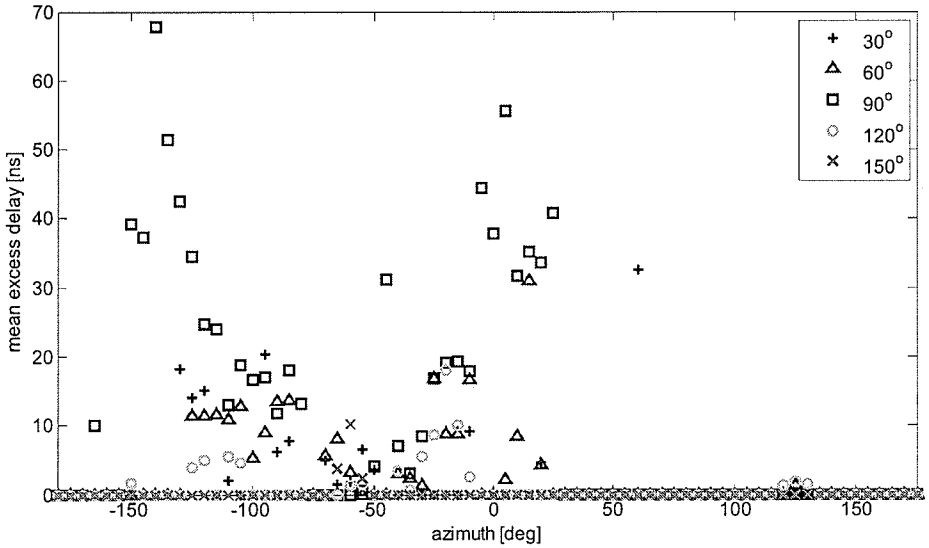

(a) Horizontal (cross-polarized).

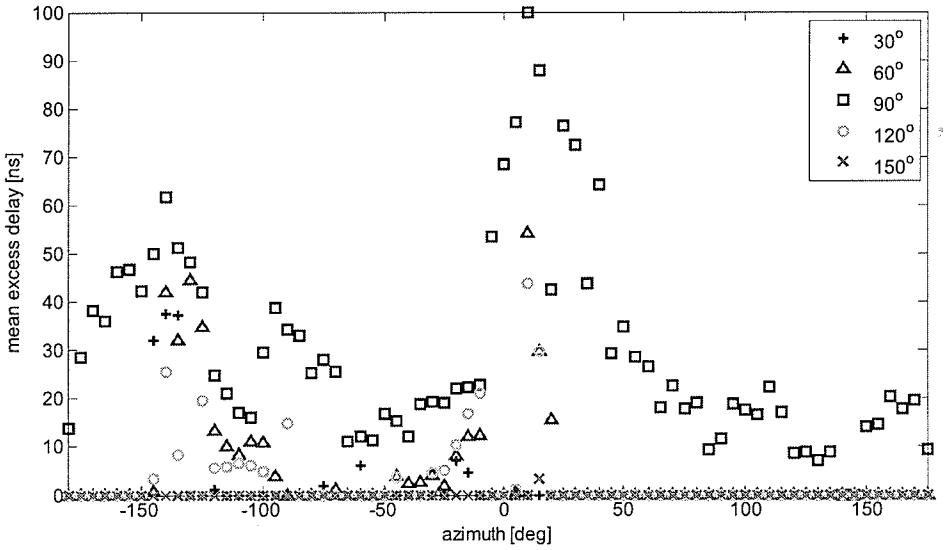

(b) Vertical (co-polarized).

Figure 5.20. Mean excess delay for different elevation angles (location B).

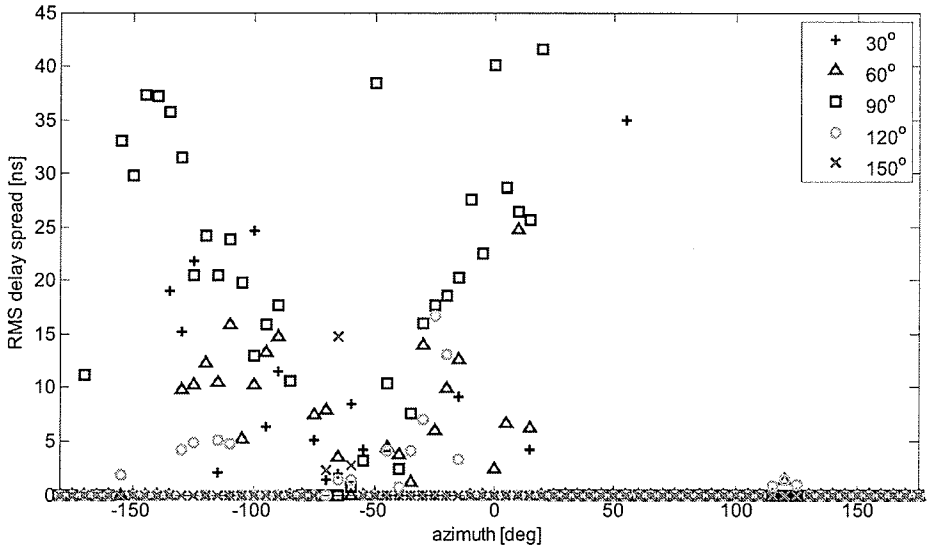

(a) Horizontal (cross-polarized).

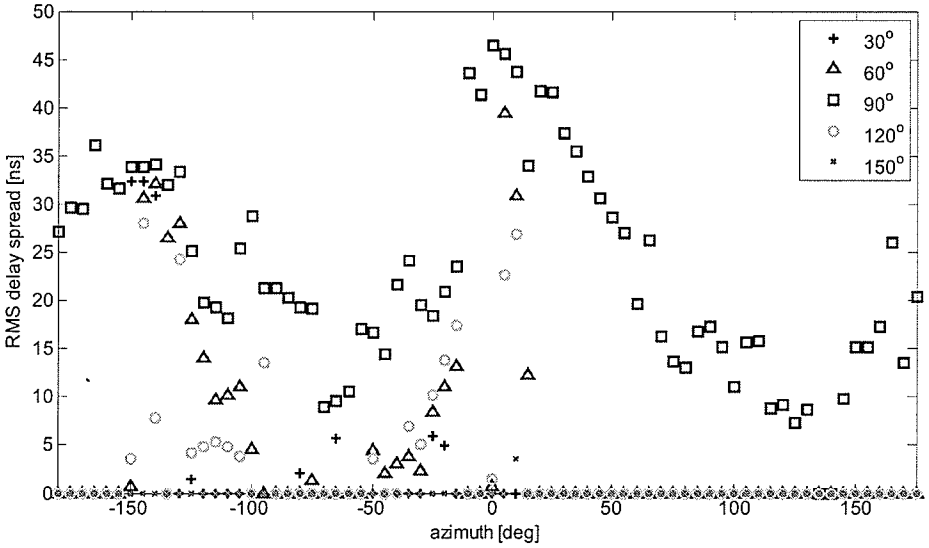

(b) Vertical (co-polarized).

Figure 5.21. RMS delay excess (location B).

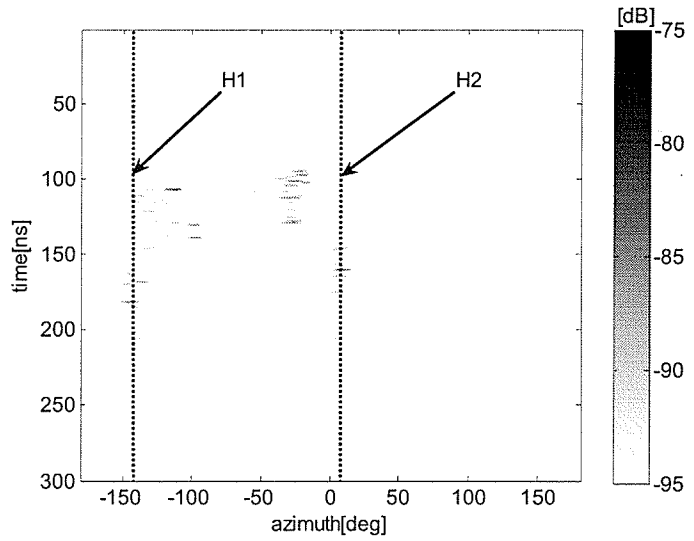

(a) Horizontal (cross-polarized).

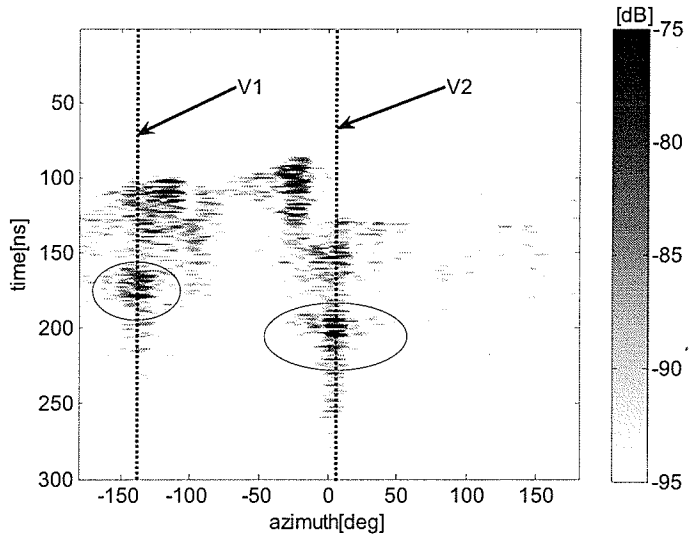

(b) Vertical (co-polarized).

Figure 5.22. Channel gain as a function of the azimuth AoA and the ToA for location B.

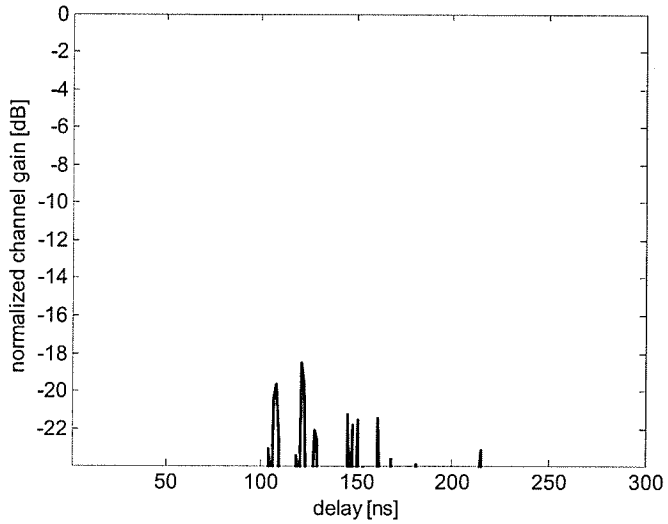

(a) H1: horizontal (cross-polarized).

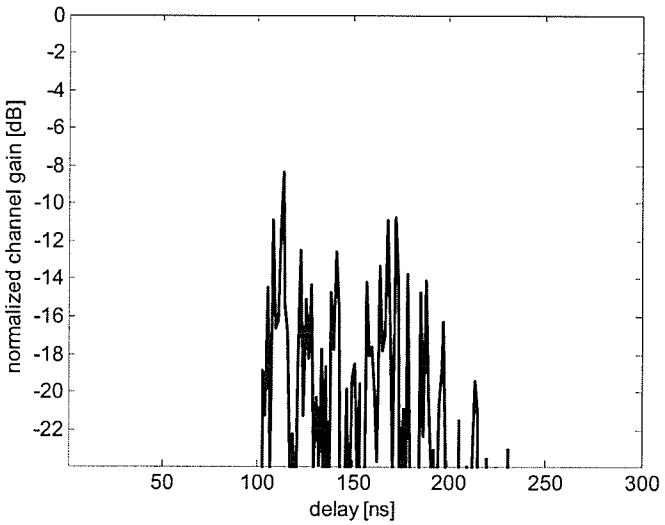

(a) V1: vertical (co-polarized).

Figure 5.23. Normalized channel gain for location B for the maximum PWMED and RMS delay spread located at $\varphi = -140°$ and $\theta = 90°$.

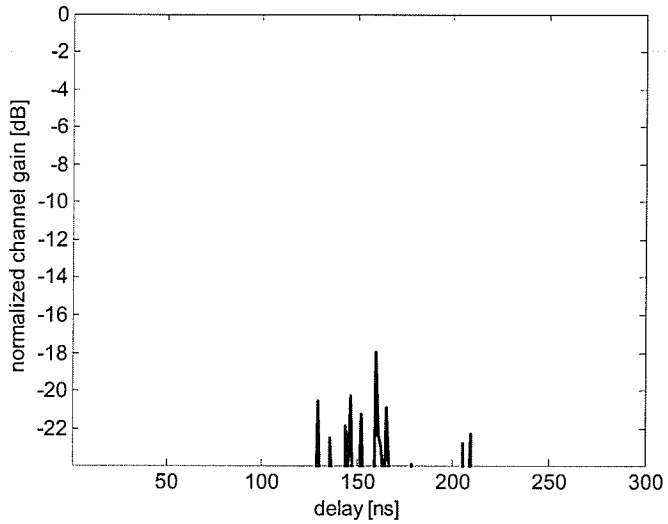

(a) H2: horizontal (cross-polarized).

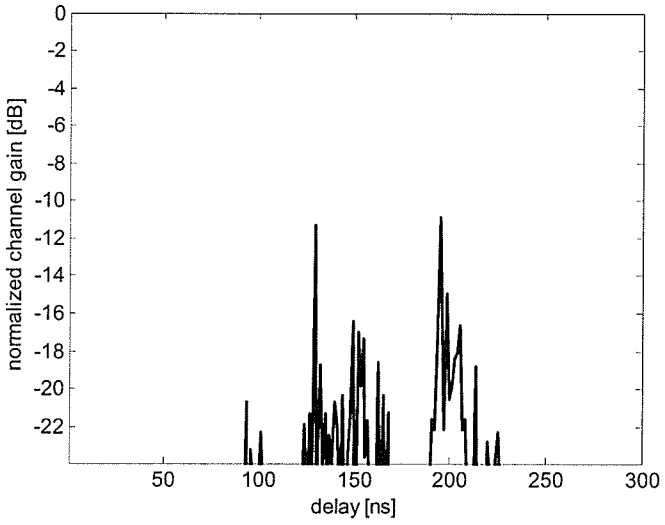

(b) V2: vertical (co-polarized).

Figure 5.24. Normalized channel gain for location B at $\varphi = 5°$ and $\theta = 90°$ showing the exponentially decaying envelope.

5.4 SUMMARY OF RESULTS

In this chapter, the joint AoA-ToA power distribution analysis of results was presented for the both indoor scenarios selected for the study. It was seen that, when the scattered signals came from angles close to the vertical, the cross-polarized MPCs appear in clusters distributed homogeneously in elevation for different delays (location A). For extreme elevation angles (θ close to 30° and 150°), clusters of only cross-polarized MPCs were observed. In contrast, when the indoor scenario favours the propagation of co-polarized signals (location B), the scattering in the surroundings of the receiver area creates cross-polarized signals at similar AoAs to the co-polarized signals. In both locations, the maximum excess delay occurs at $\theta = 90°$ for both polarizations. The ToA statistics show that, for location A, the PWMED and RMS delay spread for cross-polarized signals are uniformly distributed as a function of the azimuth AoA for a given elevation angle. In contrast, the co-polarized MPCs are more densely spaced near the horizontal plane ($60° < \theta < 120°$) and over restricted azimuth angles ($-50° < \varphi < 50°$). For other AoAs, the ToA statistics account for anomalous effects such as isolated co-polarized clusters that create peaks in the estimated values. The ToA statistics in location B exhibit a larger correlation in terms of cross- and co-polarized MPCs. The maximums of the PWMED and RMS delay spread can be explained by the concentrations of MPCs in clusters with similar maximum power.

6 CROSS-POLARIZATION CHARACTERIZATION FOR INDOOR ENVIRONMENTS

6.1 INTRODUCTION

The polarization characterization of indoor channels is important not only in the design of polarization diversity systems but also as a means to quantify the losses incurred by considering only the co-polarized signals in the existing links. The cross-polarization of an electromagnetic wave is the amount of power that is received orthogonally polarized with respect to its transmitted polarization due to interactions with scatterers [9]. In Section 6.2 of this chapter, a comparison between the co- and cross-polarized power distributions in terms of the AoA is made for the two NLOS scenarios selected for the experiment.

Previous attempts to characterize the indoor cross-polarization of signals were largely based on the assumption that depolarized components are uniformly distributed around the receiver location and are limited to the horizontal plane [1], [9]. In both cases that we

studied here, significant cross-coupling was measured where multipaths arrive with AoAs close to the vertical plane (θ ~30° or θ ~150°). The amount of power due to cross-polarized multipaths was estimated for a vertically polarized transmitter antenna located in different indoor environments. In Section 6.3, the advantages of using multi-element antennas and polarization diversity are studied in terms of the AoA distribution of cross-polarized components. Furthermore, the importance of the relative transmitter and receiver locations and the 3-D distribution of the nearest scatterers was also studied as part of this dissertation and some of the results have been presented in [24], [23].

Section 6.4 is dedicated to the study of the receiver signal-to-noise ratio (SNR) attainable after the coherent and noncoherent combining of the co- and cross-polarized MPCs. The performance comparison was made using the assumption of omnidirectional reception of vertically and horizontally polarized MPCs. It was estimated that a performance improvement of at least 2 dB in the received SNR could be achieved by intelligently combining orthogonally polarized signals. Furthermore, it was observed that when the receiver is unable to resolve multipath components, the coherent combination of two orthogonally polarized signals provides a consistent advantage over vertically or horizontally polarized omnidirectional reception. At higher bandwidths, the increased resolution improves the performance of all techniques however the dual polarization multipath combining retains its relative advantage over the other techniques.

6.2 RECEIVED POWER DISTRIBUTION

6.2.1 LOCATION A

The received power distribution when the transmitter is in location A is largely influenced by the EM waves scattering at the transmitter location which allows significant power coming from elevation angles outside the horizontal plane ($\theta = 0°$). Figure 6.1 shows the power distribution for both polarizations. These power distribution plots represent the normalized power distribution with respect to the maximum multipath power as a function of the AoA. Note that the 0° azimuth reference is normalized to the direction from the receiver location to the transmitter as shown in Figure 3.11. The maximum depolarization observed is concentrated on a power cluster below the horizontal plane located between 90° and 120° in elevation and 0° and 30° in azimuth as can be visually identified in Figure 6.1(a). There is a spatial overlapping between the cross-polarized MPC cluster and the maximum counterpart co-polarized power cluster as can be seen in Figure 6.1(b). However the power level of the horizontally polarized clusters is about -12 dB below the co-polarized cluster for the same azimuth AoA around the horizontal plane, for the low and high elevation angles, the co- and cross-polarized multipath are equivalent in power. The equivalent level of power for elevation angles outside the horizontal plane ($\theta \neq 90°$) can be explained by the reflection from floors and ceilings which create rotations in the E-field of the reflected multipath waves for those AoAs (Section 2.3).

At least ten distinguishable power clusters are identified in the horizontal plane with similar angular spread in azimuth, about 10°, as shown in Figure 6.1(b). The two clusters with the largest power are almost symmetrically located around 0° in azimuth. The maximum power co-polarized signal arrives from a single reflection from the wall in front of the auditorium exit as illustrated in Figure 3.13(2), which explains its large intensity. The second largest power cluster is due to direct transmission through the wall, which is partially blocked by a metallic plaque in that azimuth direction as can be appreciated in Figure 3.13(5). The third largest intensity cluster of co-polarized MPCs is located at -120° in azimuth and it can be attributed to reflections from the elevator metallic doors as seen in Figure 3.13(4). Reflection from the closed doors located at the south-east end of the lobby, as shown in Figure 3.13(6), creates the power cluster located at 180°. The co-polarized clusters located above and below the horizontal plane in Figure 6.1(b) can be associated with the vertical component of the E-field of reflected waves, which are consequently correlated with the horizontal components in Figure 6.1(a) for the same AoA. Notice that vertically polarized multipath clusters around the horizontal plane are present between 15° and 20° in elevation AoA spread ($\Delta\theta$). The largest $\Delta\theta$ belongs to the maximum power clusters located around $\varphi = 0°$.

Figure 6.2 shows the quantitative received power distribution for cross- and co-polarized MPCs in the azimuth AoA for different elevation angles. The AoA for co-polarized components shown in Figures 6.1(b) and 6.2(b) validate the assumption that vertically polarized signals are concentrated mostly on the horizontal plane [1], [62], [66]. However, horizontally polarized MPCs have larger $\Delta\theta$, i.e., they are not concentrated on the horizontal plane.

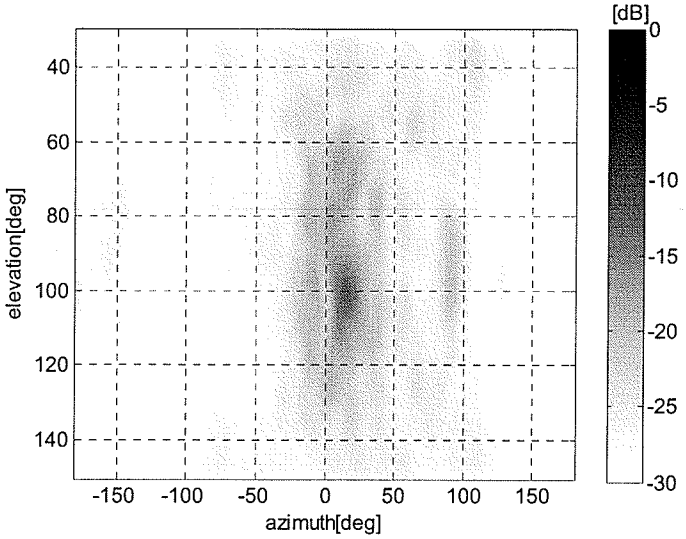

(a) Horizontal (cross-polarized).

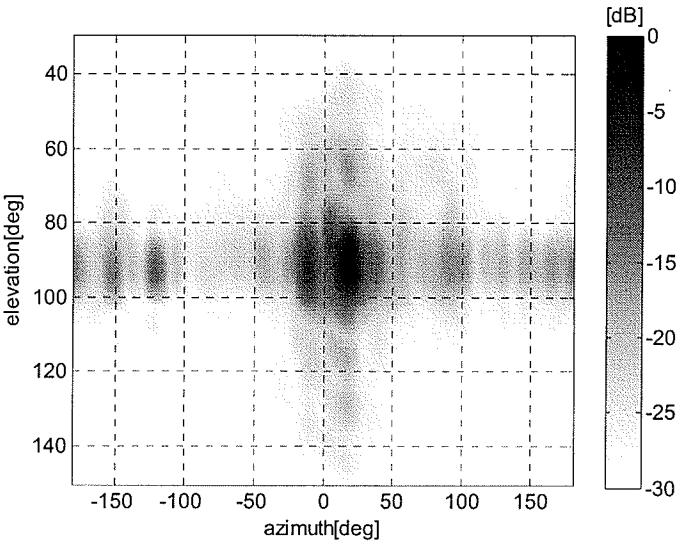

(b) Vertical (co-polarized).

Figure 6.1. Received power density as a function of AoA (location A).

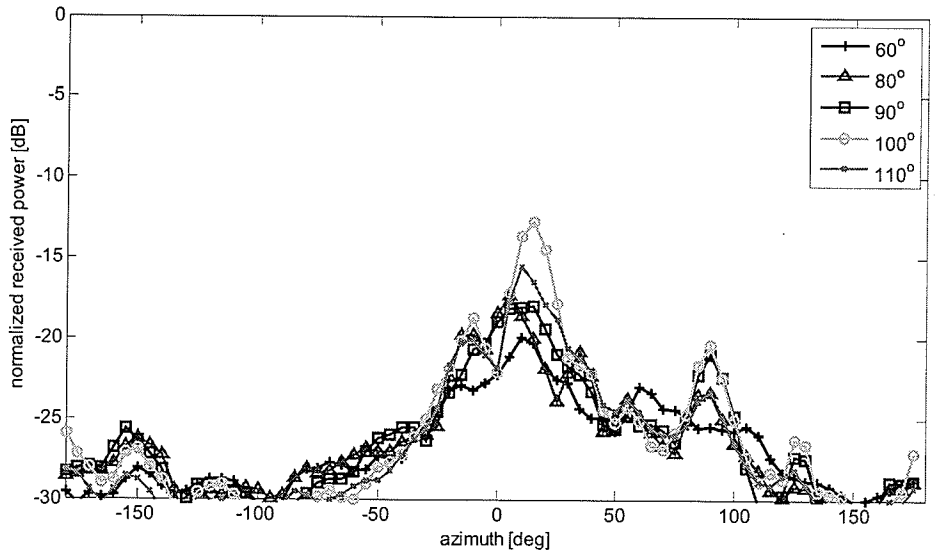

(a) Horizontal (cross-polarized).

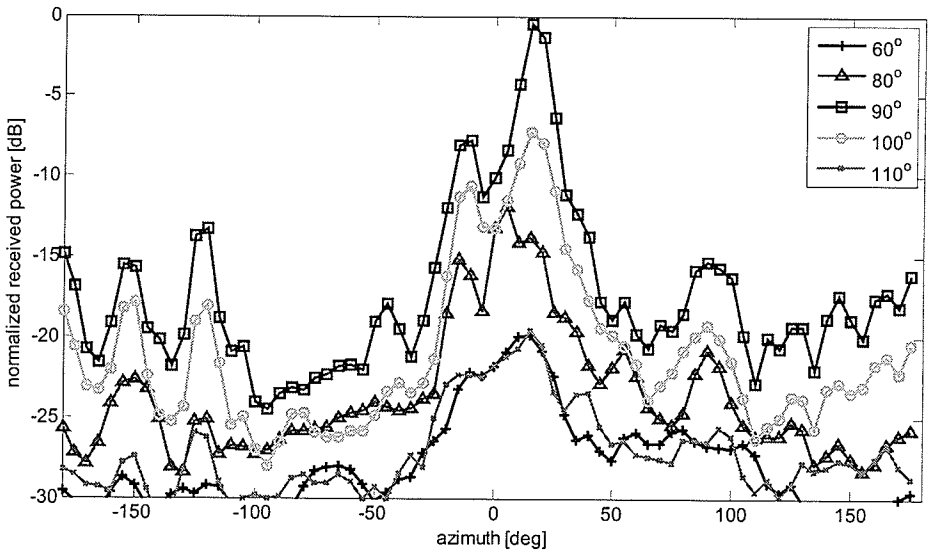

(b) Vertical (co-polarized).

Figure 6.2. Received power density as a function of the azimuth AoA (location A).

6.2.2 LOCATION B

The depolarization of MPCs when the transmitter is in location B exhibits even more elevation angular spread than in location A as shown in Figures 6.3(a) and 6.4(a). In some cases, the cross-polarized power surpasses the co-polarized power such as for the multipath clusters located at -110° in azimuth and 110°-120° in elevation. Two clusters located at 100° in azimuth and 100° and 120° in elevation, respectively, are originated by reflections from a metallic plaque behind the back wall shown in Figure 3.13(6). While the first the cluster at 100° elevation can be associated with MPCs with vertical and horizontal polarized components as shown in Figures 6.3(a) and 6.3(b), the cluster at about 120° elevation contains predominately cross-polarized MPCs.

The co-polarized MPCs distribution for this transmitter location is similar to those of location A as shown in Figures 6.3(b) and 6.4(b). In this case, eleven clearly differentiable power clusters are located in the horizontal plane. The angular elevation spread of these clusters varies from 10° spread in elevation to 25° for those clusters with maximum co-polarized power. As in location A, the two vertically polarized clusters with maximum power are approximately symmetrically located with respect to the direction of the transmitter. Another two clusters with significant power are located around -120° in azimuth which can be associated with reflection from the back wall as seen in Figure 3.13(6). Comparing the relative AoAs of vertically and horizontally polarized MPCs in Figures 6.4(a) and 6.4(b), respectively, it is possible to infer that depolarization can be associated mostly to signals with high and low elevation AoAs.

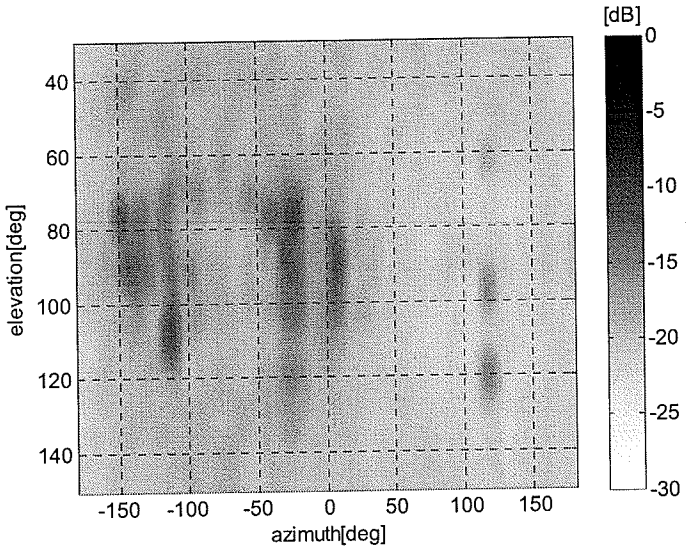

(a) Horizontal (cross-polarized).

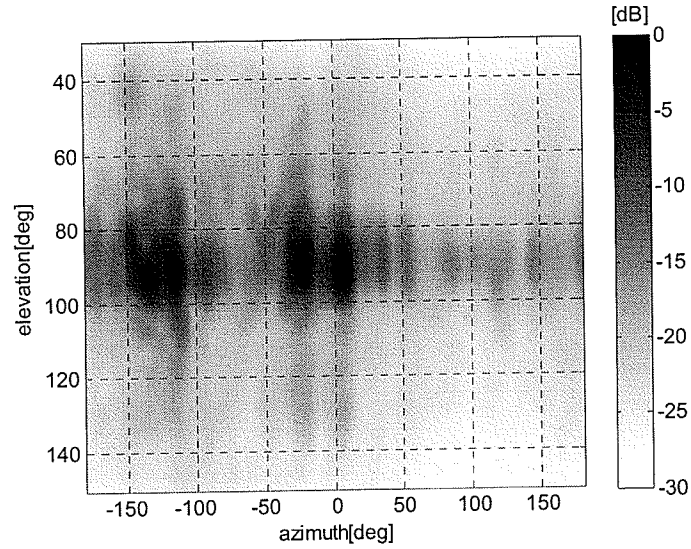

(b) Vertical (co-polarized).

Figure 6.3. Received power density as a function of AoA (location B).

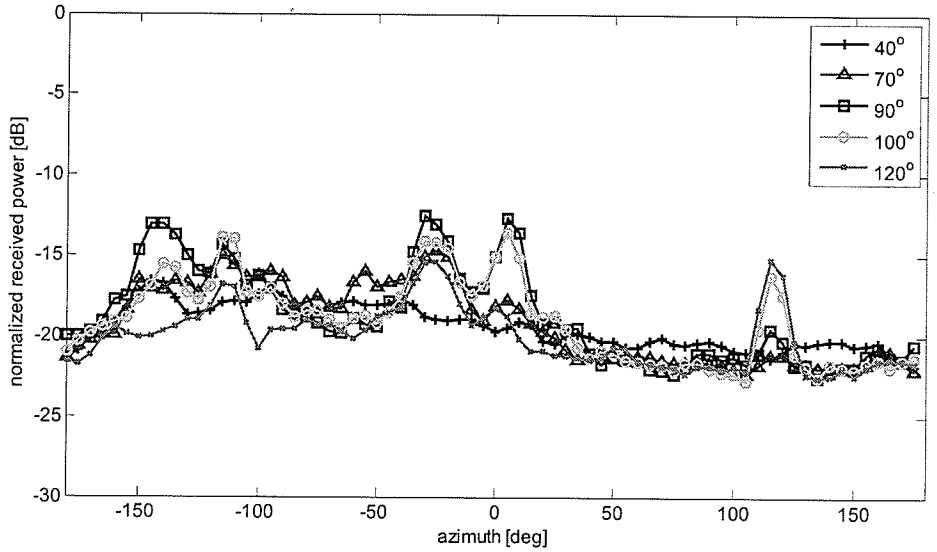

(a) Horizontal (cross-polarized).

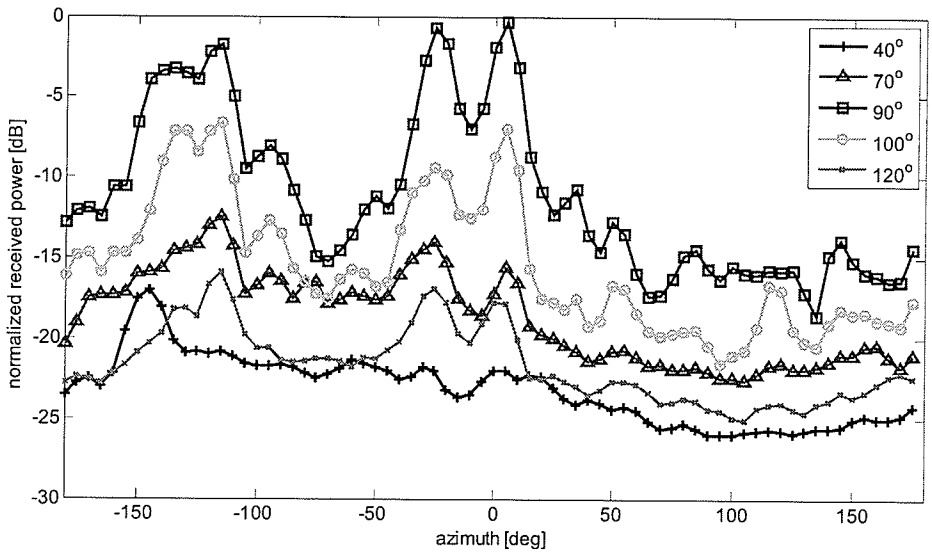

(b) Vertical (co-polarized).

Figure 6.4. Received power density as a function of the azimuth AoA (location B).

6.3 CROSS-POLARIZATION DISTRIBUTION AS A FUNCTION OF AOA

Each of the individual channel MPCs was extracted from the acquired CIR using the false alarm rate criterion as it was defined in Section 2.5. The large BW used in the experiment reduced the number of irresolvable MPCs that may be combined in each time bin causing channel fading. In order to simplify the analysis, the CIR defined in Section 2.4 can be written as a function of each discrete AoA as follows

$$h_i(\varphi,\theta,\tau)=\sum_{n=1}^{N}\sum_{m=1}^{M}\sum_{k=1}^{K}\alpha_i(n,m,k)\delta(\varphi-\varphi_n)\delta(\theta-\theta_m)\delta(\tau-\tau_k) \qquad (6.1)$$

where δ is the Dirac's delta function, the index i, such that $i = \{V, H\}$, is used to denote vertical or horizontal polarization, respectively, $\alpha_i(n,m,k)$ is the complex amplitude of the k^{th}-multipath, N, M, and K are the total number of resolution bins in azimuth, elevation and delay, respectively, φ_n and θ_m specify the discrete look angles, and τ_k is the k^{th} time sample of the multipath signal.

The total received coherent power as a function of AoA for both polarizations can be estimated using the CIR defined in (6.1) as follows

$$P_i^C(\varphi_n,\theta_m)=\sum_{k=1}^{K}\left|h_i(\varphi_n,\theta_m,\tau_k)\right|^2 \qquad (6.2)$$

The total coherent power as a function of each AoA is defined as

$$P_i^C(\varphi_n) = \sum_{m=1}^{M}\sum_{k=1}^{K}\left|h_i(\varphi_n,\theta_m,\tau_k\right|^2 \tag{6.3}$$

and

$$P_i^C(\theta_m) = \sum_{n=1}^{N}\sum_{k=1}^{K}\left|h_i(\varphi_n,\theta_m,\tau_k\right|^2 \tag{6.4}$$

The total noncoherent power as a function of the elevation and azimuth is defined as

$$P_i^{NC}(\varphi_n) = \sum_{k=1}^{K}\left|\sum_{m=1}^{M}h_i(\varphi_n,\theta_m,\tau_k)\right|^2 \tag{6.5}$$

$$P_i^{NC}(\theta_m) = \sum_{k=1}^{K}\left|\sum_{n=1}^{N}h_i(\varphi_n,\theta_m,\tau_k)\right|^2 \tag{6.6}$$

The distinction between the total coherent and noncoherent power is made here to compare the performance achievable by multi-antenna systems (MIMO) vs. single antennas in polarization-based communication systems.

The *XPOL* as a function of AoA can be defined as

$$XPOL(\varphi_n,\theta_m) = \frac{P_H^C(\varphi_n,\theta_m)}{P_V^C(\varphi_n,\theta_m)} \tag{6.7}$$

where P_H^C and P_V^C were defined in (6.2). In order to study the depolarization in azimuth and elevation using coherent and noncoherent power addition, the ratios

$$XPOL(\varphi) = \frac{P_H^i(\varphi)}{P_V^i(\varphi)} \tag{6.8}$$

and

$$XPOL(\theta) = \frac{P_H^i(\theta)}{P_V^i(\theta)} \tag{6.9}$$

were used, where P_H^i and P_V^i were defined in (6.3) and (6.4) for coherent power addition ($i = C$) and in (6.5) and (6.6) for noncoherent power addition ($i = NC$).

6.3.1 LOCATION A

The large number of scatterers in the transmitter location A creates reflections from ceiling and floors, increasing polarization decoupling for high and low elevation AoAs. As was explained in Section 5.2.1, the scatterers surrounding the transmitter at the auditorium (Figure 3.13(1)) originate multipath signals with diverse angles-of-departure. These scattered signals arrive at the receiver neighbourhood (Figure 3.12) after more than one reflection from the walls and ceilings and at least one transmission through the wall that divides the auditorium and the CRC main lobby (Figure 3.13(5)). Hence, these signals arrive much more attenuated than those echoes coming after a smaller number of interactions with the surrounding environment such as those originated in a single reflection in the wall outside the auditorium exit door (Figure 3.13(2)). The maximum *XPOL* coupling was created by the contribution of oblique reflected MPCs coming from the floor at low angle as shown in Figure 6.5 and Figure 6.6 for elevation angles above and below the horizontal plane. Less decoupling is observed in the horizontal plane as can be seen in Figure 6.6 for $\theta = 90°$ with a $\Delta\theta = 20°$. This effect can be expected

considering that reflections from walls, and even transmission through dielectric material commonly present in indoors, favours the propagation of co-polarized waves. On the other hand, the formation of cross-polarized signals occurs after a number of interactions with the indoor environment and therefore they arrive largely attenuated.

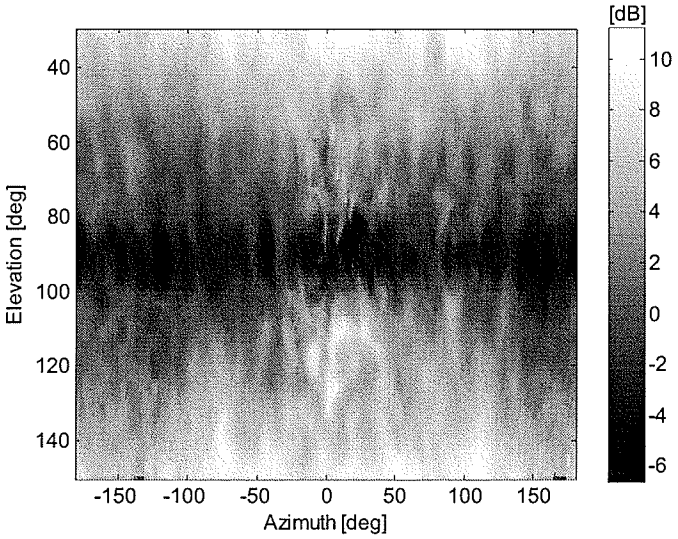

Figure 6.5. XPOL (location A).

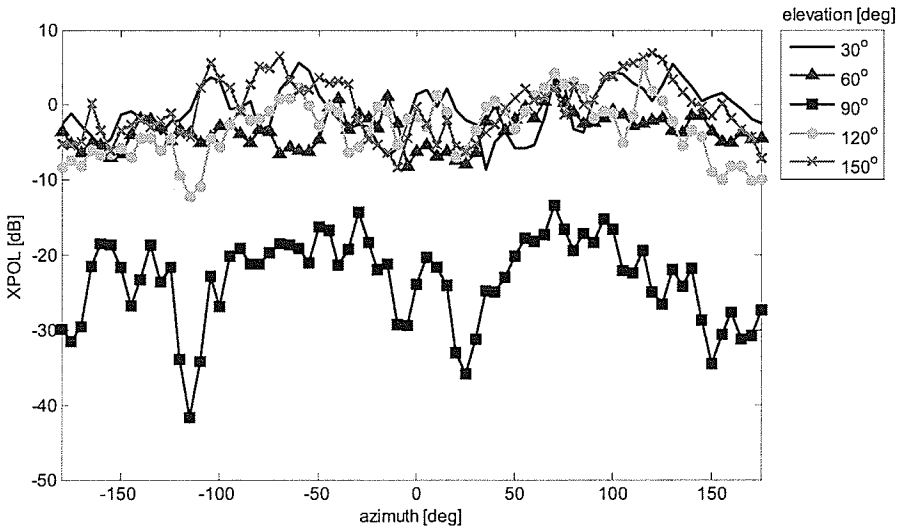

Figure 6.6. XPOL as a function of azimuth AoA (location A).

6.3.2 LOCATION B

Location B is an example of a sparse channel where the MPC interarrival times are larger than the binwidth. The topology of location B is comparable to a dielectric canyon which acts as a lossy waveguide favouring the propagation of vertically polarized components. Horizontally polarized multipaths caused by interactions in the transmitter surroundings arrive highly attenuated at the receiver. Therefore, the *XPOL* measured can be attributed to the decoupling of vertical components arriving in the receiver area from the horizontal plane after one or more interactions with the walls. The maximum depolarization was symmetrically located in two clusters above and below the horizontal plane around $\varphi = 120°$ as shown in Figure 6.7 and *XPOL* has a maximum for $\theta = 120°$ as can be seen in Figure 6.8. Oblique reflections from two metal panels perpendicularly oriented with respect to the wall explain the maximum *XPOL* concentration observed for that elevation angle. The cross-polarized distribution displays a distinctive pattern in both locations which can be appreciated when comparing the results shown in Figure 6.5 against those in Figure 6.7. Note that the maximum *XPOL* does not necessarily imply stronger horizontally polarized MPCs but, rather, may indicate the presence of weaker or the complete absence of vertically polarized MPCs. Furthermore, analyzing the power distribution of horizontally polarized multipaths, strong clusters of cross-polarized MPCs are found located closer, or even into, the region of minimum decoupling ($\theta = 90°$).

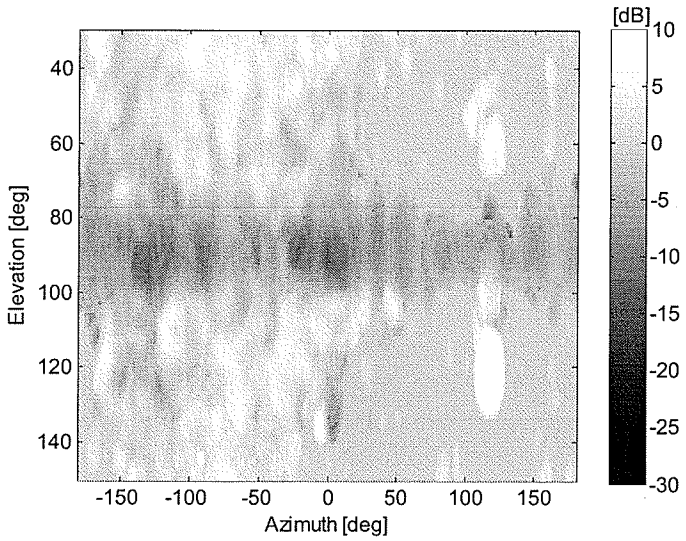

Figure 6.7. XPOL (location B).

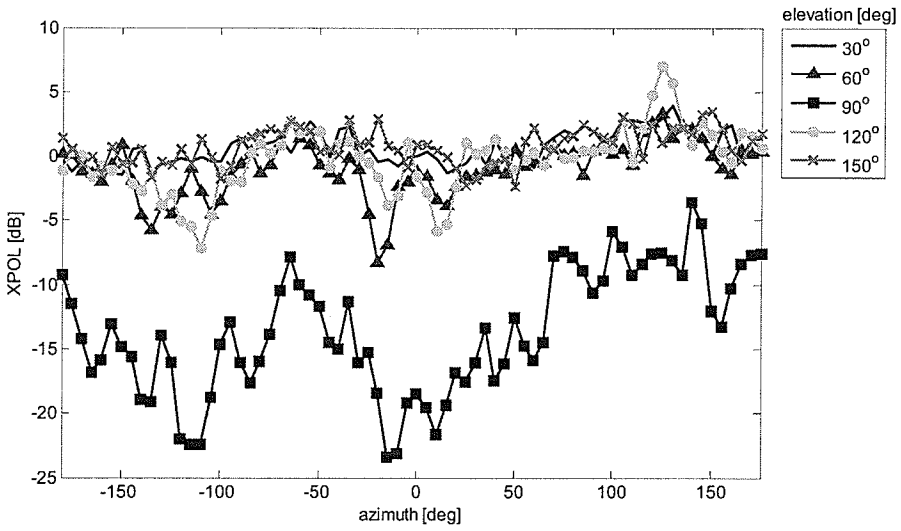

Figure 6.8. XPOL as a function of azimuth AoA (location B).

6.4 COMPARISON OF CROSS-POLARIZATION RESULTS FOR BOTH LOCATIONS

The amount of decoupling as a function of azimuth and elevation AoAs for both locations was estimated using the cumulative received power defined in (6.8) and (6.9), respectively. In both cases, the maximum decoupling occurs for MPCs coming from the ceiling and floors ($\theta < 40°$ and $\theta > 100°$) and the minimum depolarization is observed within $\pm 10°$ of the horizontal plane. The results of the noncoherent combination of MPCs are shown in Figure 6.9 while the coherent combination results are shown in Figure 6.10. Notice that similar decoupling is observed for signals in location A for coherent and noncoherent multipath combination. In contrast, decoupling is highly reduced in those MPCs in location B with sharp elevation angles for the noncoherent case which shows the limitation in the potential use of those decoupled MPCs by a narrow band system.

Tables 6.1 and 6.2 show the quantitative results for the total *XPOL* estimated for each location. The percentage of the total power received from horizontally polarized MPCs is larger in location A than in location B for coherent and noncoherent MPC addition. For location A, the coherent addition of multipaths enhances the *XPOL* about 1.4 dB, while the opposite effect is observed for location B with -1.6 dB *XPOL* variation.

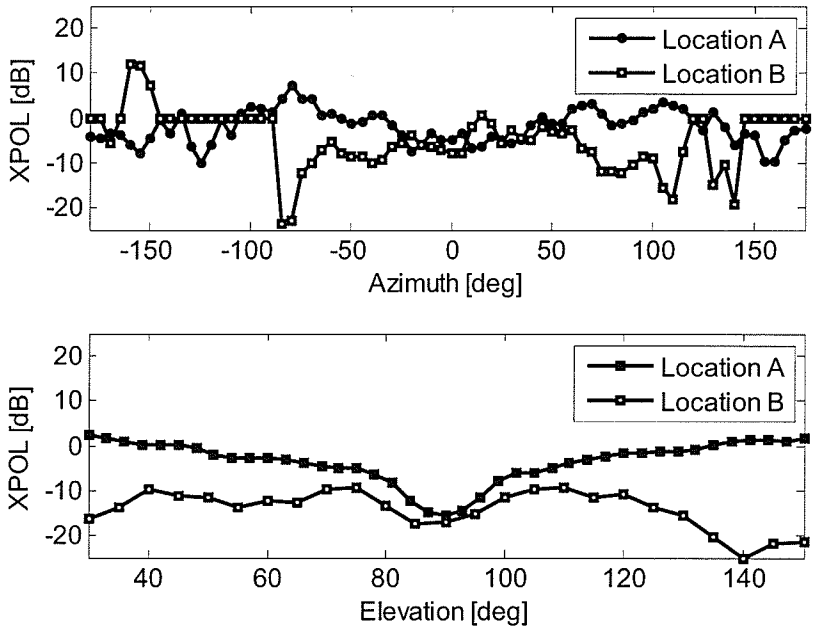

Figure 6.9. XPOL: noncoherent multipath combination.

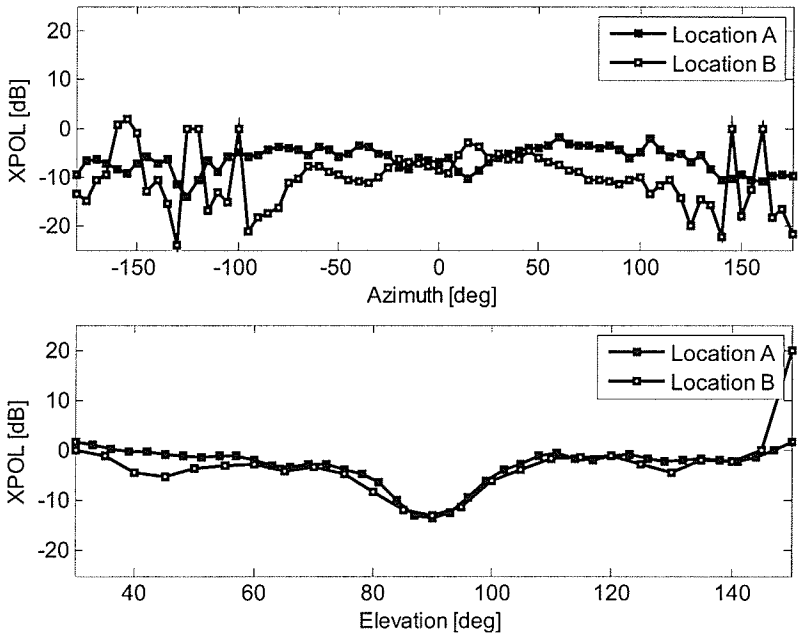

Figure 6.10. XPOL: coherent multipath combination.

A strong dependency of the cross-polarization of multipath components on the elevation AoA was observed for both transmitter locations. While co-polarized multipaths are confined exclusively to the region around the horizontal plane, cross-polarized MPCs can have sharp AoAs. Although the co-polarized MPCs are dominant in the horizontal plane for both locations, the cross-polarized components are uniformly distributed around the receiver for elevation AoAs close to the vertical as is seen in Figures 6.5-6.8. In rich scattering environments, MPCs are expected to arrive at the receiver location after one or more interactions with the surroundings. Furthermore, if these MPCs have elevation AoAs outside the horizontal plane, the probability that they have experienced reflections from the floor and ceiling is higher and so is the creation of cross-polarized MPCs. A vertically polarized wave will arrive at the receiver location co-polarized and confined mostly to the horizontal plane due to the waveguide effect of walls: this is the case in location B. Therefore, the probability of having cross-polarized components from scattering in the receiver surroundings is less than that of MPCs arriving after being subject to first or second order scattering and coming from above and below the horizontal plane, as in location A. Furthermore, the noncoherent addition of cross-polarized MPCs results in the destructive combination of these multipaths for location B as is evident in the *XPOL* as a function of the elevation AoA in Figure 6.9. This validates the assumption that for the particular propagation scenario of location B, cross-polarized components are created around the receiver area [54]. Consequently, scatterers located in the neighbourhood of the receiver location play an important role in terms of the creation of depolarized MPCs in a propagation scenario such as location B. In contrast, in location A, the noncoherent combination of MPCs does not destroy the

horizontally polarized signals for high and low elevation AoAs as is shown in Figure 6.9. The noncoherent combination of co- and cross-polarized signals maintains the same *XPOL* as the noncoherent combination for around the horizontal plane ($80° < \theta < 100°$), but favours depolarization for high and low elevation AoA as seen in Figure 6.10. A strategy to boost the capacity of a MIMO system might be to increase the total received signal-to-noise ratio (SNR) by collecting the otherwise wasted power due to cross-polarized MPCs [24].

Table 6.1. Noncoherent combination of MPCs.

Location	Rx Power	Co-polarized	Cross-polarized	*XPOL*
A	-16.1 dBm	81.2 %	18.7 %	-7.2 dB
B	-19.2 dBm	87.2 %	12.7 %	-8.9 dB

Table 6.2. Coherent combination of MPCs.

Location	Rx Power	Co-polarized	Cross-polarized	*XPOL*
A	-10.1 dBm	73.8 %	26.1 %	-5.8 dB
B	-15.2 dBm	91.1 %	8.8 %	-10.5 dB

6.5 CROSS-POLARIZATION IN INDOOR ENVIRONMENTS AND THE RECEIVED SNR PERFORMANCE

The distinct characteristics of co- and cross-polarized MPCs for indoor the two NLOS environments under study have been presented in Section 6.4. In this section, the received SNRs for coherent and noncoherent combining of the co- and cross-polarized multipath components are compared with those obtained for omnidirectional reception using vertically vs. horizontally polarized antennas. The channel measurement results for the transmitter in location B will be used in this study as seen in Figure 6.11.

In the previous section, it was concluded that the cross-polarized MPCs in indoor environments are mostly originated from the interaction of the transmitted signal with scatterers located in the proximity of the receiver. These cross-polarized multipaths are important not only for polarization diversity systems but also for their potential to boost the received power when a signal is transmitted with a single linear polarization. Polarization diversity systems generally exploit the EM wave polarization to multiplex data streams into separate channels [46]. When using this approach, cross-polarization degrades the performance by increasing the correlation between these channels [69]. On the other hand, in linear single polarization links, cross-polarized signals are normally ignored as negligible in comparison with the co-polarized received power. Based on the indoor channel data collected in both polarizations, the performance of vertically, horizontally and dual polarized, omnidirectional receptions were compared. For the case

of dual polarized reception, both coherent and noncoherent MPC combinations were considered. In many other studies, the indoor channel parameters were obtained using omnidirectional electric or magnetic dipoles [1] or, in some cases, ray-tracing simulations which include dipole-type omnidirectional radiation patterns [9]. The measurement system and signal processing technique provide channel characterizations that are independent of the radiation pattern, in addition to providing both magnitude and phase information for each AoA and delay sample. This information is necessary for the investigation of the influence of the spatial and temporal resolution of the receiver on the system performance. In the following analysis, the term *equal gain reception* refers to the ideal, direction independent and linearly polarized RF reception, without trying to simulate any real antenna. The case of dual polarized antennas with RF combining was simulated using noncoherent addition of the vertically and horizontally polarized signals arriving from every AoA, while coherent addition was used to evaluate the impact of smart baseband combining. For each case, the total power was calculated by adding the multipath signal coherently in the time domain for the maximum BW, which is equivalent to the maximum multipath delay resolution or the minimum time-binwidth.

The channel CIR for horizontally and vertically polarized signals given in (6.1) can be written as discrete functions as

$$h_i[n,m,k] = h_i(\varphi_n, \theta_m, \tau_k), \qquad i = \{V, H\} \tag{6.10}$$

where $n = 1, \ldots, N_\varphi$, $m = 1, \ldots, N_\theta$, $k = 1, \ldots, N_\tau$, the total number of samples in φ, θ, τ, respectively, are $N_\varphi = 360$, $N_\theta = 150$, $N_\tau = 400$. The equal gain reception of received

signal was calculated as the noncoherent combination of multipaths arriving from every discrete AoA as follows

$$s_i[k] = \sum_{n=1}^{360} \sum_{m=1}^{150} h_i[n,m,k], \qquad i = \{V, H\}. \tag{6.11}$$

The equal gain reception of vertically and horizontally polarized power as a function of the time-bin duration Δ was calculated as

$$P_i^C[\Delta] = \sum_{l=1}^{(N_\tau/\Delta)-1} \left| \sum_{k=\Delta l+1}^{\Delta(l+1)} s_i[k] \right|^2, \quad i = \{V, H\}. \tag{6.12}$$

where Δ is the time-binwidth in number of channel samples, N_τ is the total number of time-bins for the maximum resolution, in this case N_τ = 400. The equal gain, dual polarized multipath combination as a function of the time binwidth is defined as

$$P^C[\Delta] = \sum_{l=1}^{(N/\Delta)+1} \left(\left| \sum_{k=\Delta l+1}^{\Delta(l+1)} s_V[k] \right|^2 + \left| \sum_{k=1}^{\Delta(l+1)} s_H[k] \right|^2 \right) \tag{6.13}$$

$$P_i^{NC}[\Delta] = \sum_{l=1}^{(N/\Delta)+1} \left| \sum_{k=\Delta l+1}^{\Delta(l+1)} s_V[k] + s_H[k] \right|^2 \tag{6.14}$$

The coherent combination of vertical and horizontal received signal is represented by (6.13) while the noncoherent combination is represented by (6.14).

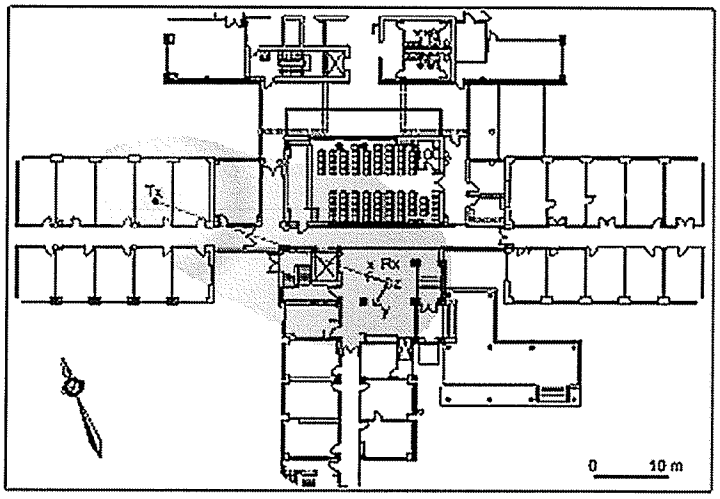

Figure 6.11. Transmitter location chosen for the SNR vs. time bin characterization.

The relationship between the receiver performance and its time resolution is shown in Figure 6.12. While the coherent combination of orthogonally polarized signals maintains its advantage for decreasing temporal resolution, the noncoherent combination exhibits fluctuations in the SNR performance. The points marked as A-C in Figure 6.12 coincide with the clusters arrival delays seen in Figure 6.13. For these delays, cross-polarized and co-polarized MPCs are combined destructively in the same time bin, degrading the performance. In contrast, the coherent combination of both orthogonally polarized signals avoids this destructive effect for the same delays and outperforms the other techniques. However, when the MPC addition in some time-bins leads to vertical and horizontal signals close in phase, the noncoherent addition of the resultant orthogonally polarized components can be higher than the coherent combination of both signals. This occurs for instance, when the time-binwidth is 50 ns, 70 ns, 100 ns, and 180 ns, (e.g. case E in

Figure 6.12), then the noncoherent addition of orthogonally polarized MPCs outperforms the coherent combination.

The received SNR performance for low multipath resolution (Figure 6.12), or equivalently, low channel BW, exhibits a larger difference between the equal gain reception of both singularly polarized components, favouring the co-polarized MPCs. Larger time-binwidth (low temporal resolution) results in the noncoherent combination of a larger number of cross-polarized MPCs, leading to the mutual cancellation of multipaths. This effect is explained by cross-polarized MPCs, which after being created by scattering around the receiver area (Figures 5.1 and 5.3), have random phases and exponentially decaying magnitudes between each power cluster, whose maximum MPC power are comparable within clusters in some cases as can be seen in the example given in Figure 5.24. The dual noncoherent combination of both vertical and horizontal signals causes the SNR performance to decrease even further for time-binwidths larger than 230 ns, which is the duration of the multipath signal. This can be attributed to the destructive effect of the orthogonally polarized noncoherent addition. The dual coherent combination is the best combination strategy for low multipath resolution.

For high channel BW, the noise power increases making the SNR worse despite the increase in received power. Figure 6.14 shows the high temporal resolution performance in terms of the received SNR. Note that for small time-binwidth, the equal gain reception of vertically and horizontally polarized MPCs leads to similar performance. This effect can be explained by the spatial power distribution for both polarizations. Even though the individual cross-polarized MPCs are 10 dB below the maximum co-polarized MPCs, their AoAs are more spread in azimuth and, particularly, in elevation. Therefore, for high

time resolution, fewer MPCs are destructively combined in each time-bin, leading to a higher signal level than in the case of low resolution where this destructive effect cannot be avoided. Furthermore, the higher the resolution, the closer the performance achieved for dual coherent and noncoherent signal combination, providing a constant 2 dB gain in comparison with the equal gain reception of the co- or cross-polarized signals.

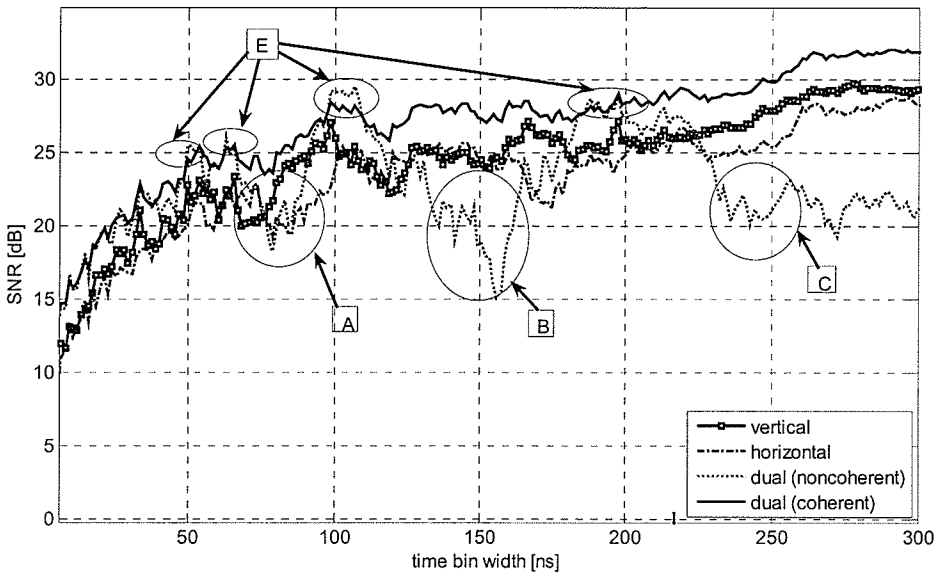

Figure 6.12. Received SNR vs. time-binwidth.

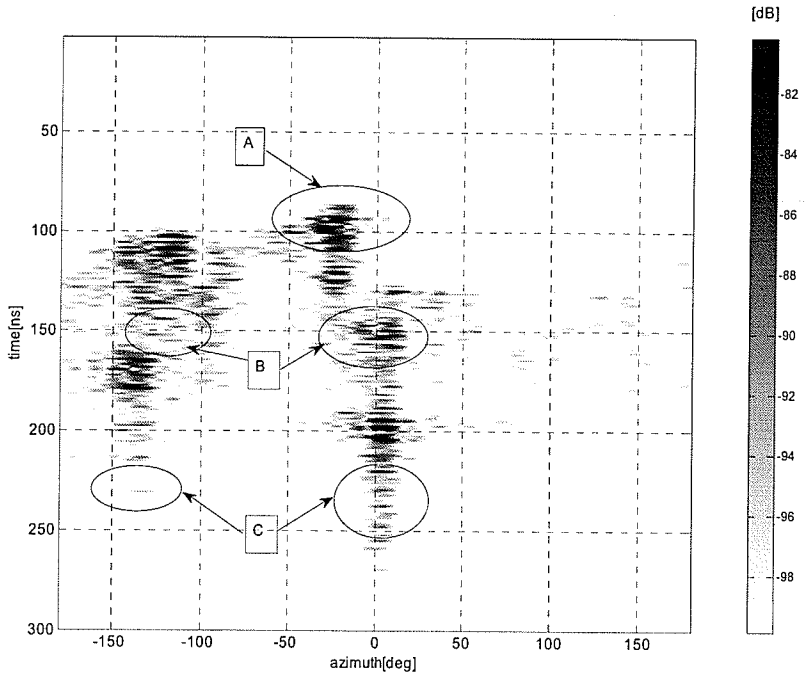

Figure 6.13. Receiver power clusters, vertical polarization (location B).

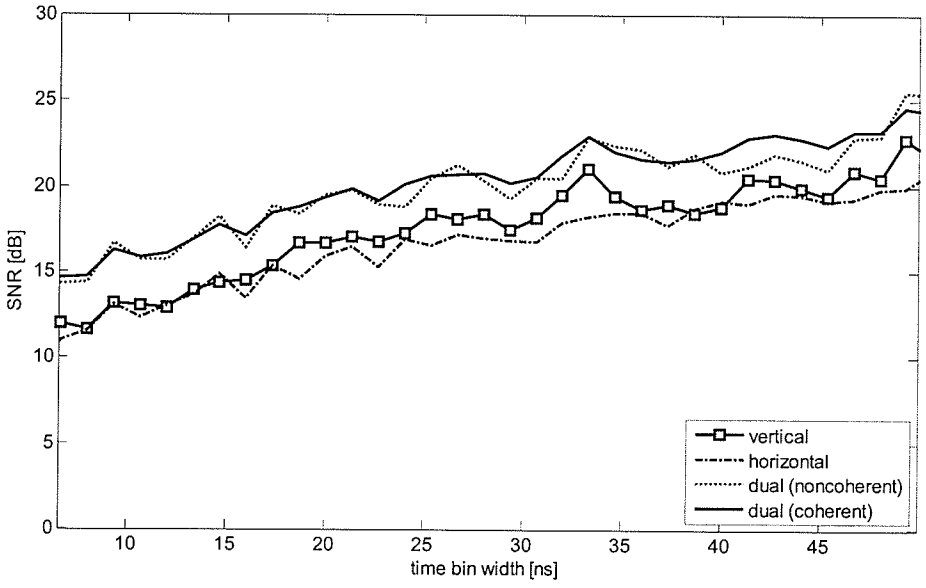

Figure 6.14. SNR vs. time-binwidth for high temporal resolution.

Table 6.3. Total coherent multipath power.

Combining technique	Received power [dBm]
Vertical	-49.1
Horizontal	-50.0
Dual (noncoherent)	-47.0
Dual (coherent)	-46.5

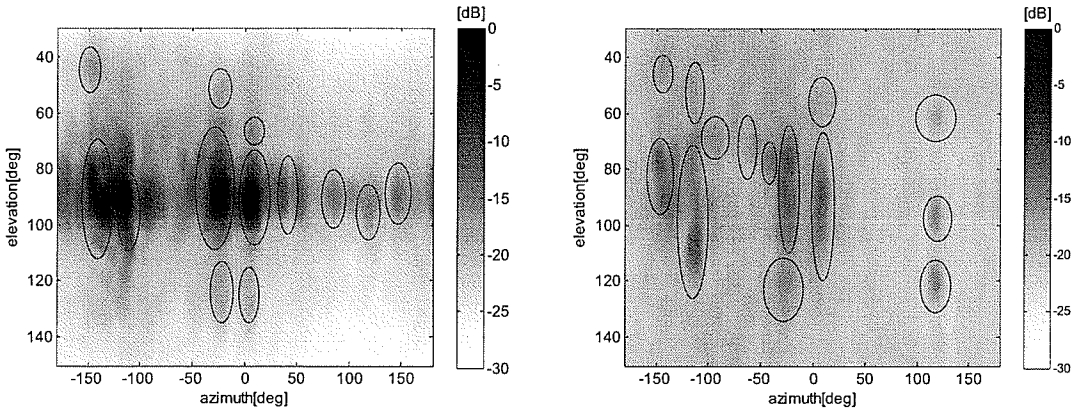

(a) Vertical (co-polarized). **(b) Horizontal (cross-polarized).**

Figure 6.15. Clusters for co- and cross-polarized reception for the transmitter in location B.

The total power distribution as a result of the coherent addition of MPCs for both polarizations is shown in Figure 6.3 for this transmitter location. Note that, while vertically polarized MPCs are distributed in the proximity of the horizontal plane, cross-polarized components appear in clusters that are more uniformly distributed with respect to the elevation AoA as is shown in Figure 6.15. After combining the information

obtained from Figures 6.3(a) and 6.3(b), the *XPOL* as a function of the elevation and azimuth AoAs was determined (Figure 6.7). The higher *XPOL* can be associated with multipaths coming from above and below the horizontal plane. This does not necessarily imply the presence of horizontally polarized MPCs with significant strength coming from elevation AoAs above and below $\theta = 90°$ but the relative absence of co-polarized MPCs for those AoAs, which is consistent with the observations presented in Section 6.2.

6.6 SUMMARY OF RESULTS AND CONCLUSIONS

The performance attainable for different approaches to combine polarized MPCs was presented in this chapter. The coherent combination of MPCs from the equal gain reception of co-polarized and cross-polarized signals increased the received SNR for a NLOS indoor environment. This improvement was possible due to the significant amount of signal power that is decoupled into orthogonally polarized MPCs [23]. The coherent combination of two polarized signals exhibits better performance than the single polarization combination in most cases. The creation of cross-polarized signals around the receiver area with randomly distributed phases and comparable magnitudes contributes to the cancellation of MPCs when added noncoherently for large time-binwidths. The result is a performance advantage for the equal gain reception of co-polarized components over the cross-polarized and dual noncoherent polar combination

for low BW. However, the coherent combination of equal gain reception of co- and cross-polarized components still provides a performance advantage which has to be counterbalanced by the increased complexity of the antenna system.

Clusters of significant power arriving from diverse AoAs at different delays for each polarization were observed in both locations. These clusters of MPCs are added destructively reducing the significance of the noncoherent polar combination. Furthermore, it was estimated that the total power of vertically polarized signals with equal gain reception for large bin-widths is reduced considerably, again because of the destructive addition of MPCs arriving simultaneously from distinctive AoAs. It is possible to eliminate this destructive effect, taking advantage of the rich scattering indoor environment, by combining multi-beam antenna systems and polarization diversity at the same time.

In addition, a strong dependency of the cross-polarization of multipath components on the elevation AoA was found. While vertically polarized signals are confined exclusively to the region around the horizontal plane, cross-polarized signals are more spread in their elevation AoA. The latter can be explained by reflections from floors and ceilings in the surroundings of the receiver. It can be concluded that the spatial distribution of the scatterers in the proximity of the receiver is a decisive factor in the creation of decoupled MPCs.

7 CONCLUSIONS

This dissertation presented the results of a measurement campaign designed to characterize the wireless channel for distinctive indoor scenarios to study the space-time-polarization diversity. Using a channel sounding platform designed for this purpose, the results were presented in terms of the AoA power distribution, the joint AoA-ToA power distribution and the delay statistics as functions of the AoA for co- and cross-polarized received signals. In addition, the depolarization of MPCs in the two indoor scenarios was studied in terms of the AoA and ToA. In this concluding chapter, the most important results for the space-time-polarization characterization and possible directions for future research work will be summarized.

7.1 RECONSTRUCTION OF THE CHANNEL RESPONSE

Using the high resolution method proposed in Chapter 4, the spatial and temporal response of the indoor channel was reconstructed for both polarizations. To control the number of iterations on each recursion a modification of the CLEAN process was proposed. Using this innovation, the total energy subtracted from the signal was adaptively minimized, diminishing the possibility of false identification of MPCs. The antenna radiation patterns and the cross-polarization rejection, which were properly characterized for the frequency band used in this experiment, are particularly good for this type of sequential channel sounding. However, this technique of signal interpolation and deconvolution can be used even in cases where the antenna SLL is high enough to introduce considerable interference from distinctive AoAs. If the radiation patterns change with the scanning angle, such as the cases of using beamforming to scan to different AoA, this method can be used to detect the dominant MPC's AoA providing the radiation pattern is sufficiently well characterized. A variation of the CLEAN algorithm called *sequential CLEAN* was also evaluated, but it was found that the modified CLEAN outperforms this alternative algorithm for this application.

It is left for future work to test this technique for other directive antennas and arrays in cases where the scanning angle independency of the antenna response does not hold and when the cross-polarization rejection response needs to be compensated. The capabilities

of this technique to mitigate the antenna near-field distortive effects on the indoor channel characterization are another aspect that needs to be studied in more detail.

7.2 JOINT AOA-TOA POWER DISTRIBUTION

The joint azimuth-elevation AoA power distribution as a function of the delay exhibits similar patterns in both indoor scenarios. It was seen that the first waves to arrive are grouped in clusters of power on and outside the horizontal plane for both polarizations justifying the assumption that the predominant cause of depolarization is the reflection from floors and ceilings of MPCs arriving from the shortest path (shortest excess delay). However, the co-polarized MPCs tend to be concentrated in the clusters located on horizontal plane for longer excess delays while depolarized signals are more wide spread in elevation AoA. The co-polarized signals arriving in the horizontal plane ($\theta = 90°$, $\varphi \in [0°, 360°)$) exhibit maximum signal excess delays in both locations (175 ns and 225 ns for locations A and B, respectively). The cross-polarized signals, in contrast, exhibit maximum excess delays of about half of those of co-polarized for the same AoA (87 ns and 110 ns, for locations A and B, respectively). The signals with maximum excess delays are those that had more interactions with the environment. Hence, co-polarized signals are more likely to arrive at the receiver area with larger excess delays than cross-polarized signals. This result may be explained by walls acting as *lossy waveguides* favouring the co-polarized signal propagation. Cross-polarized signals

originated in the transmitter area have less power and they are attenuated beyond detection before arriving at the receiver. Therefore, the measured cross-polarization phenomena take place in the receiver neighbourhood as a result of depolarization of co-polarized signals which are more likely to arrive at the receiver neighbourhood with enough power to be detected.

The ToA statistics estimated for the transmitter at location A (auditorium) show that cross-polarized signals exhibit uniform properties in terms of PWMED and RMS delay spread as a function of the azimuth AoA for a given elevation angle. The median value for both PWMED and RMS delay spread are 20 ns for cross-polarized MPCs. In contrast, the co-polarized MPCs are more densely concentrated near the horizontal plane ($60° < \theta < 120°$) and over restricted azimuth angles ($-50° < \varphi < 50°$). The median value for the PMWED is 25 ns while the median RMS delay spread is 30 ns for co-polarized signals when the transmitter is in location A. For the transmitter at location B (office), the ToA statistics show maximum peaks located on the horizontal plane in both polarization cases. For other AoAs, the ToA statistics account for anomalous effects such as isolated co-polarized clusters that create peaks in the estimated values. Similar behaviour in term of ToA statistics for both polarized MPCs is seen when the transmitter is at location B. The maxima of the delay statistics can be explained by the concentrations of MPCs in clusters with similar maximum power.

7.3 POWER DISTRIBUTION VS. AOA AND DEPOLARIZATION IN INDOOR CHANNELS

The analysis of the results from both locations shows that the co-polarized MPCs appear in clusters of power around the horizontal plane with an elevation spread of ~20° in both locations. Clusters of co-polarized MPCs outside the horizontal plane ($\theta = 90°$) were found in both transmitter locations even though the propagation scenarios are quite different. The azimuth AoA of power clusters suggests a uniform distribution within [0°, 360°). In contrast, the cross-polarized MPCs clusters have larger elevation spread and are not restricted to the horizontal plane as is the case of co-polarized MPCs. Even though the cross-polarized signals are stronger in the neighbourhood of the horizontal plane, they were also found outside these elevation AoAs.

As a result of the equal gain reception of MPCs, the resultant co-polarized signal level was reduced significantly due to destructive noncoherent addition. In contrast, the opposite effect was observed for cross-polarized MPCs which were enhanced after the noncoherent combination. This could be explained by a higher phase correlation of cross-polarized components arriving from different AoAs.

7.4 On the Use of Cross-Polarized Signals to Improve Indoor Reception Performance

One possible strategy to boost the capacity in indoor channels consists of intelligent combining of co- and cross- polarized signals and antenna beamforming techniques. The power clusters for both polarizations and their relative angular spreads suggest that, for co-polarized reception, a multi-beam system can be implemented to sectorize the reception around the horizontal plane. Using this strategy, the spatial correlation of co-polarized clusters that appears around $\varphi = 90°$ can be used to maximize the signal reception. The same strategy can be implemented for cross-polarized components but this time favouring a wider elevation AoA. The coherent combination of both polar signals, when the BW is large enough to make the use of cross-polarized MPCs attractive, can be used to improve the performance.

7.5 Thesis Contributions

The work reported herein was supported by Defence Research and Development Canada (DRDC), Natural Sciences and Engineering Research Council (NSERC) and the University of Manitoba. The receiver antenna used in the AZELTI channel sounder platform was provided by the Advanced Antenna Technology research group of the

Communications Research Centre (CRC) in Ottawa. The receiver patch antenna radiation patterns characterization for both, far and near fields was provided by Dr. A. Petosa and S. Raut from the same group. The control system for the AZELTI platform was developed by C. Squires from the Terrestrial Wireless Systems branch (CRC) who also helped in the acquisition of material and building of the sounder platform, in addition to providing technical support during the measurement trials.

The most important contributions of the thesis can be summarized as:

- The main idea of the project, which is the characterization of the indoor wireless channel in terms of AoA, ToA and polarization to collect enough information to support improvements of existents and new channels models for indoor propagation;

- The design, evaluation, test, and calibration of the indoor channel sounder, as well as the selection of the in indoor locations to provide different propagation scenarios for the experiment;

- The modification of the CLEAN deconvolution algorithm to control the number of iterations of each recursion by adaptively modifying the amount of energy subtracted from the original signal after each cycle;

- The identification of the main power cluster angular distributions and spread for co- and cross-polarized components in terms of the propagation processes that take place for each location;

- The identification of the main processes involved in the creation of depolarized MPCs in indoor environments, such as the relative distribution of scatterers surrounding transmitter and receiver and their EM properties;

- The analysis of the total cross-polarization as a function of the AoA;

- The measurement of the excess delay spread and RMS delay spread in azimuth and elevation for co- and cross-polarized signals, and the resulting degradation in performance by the presence of the spatio-temporal clusters of MPCs;

- The estimation of the receiver SNR performance as a function of the channel bandwidth, or equivalently, the delay resolution, from the equal gain reception of signals of co-, cross- and dual polarization reception;

- The proposal of an alternative method of coherent combining of MPCs with polarization diversity that could lead to significant performance improvements for linearly polarized transmitted signals in indoor channels.

The development of innovative sounding and post-processing techniques for the characterization of indoor channels with high resolution in terms of AoA, ToA, and polarization provided a tool for studying of the interrelation between propagation physics and space-time-polarization diversity. The results of this project may potentially have a tremendous impact on proposal and verifications of indoor channel models.

This research work has been presented partially in the Canadian Conference of Electrical and Computer Engineering [23] (CCECE06), Ottawa, May 2006, and in ANTEM/URSI [24], Montreal, July 2006.

APPENDIX A: THE RECEIVER ANTENNA

A.1 RECEIVER ANTENNA SCHEMATIC

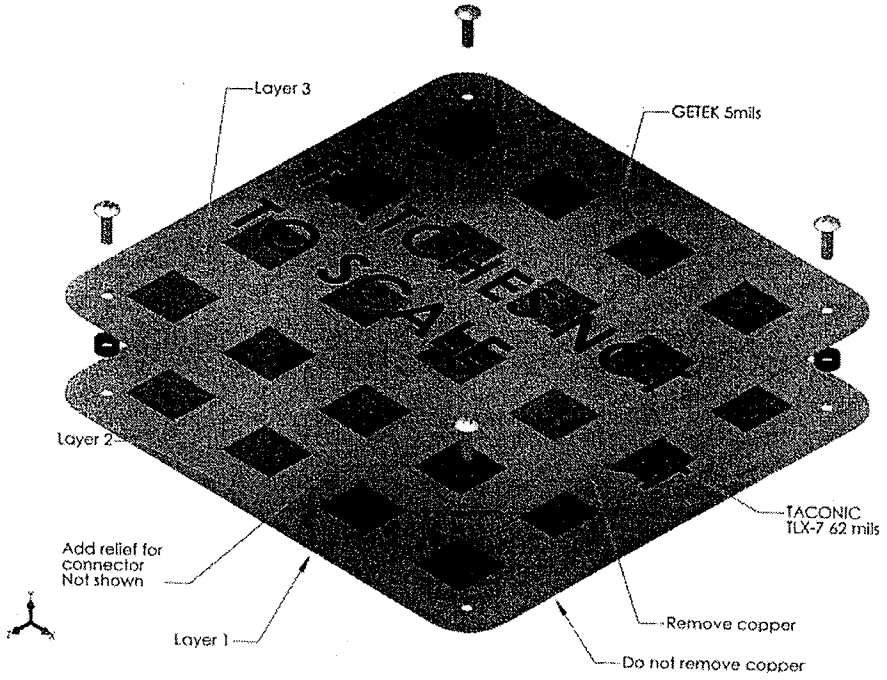

A.2 RADIATION PATTERN (5.10 GHz)

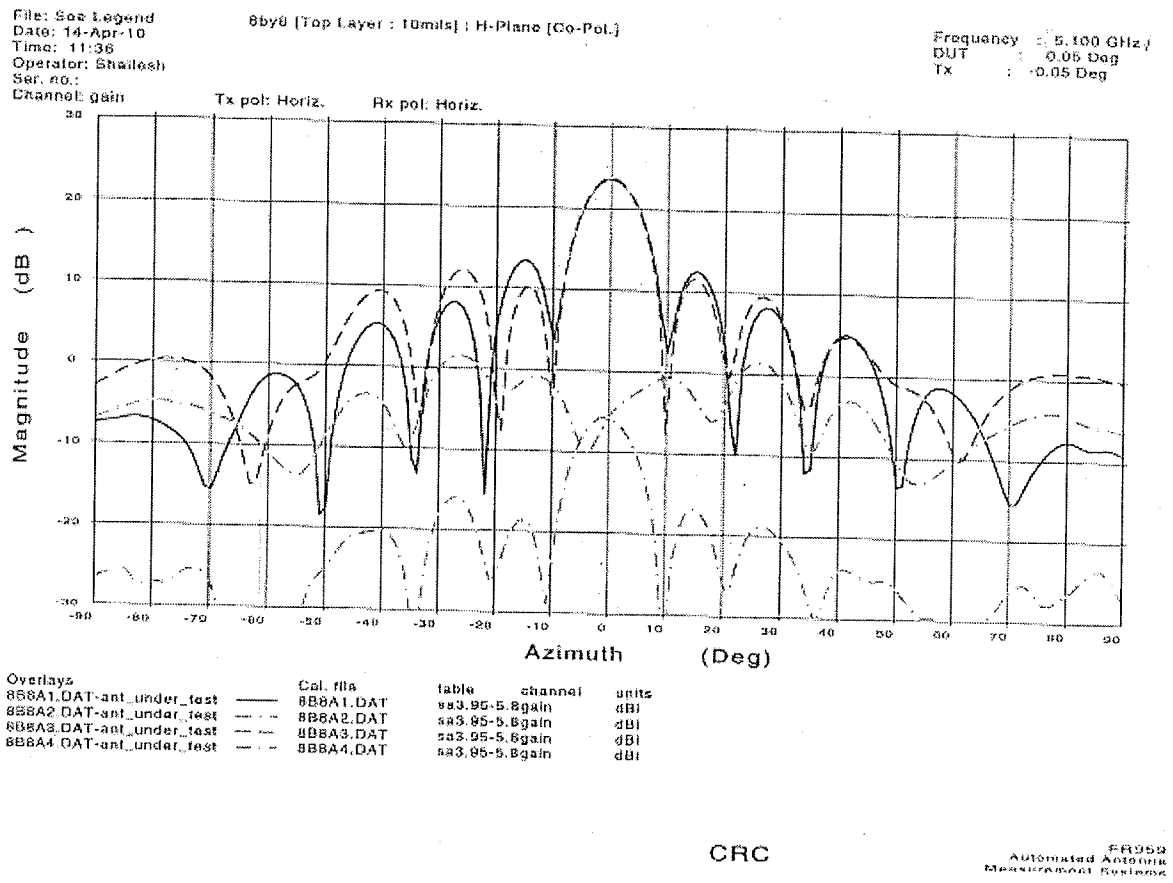

A.3 RADIATION PATTERN (5.15 GHZ)

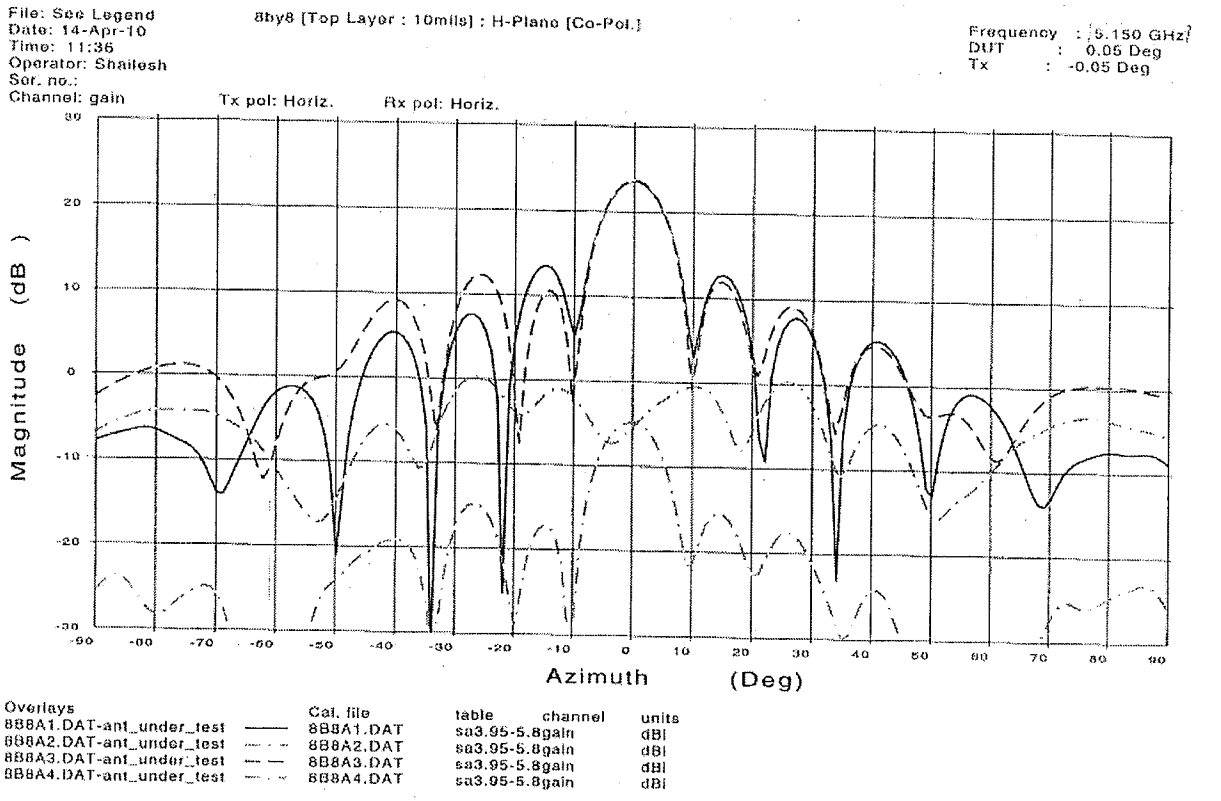

CRC

FR959
Automated Antenna
Measurement Systems

A.4 RADIATION PATTERN (5.20 GHZ)

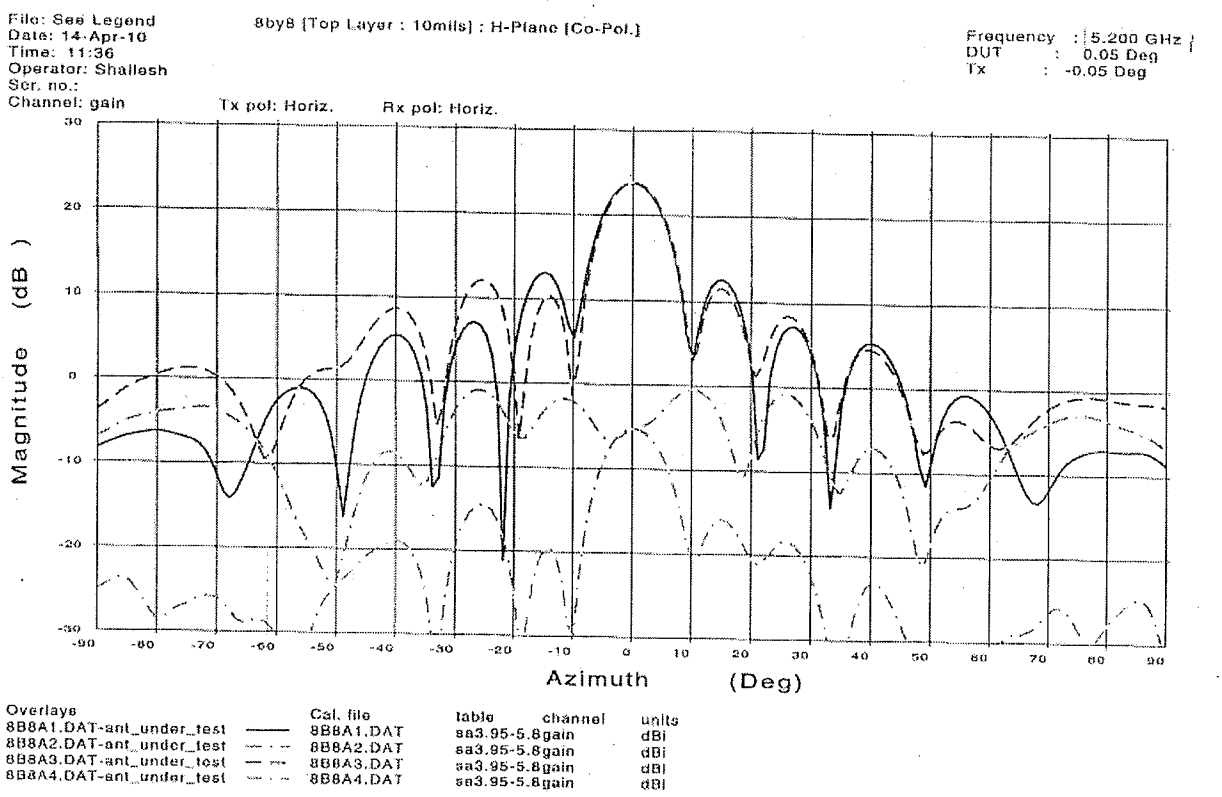

CRC

FR959
Automated Antenna
Measurement Systems

A.5 RADIATION PATTERN (5.25 GHz)

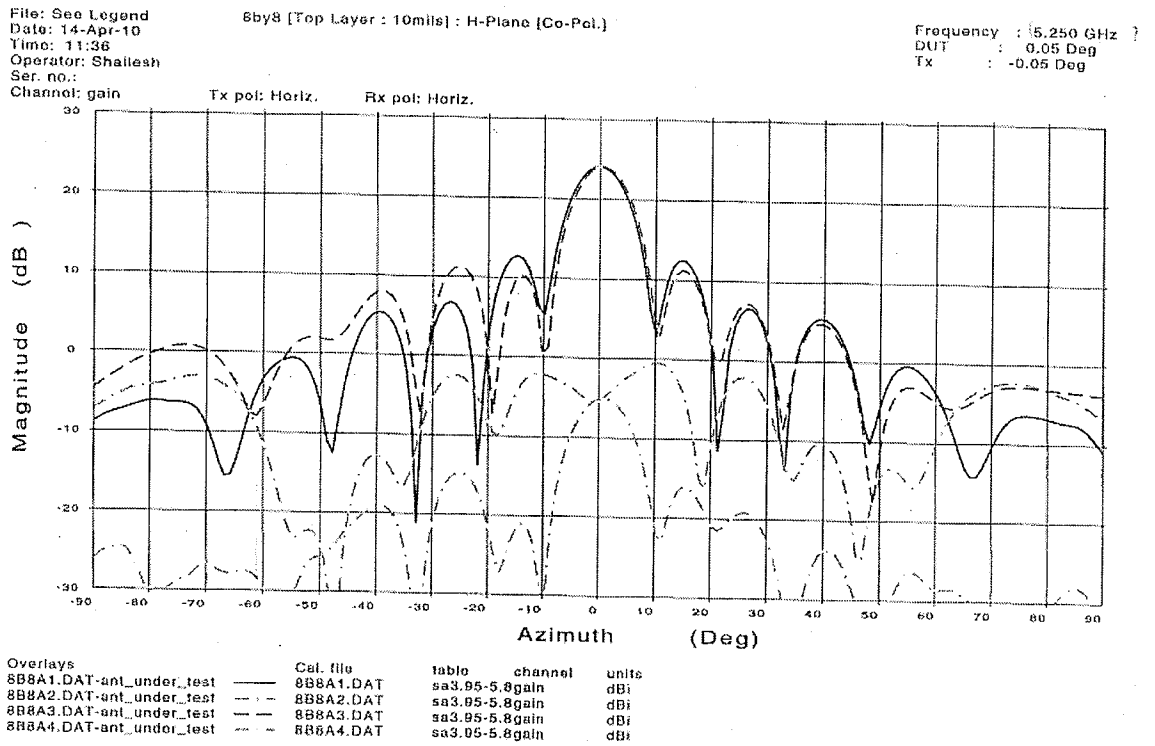

CRC

FR959
Automated Antenna
Measurement Systems

A.6 RADIATION PATTERN (5.25 GHZ)

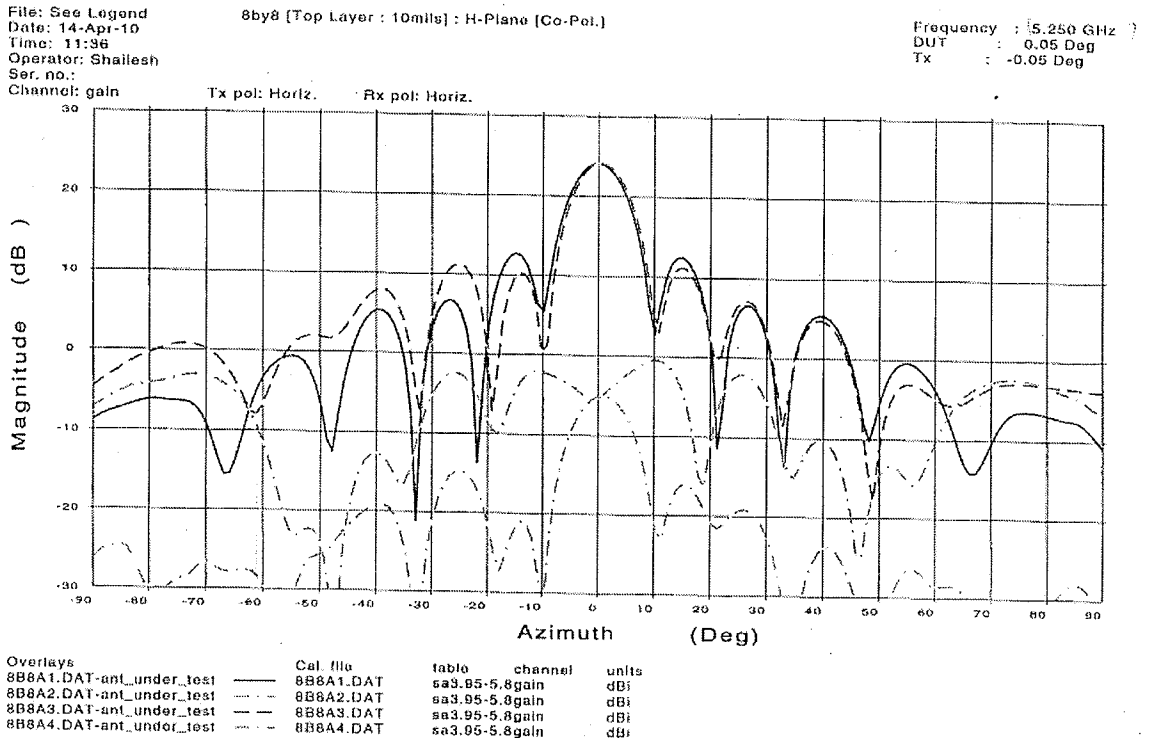

A.7 RADIATION PATTERN (5.30 GHZ)

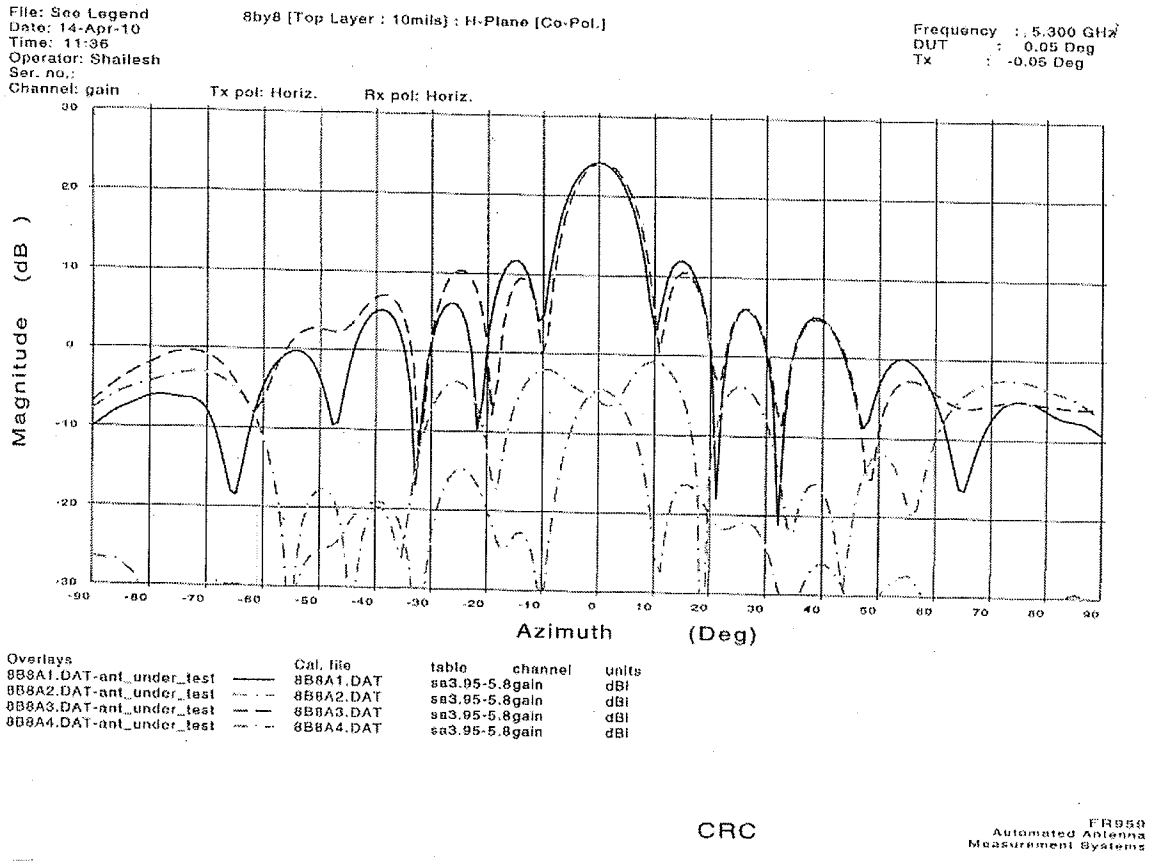

A.8 RADIATION PATTERN (5.35 GHZ)

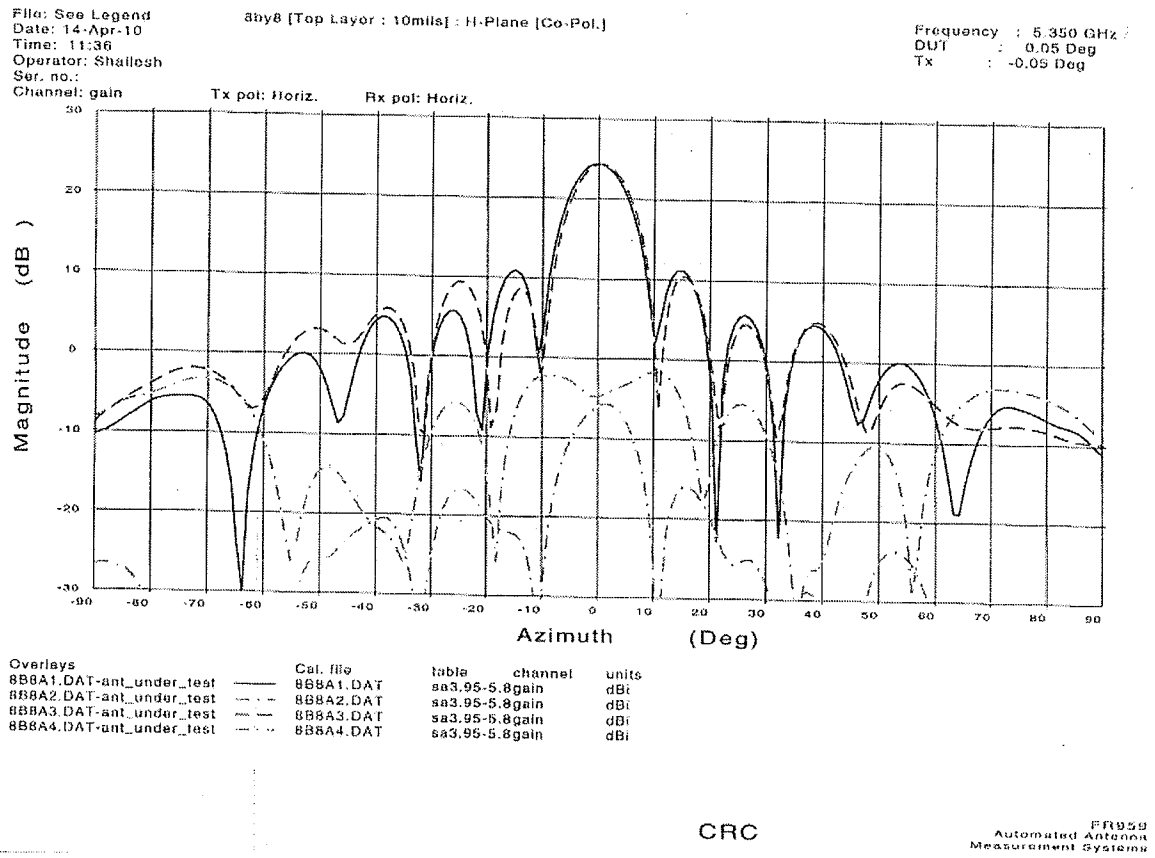

CRC

FF959
Automated Antenna
Measurement Systems

A.9 RADIATION PATTERN (5.40 GHZ)

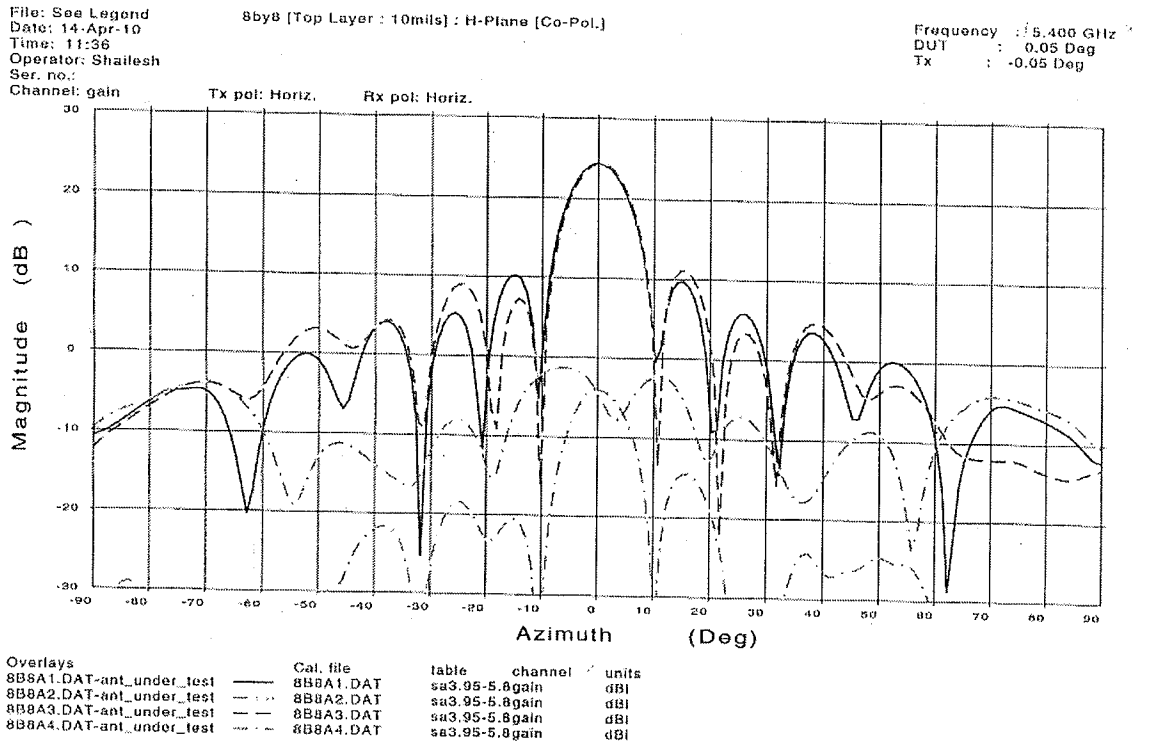

A.10 RADIATION PATTERN (5.45 GHZ)

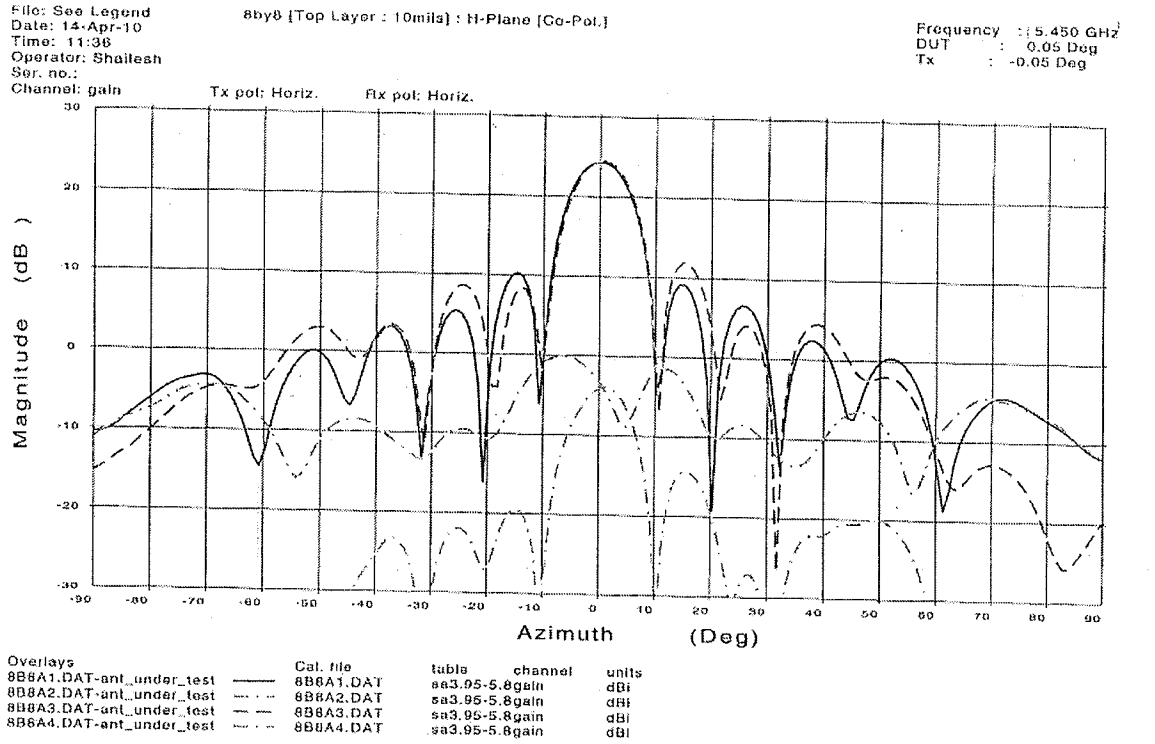

CRC

FR950
Automated Antenna
Measurement Systems

A.11 RADIATION PATTERN (5.50 GHZ)

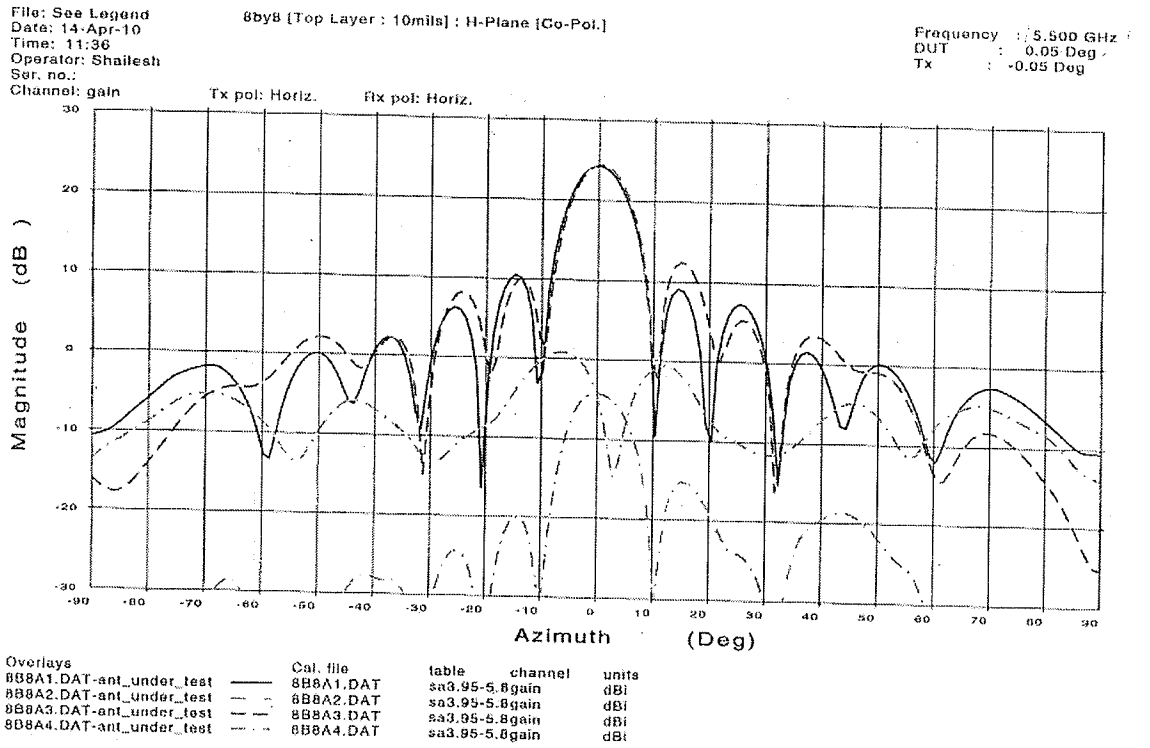

CRC

FR959
Automated Antenna
Measurement Systems

A.12 RADIATION PATTERN (5.55 GHZ)

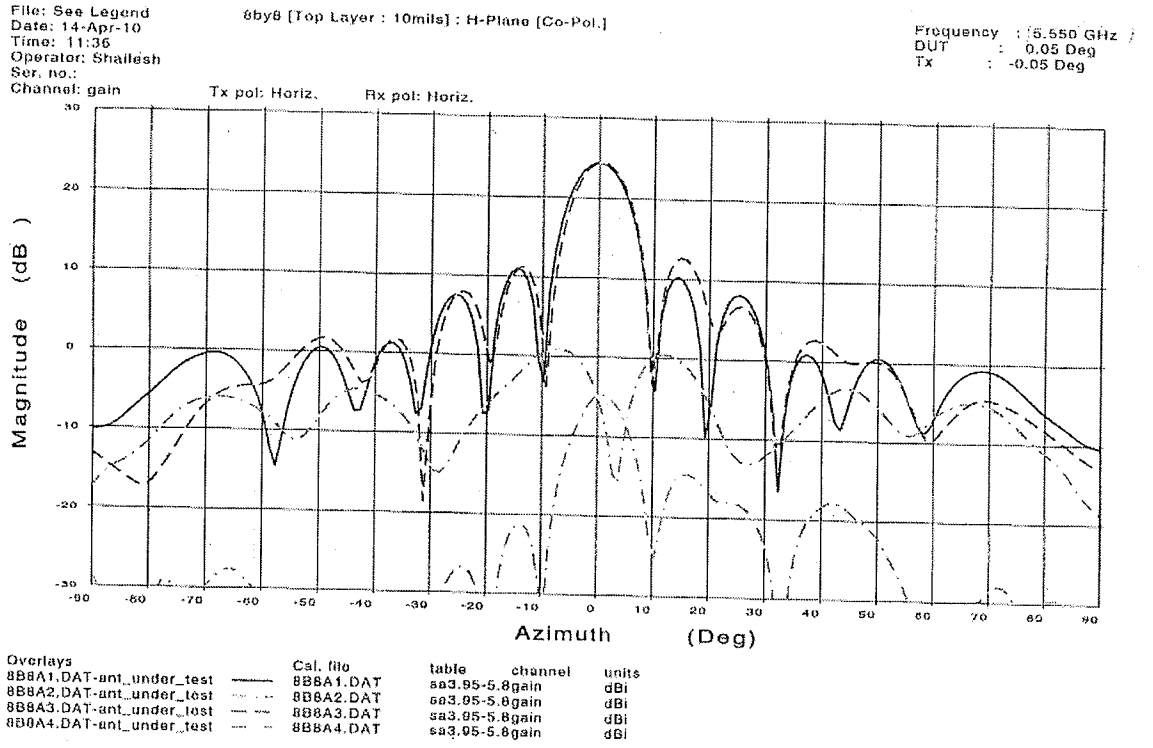

CRC

CR959
Automated Antenna
Measurement Systems

A.13 RADIATION PATTERN (5.60 GHz)

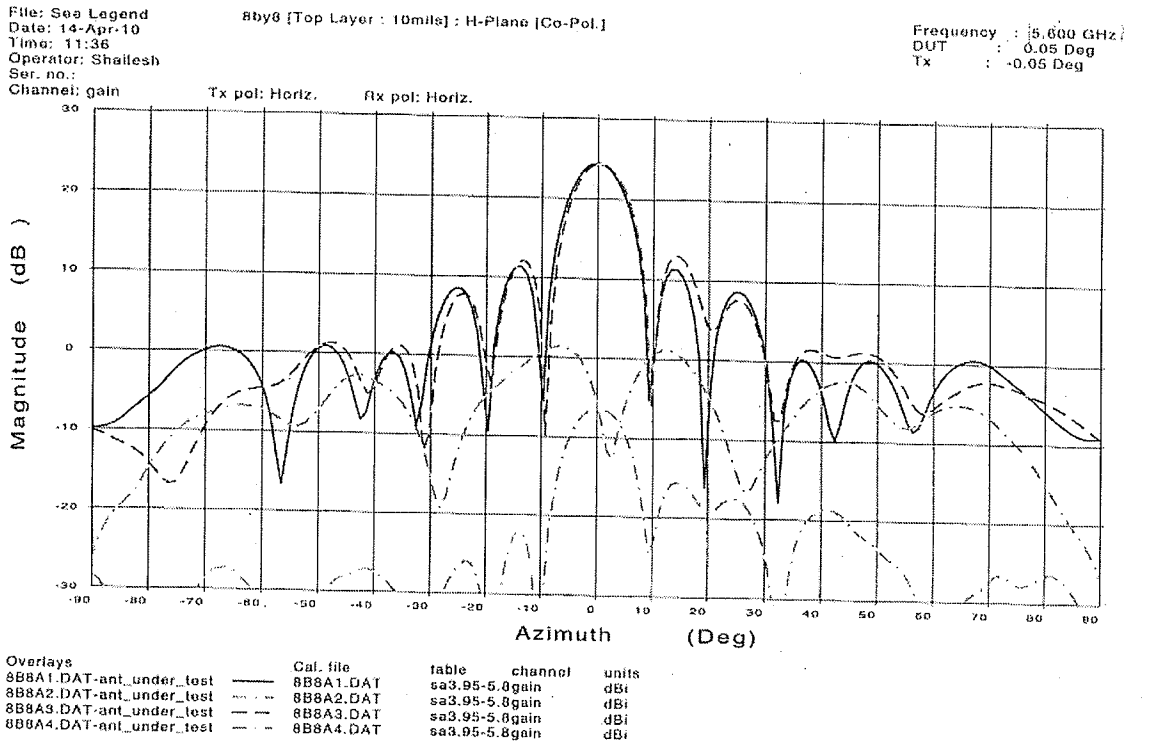

A.14 RADIATION PATTERN (5.65 GHZ)

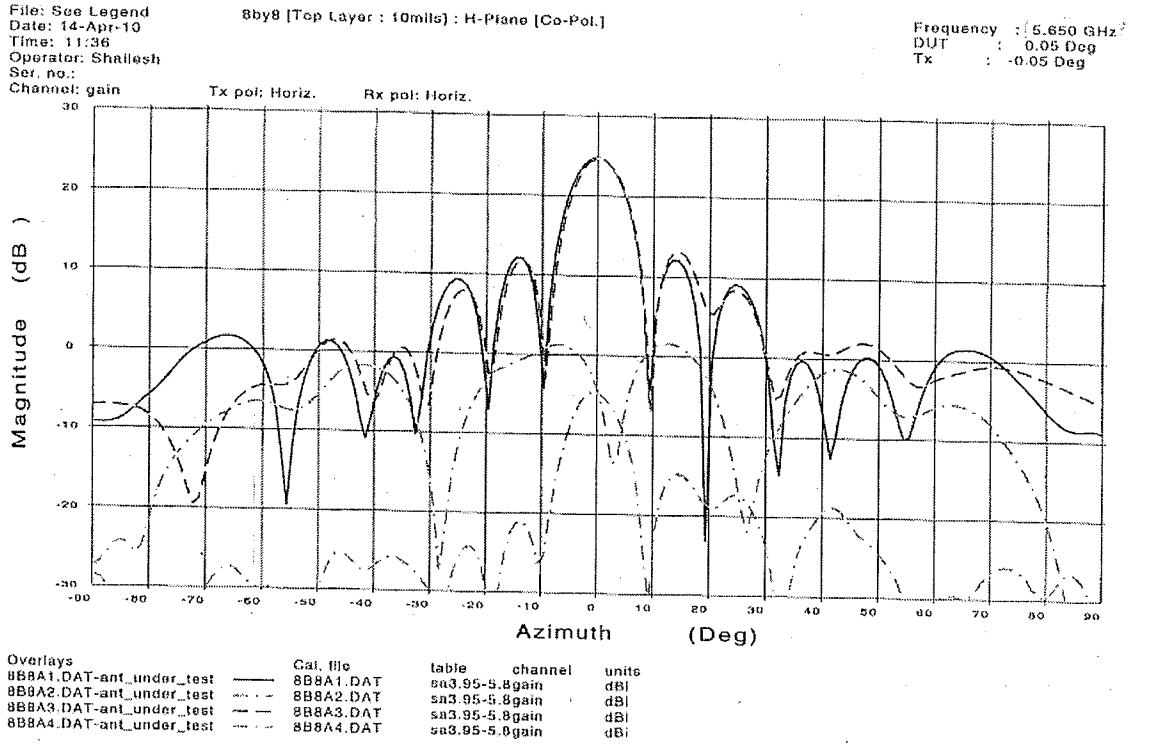

A.15 RADIATION PATTERN (5.70 GHZ)

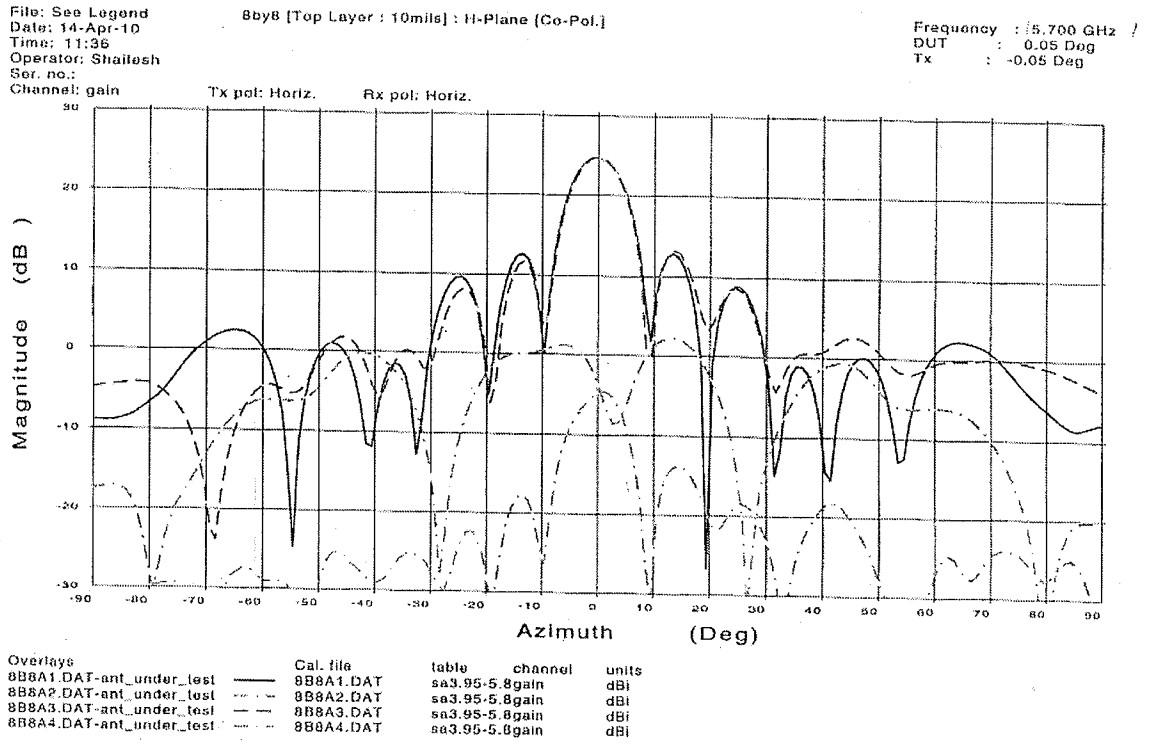

A.16 RADIATION PATTERN (5.75 GHZ)

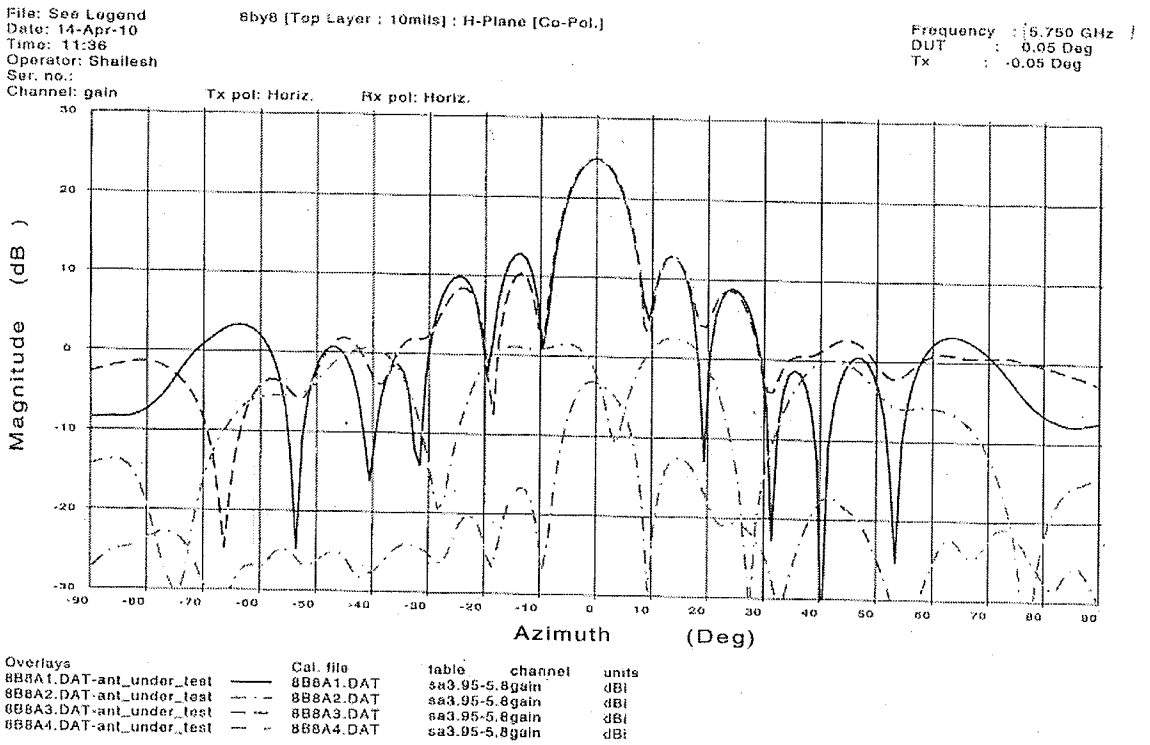

CRC

FR959
Automated Antenna
Measurement Systems

A.17 RADIATION PATTERN (5.80 GHz)

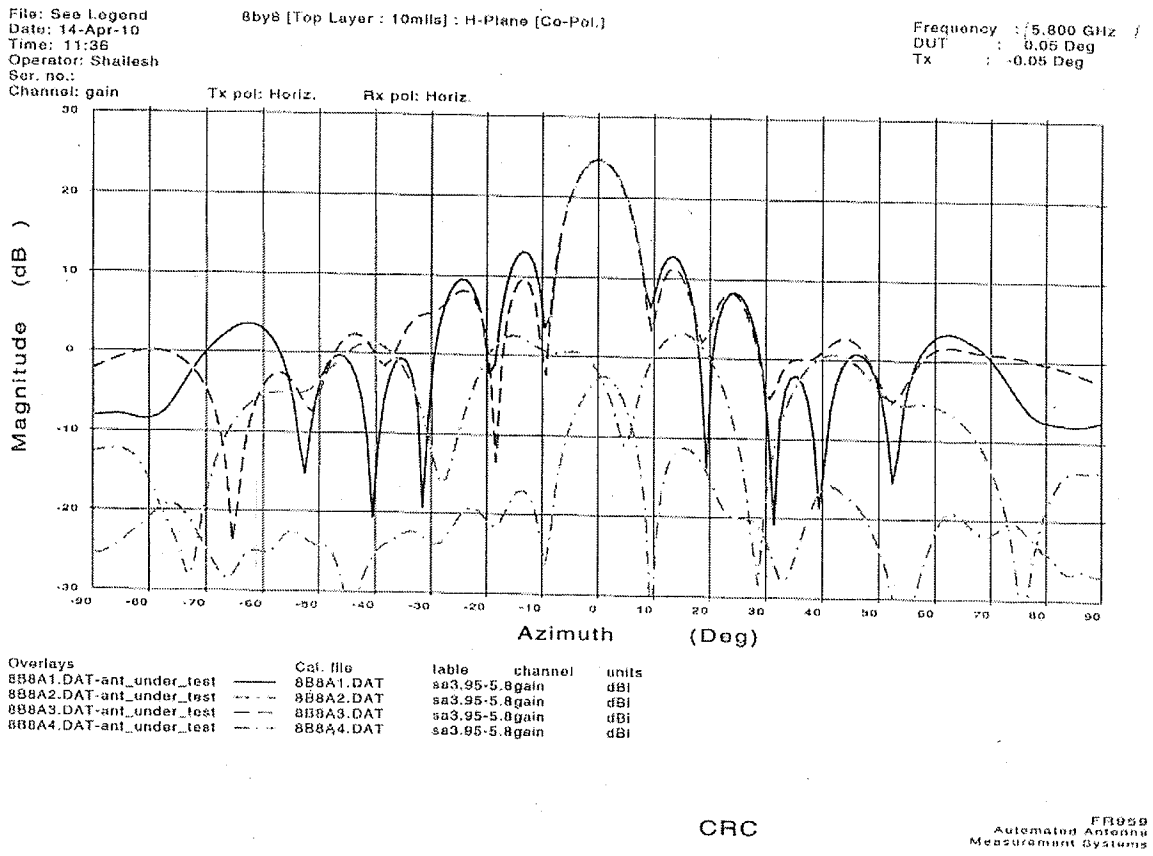

A.18 RADIATION PATTERN (5.85 GHz)

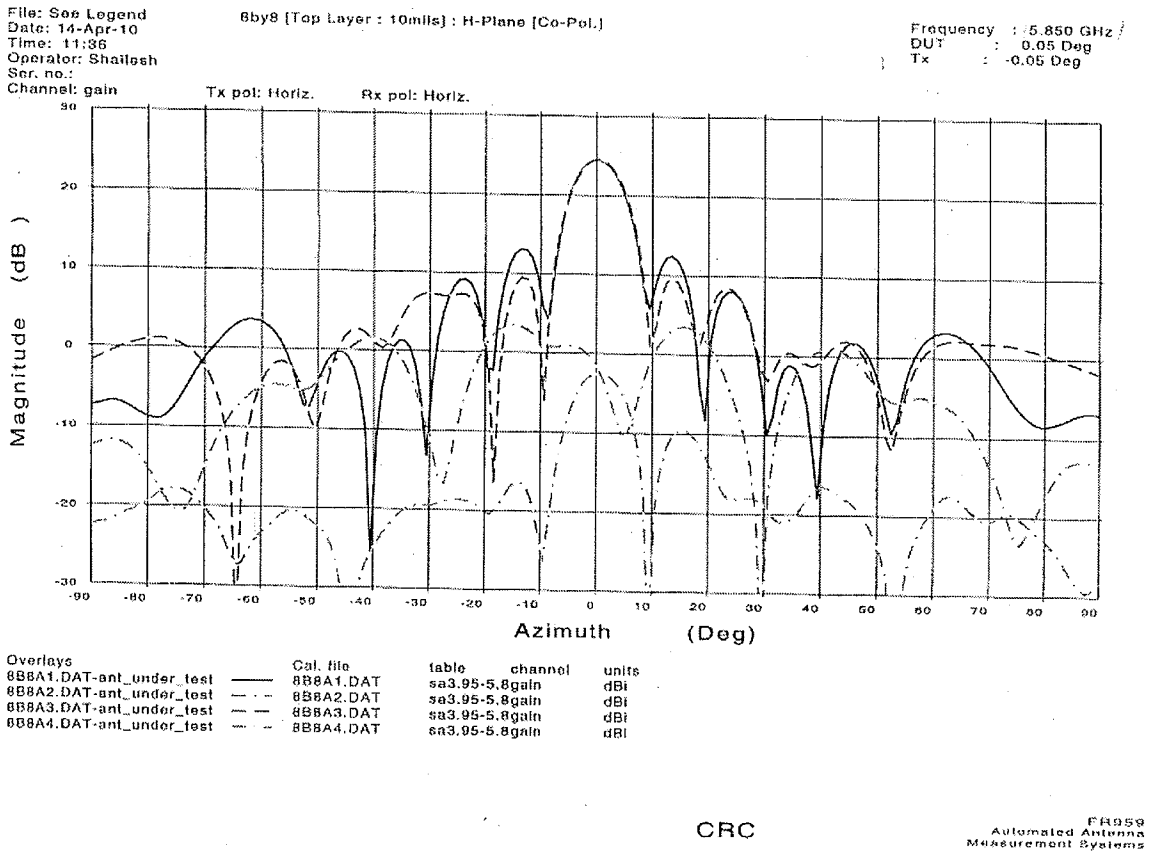

APPENDIX B: LATTICE THEORY

The lattice is the mathematical abstraction of a grid used to represent a sampling structure for 2D signals. The grid structure used in this dissertation is a particular case of lattice known as *rectangular grid*, but any regular distribution of sample points in 2D space can be a lattice as long as it can be specified by a set of integer vectors. In this Appendix, the fundamental definitions and properties used within this dissertation will be presented. A thorough review of the sampling theory of multidimensional signals on lattices can be found in Dubois' paper [14]; an excellent review of lattice theory with applications can also be found in [15] and [71]. The definitions presented in this Appendix and the uses of notation are based on [71].

Definition B.1: A lattice Λ, in the real K-D space, R^K, is the set of all possible vectors that can be represented as integer-weighted linear combinations of K linearly independent basis vectors, $v_k \in R^K$, $k = \{1,2,\ldots,K\}$. That is,

$$\Lambda = \left\{ x \in R^K \mid x = \sum_{k=1}^{K} n_k v_k \in Z \right\} \tag{B.1}$$

where Z represents the space of integer numbers in this context. The generating matrix, also called the sampling matrix, is defined as

$$V = \{v_1, v_2, \ldots, v_K\} \tag{B.2}$$

In this context, the lattice defined by the generating matrix V is noted as

$$\Lambda = LAT(V) \tag{B.3}$$

For a given generating matrix, any point in the lattice can be represented as a linear combination of the integer coefficients, n_k, $k \in K$. Hence, any sample point can be represented by an integer vector $n = [n_1, n_2, \ldots, n_K]^T \in Z$. The position of any point in the lattice is

$$x = Vn \tag{B.4}$$

Theorem B.1: Given a lattice Λ, one can find a unit cell $U(\Lambda)$ so that its translation to all points covers the entire R^K space with non-overlapping replicas, i.e.

$$\bigcup_{x \in \Lambda} (U + x) = R^K \tag{B.5}$$

where $U + x = \{p + x \mid p \in U\}$, and $(U + x) \cap (U + y) = \phi$, $x \neq y$. The basis vectors that define the generating matrix are not unique, hence, there is more than one unit cell $U(\Lambda)$.

Definition B.2: The polygon enclosed by the vectors corresponding to the basis vectors of the lattice Λ is defined by

$$P(\Lambda) = \left\{ x \in R^K \mid x = \sum_K \alpha_k v_k, \forall 0 \leq \alpha_k \leq 1 \right\} \tag{B.6}$$

The translation of the fundamental polygon to all lattice points forms a partition of R^K, and by (B.5), the fundamental polygon is a unit cell of Λ.

Definition B.3: The Voronoi cell of a lattice is the set of points which are closer to the origin than any other points in the lattice, i.e.

$$\Delta(\Lambda) = \left\{ x \in R^K \mid d(x,0) \le d(x,p), \forall p \in \Lambda \right\} \tag{B.7}$$

As well as the unit polygon, the Voronoi unit cell defines a partition of R^K, therefore, it is a unit cell $U(\Lambda)$.

Definition B.4: The *volume* of the unit cell is unique although there is more than one possible unit cells, and its reciprocal represents the *sample density* of Λ, i.e.

$$d(\Lambda) = \frac{1}{\det(V)} \tag{B.8}$$

where det symbolizes the determinate of the generating matrix V.

Definition B.5: Given a lattice with generating matrix V, its reciprocal lattice Λ^* is defined as a lattice with a generating matrix

$$U = (V^T)^{-1} \tag{B.9}$$

The inner product between points from a lattice and its reciprocal lattice is an integer. If $x = Vm \in \Lambda$ and $y = Un \in \Lambda^*$, then $x^T y = m^T V^T U n = m^T n \in Z$ by (B.9). Therefore, the basis vectors of Λ and Λ^* are orthogonal.

Definition B.6: Given a continuous signal $s_c(x)$, $x \in R^K$, a sampled signal over a lattice Λ is defined as

$$s_\Lambda(n) = s_c(Vn) \tag{B.10}$$

where s_Λ is the sampled signal over a lattice Λ, whose generating matrix is V, $x \in \Lambda$, and $n \in Z^K$.

Definition B.7: The Fourier transform of a sampled signal over Λ is defined as

$$S_\Lambda(f) = \sum_{n \in Z^K} s_\Lambda(n) \exp(-j2\pi f^T V n) \tag{B.11}$$

where s_Λ is the sampled signal on Λ, $f = [u_1, u_2, \ldots, u_K]$ is the spatial frequencies vector. Note that, if $f^T x = k \in Z$, then $\exp(-j2\pi f^T x) = 1$, therefore,

$$S_\Lambda(f + Um) = S_\Lambda(f) \tag{B.12}$$

where U is defined in (B.9). Expression (B.12) implies that the Fourier transform of a signal sampled on a lattice Λ is periodic with periodicity given by U, and that the spectral distribution is centered on every point defined by the reciprocal lattice Λ^*. The period is the Voronoi cell of the reciprocal lattice $\Delta(\Lambda^*)$, whose spectral content is repeated at all points of Λ^*.

Definition B.8: The inverse Fourier transform is defined as

$$s_\Lambda(n) = \frac{1}{d(\Lambda)} \int_{\Delta(\Lambda^*)} S_\Lambda(f) \exp(j2\pi f^T V n) df$$

where $d(\Lambda)$ is the sample density over the lattice Λ, $\Delta(\Lambda^*)$ is the Voronoi cell of the reciprocal lattice Λ^* and $S_\Lambda(f)$ is the frequency spectrum of the sampled signal defined in (B.10).

Definition B.9: The linear convolution of two sampled signals , s_Λ and g_Λ, over the same lattice Λ is defined as

$$s_\Lambda(n) * g_\Lambda(n) = \sum_{m \in \Lambda} s_\Lambda(n-m) g_\Lambda(m) \tag{B.13}$$

where n and $m \in \Lambda$. If $h_c(x)$, $x \in R^K$, is the impulse response of a linear shift-invariant system, applying the sampling defined in (B.10) over a lattice Λ, then the impulse response over the lattice is defined by $h_\Lambda(n)$ and the output of the system to an input signal $s_\Lambda(x)$ over the same lattice is given by (B.13).

Definition B.10: The convolution of sampled signals in Λ is equivalent to the product of their Fourier transform over Λ^*, i.e.,

$$s_\Lambda(n) * h_\Lambda(n) \leftrightarrow S_\Lambda(f) H_\Lambda(f) \tag{B.14}$$

Definition B.11: The impulse signal over a sampling lattice Λ is defined as

$$\delta_\Lambda(n) = \begin{cases} 1, n = [0,...,0] \\ 0, n \neq [0,...,0] \end{cases}$$

where $n \in Z^K$.

Definition B.12: The shift invariance property of a linear system is verified if and only if, given the sampled response $h_\Lambda(n)$ to an impulse $\delta(n)$, n $\in Z^K$, over a lattice Λ, the impulse response to a shifted impulse $\delta_\Lambda(n+m)$, m $\in Z^K$, is $h_\Lambda(n+\mathrm{m})$.

Theorem B.2: (The Generalized Nyquist Sampling Theorem) When a continuous signal $s_c(x)$, $x \in R^K$, is sampled over a lattice Λ with generating matrix V, creating the sampled

version $s_s(n)$, $n \in \Lambda$, then its Fourier transform over the reciprocal lattice Λ^* with generating matrix U is given by

$$S_\Lambda(f) = d(\Lambda) \sum_{f_m \in \Lambda^*} S_c(f - f_m) = d(\Lambda) \sum_{f_m \in \Lambda^*} S_c(f - Um) \qquad \text{(B.15)}$$

where $S_c(f)$ is the K-D Fourier transform of the continuous multidimensional signal $s_c(x)$. In other words, the Fourier transform of a sampled signal over a lattice Λ is the sum of the translated versions of the K-D Fourier transform of the continuous signal over all the points of the reciprocal lattice Λ^*. Since the K-D sampling grid is tessellated by the Voronoi unit cell (B.7), it is possible to recover the original continuous signal from its sampled signal version if and only if the frequency components of the original signal Fourier transform are limited to the Voronoi unit cell of Λ^*, i.e.

$$S_\Lambda(f) = 0, \forall f \notin \Delta(\Lambda^*) \qquad \text{(B.16)}$$

In order to avoid aliasing when sampling a continuous signal on a lattice Λ, the frequency content of the continuous multi-dimensional signal should be band-limited to the support region defined by the unit cell of the reciprocal lattice Λ^*.

REFERENCES

[1] H. L. Bertoni, *Radio Propagation for Modern Wireless Systems*, Prentice-Hall, 1999.

[2] R. Bose, A. Freedman, and B. Steinberg, "Sequence CLEAN: a modified deconvolution technique for microwave images of contiguous targets," *IEEE Trans. on Aerospace and Electronics Systems*, vol. 38, no. 1, pp. 89-96, Jan. 2002.

[3] R. J. C. Bultitude, "Measurement, characterization, and modeling of indoor 800/900 MHz radio channels for digital communications," *IEEE Commun. Magazine*, vol. 25, no. 6, pp. 5-12, Jun. 1987.

[4] R. J. C. Bultitude, S. A. Mahmoud, and W. Sullivan, "A comparison of indoor radio propagation characteristics at 910 MHz and 1.175 GHz," *IEEE J. Selected Areas in Commun.*, vol. 7, no. 1, pp. 20-30, Jan. 1989.

[5] R. J. C. Bultitude, R. F. Hahn, and R. J. Davies, "Propagation considerations for the design of an indoor broadband communications system at UHF," *IEEE J. Selected Areas in Commun.*, vol. 11, no. 7, pp. 979-990, Sep. 1993.

[6] R. J. C. Bultitude, P. Melancon, H. Zaghloul, G. Morrison, and M. Prokki, "The dependence of the indoor multipath channel characteristics on transmit/receive ranges," *IEEE Trans. Veh. Technol.*, vol. 47, no. 1, pp. 235-245, Feb. 1998.

[7] Chia-Chin Chong, Y. Kim, and Seong-Soo Lee, "UWB indoor propagation channel measurements and data analysis in various types of high-rise apartments," *Proc. IEEE Vehic. Technol. Conference*, vol. 1, pp. 150-154, Sep. 2004.

[8] Chia-Chin Chong, Y. Kim, and Seong-Soo Lee, "A statistical based UWB multipath channel model for the indoor environments WPAN applications," *Proc. IEEE Intelligent Vehic. Symposium*, pp. 525-530, Jun. 2005.

[9] D. Chizhik, J. Ling, and R.A. Valenzuela, "The effects of electric field polarization on indoor propagation," *IEEE 1998 International Conference on Universal Personal Communications*, ICUPC '98, vol. 1, pp. 459-462, Oct. 1998.

[10] D. C. Cox, R. R. Murray, H. W. Arnold, A. W. Norris, and M. F. Wazowicz, "Cross-polarization coupling measured for 800 MHz radio transmission in and around houses and large buildings," *IEEE Trans. Antennas Propagat.*, vol. 34, no. 1, pp. 83-87, Jan. 1986.

[11] R. J. Cramer, M. Z. Win, and R. A. Scholtz, "Evaluation of the multipath characteristics of the impulse radio channel," *Antennas and Propagation International Symposium*, vol. 2, pp. 626-630, Jun. 1998.

[12] N. Czink, M. Herdin, H. Ozcelik, and E. Bonek, "Number of multipath clusters in indoor MIMO propagation environments," *Electronic Letters*, vol. 40, no. 23, pp. 1498-1499, Nov. 2004.

[13] D. M. Devasirvatham, M. J. Krain, and D. A. Rappaport, "Radio propagation measurements at 850 MHz, 1.7 GHz and 4 GHz inside two dissimilar office buildings," *Electronic Letters*, vol. 26, no. 7, pp. 445-447, Mar. 1990.

[14] E. Dubois, "The sampling and reconstruction of time-varying imagery with applications in video systems," *Proceedings of IEEE*, no. 73, pp. 502-522, Apr. 1985.

[15] E. Dubois, "Image processing and image communication, Chapter 2: two and three-dimensional signals and systems", *ELG 5378 Class notes*, University of Ottawa, pp. 2-62, Jan. 2006.

[16] H. El-Sallabi, L. Vuokko, J. Kivinen, P. Vainiakainen, "Indoor directional and temporal channel characteristics for MIMO wideband channel modeling at 5 GHz," *Proc. Antennas and Propagation Soc. International Symposium*, vol. 3B, pp. 414-417, Jul. 2005.

[17] B. H. Fleury, D. Dahlhaus, R. Heddergott, and M. Tschudin, "Wideband angle of arrival estimation using the SAGE algorithm," *Proc. IEEE International*

Symposium in Spread Spectrum Techniques and App., vol. 1, pp. 140-144, Sep. 1997.

[18] G. J. Foschini and M. J. Gans, "On limits of wireless communications in a fading environment when using multiple antennas," *Proc. Wireless Personal Commun.*, vol. 6, no. 3, pp. 311-335, Mar. 1998.

[19] J. Fuhl and A. Molisch, "Virtual-image-array single-snapshot (VIASS) algorithm for direction-of-arrival estimation of coherent signals," *Proc. IEEE Int. Symposium in Personal, Indoor and Mobile Communications*, vol. 2, pp. 658-653, Sep. 1995.

[20] M. J. Gans, R. A. Valenzuela, Y. S. Yeh, and N. Amitay, "Antenna pattern deconvolution for precise incident power density pattern measurement," *Proc. Vehic. Technology Conf.*, VTC'00, vol. 3, pp. 2532-2535, May 2000.

[21] R. Ganesh and K. Pahlavan, "Statistical modeling and computer simulation of the indoor wireless channel," *IEE Proceedings*, vol. 138, no. 3, pp. 297-302, Jun. 1991.

[22] R. C. Gonzalez and P. Wintz, *Digital Image Processing*, 2nd ed., Addison-Wesley, Nov. 1987.

[23] L. Gurrieri, C. Squires, S. Noghanian, and T. Willink, "High resolution spatiotemporal characterization of the electric field polarization on indoor environments", *Proc. IEEE Canadian Conference on Electrical and Computer Engineering*, CCECE/CCGEI, pp. 940-943, Ottawa, May. 2006.

[24] L. Gurrieri, S. Noghanian, and T. Willink, "Indoor wireless reception improvement using cross-polarized multipath signals," *Proc. of ANTEM/URSI 2006*, pp. 273-276, Montreal, Jul. 2006.

[25] S. Haykin and J. H. Justice, *Array Signal Processing*, Prentice Hall, Inc., Englewood Cliffs, New Jersey, 1985.

[26] S. J. Howard and K. Pahlavan, "Measurement and analysis of the indoor radio channel in the frequency domain," *IEEE Trans. Instrum. Meas.*, vol. 39, pp. 751-755, 1990.

[27] IEEE 802.11 standard group document, *IEEE std 802.11g-2003*, http://ieeexplore.ieee.org/servlet/opac?punumber=8601.

[28] IEEE 802.15 standard group document, *IEEE std 802.15.1-2005*, http://ieeexplore.ieee.org/servlet/opac?punumber=9980.

[29] S. M. Jefferies and J. C. Christou, "Restoration of astronomical images by iterative blind deconvolution," *American Astronomical Society, The Astronomical Journal*, no. 415, pp. 862-874, Oct. 1993.

[30] M. A. Jensen, Q. H. Spencer, A. Lee Swindlehurst, and B. D. Jeffs, "Measuring and modelling of temporal and spatial indoor multipath characteristics," *IEEE J. Select. Areas Commun.,* vol. 18, no. 3, pp. 347-360, Mar. 2000.

[31] Y. L. C. de Jong and M. H. Herben, "High-resolution angle-of-arrival measurement of the mobile radio channel," *IEEE Trans. Antennas. Propagat.*, vol. 47, pp. 1677-1687, Nov. 1999.

[32] S. Kapp, "802.11a: more bandwidth without wires," *IEEE Internet Computing*, no. 4, vol. 6, pp.75-79, Jul-Aug 2002.

[33] K. Kalliola, K. Sulonen, H. Laitinen, O. Kivekas, J.Krogerus, and P. Vainikainen, "Angular power distribution and mean effective gain of mobile antenna in different propagation environments," *IEEE Trans. Veh. Technol.*, vol. 51, no. 5, pp. 823-838, Sep. 2002.

[34] K. Kalliola, H. Laitinen, L. I. Vaskelainen, and P. Vainikainen, "Real-Time 3-D spatial-temporal dual-polarized measurement of wideband radio channel at mobile station," *IEEE Trans. Instrum. Meas.*, vol. 49, no. 2, Apr. 2000.

[35] J. Kivinen, X. Zhao, and P. Vainikainen, "Empirical characterization of wideband indoor radio channel at 5.3 GHz," *IEEE Trans. Antennas Propag.*, vol. 49, no. 8, Aug. 2001.

[36] P. Kyritsi, D. Cox, R. A. Valenzuela, and P. W. Wolniansky, "Effect of antenna polarization on the capacity of a multiple element system in an indoor environment," *IEEE J. Selected Areas in Commun.*, vol. 20, no. 6, pp. 1227-1239, Aug. 2002.

[37] A. Leshem and A. J, Van Der Veen, "Adaptive suppression of RFI and its effect on radio-astronomical image formation," vol. 3, pp. 616-619, Oct. 2001.

[38] T. Lo and J. Litva, "Angles of arrival of indoor multipath," *Electron. Letters,* vol. 28, no. 18, pp. 1687–1689, Aug. 1992.

[39] Y. Lim, J. Kim, S. L. Min, and J. S. Ma, "Performance evaluation of the bluetooth-based public Internet access point," *Proc. 15th International Conference on Information Networking*, pp. 643-648, Jan. 2001.

[40] J. Litva, A. Ghaforian, and V. Kezys, "High resolution measurements of AoA and time-delay for characterizing indoor propagation environments," *Proc. 8th Int. Conf. in Wireless Communications*, vol. 2, pp. 514-518, Calgary, Canada, July 1996.

[41] L. C. Lukama, D. J. Edwards, and A. Wain, "Application of three-branch polarization diversity in the indoor environment," *IEE Proc-Commun.*, vol. 150, no. 5, pp. 399-403, Oct. 2003.

[42] T. Manabe, Y. Miura, and T. Ihara, "Effects of antenna directivity and polarization on indoor multipath propagation characteristics at 60 GHz," *IEEE J. Select. Areas Commun.*, vol. 14, no., pp. 44-48, Apr. 1996.

[43] J.T. E. McDonnell, T.P. Spiller, and T.A. Wilkinson, "Characterization of the spatial distribution of RMS delay spread in indoor LOS wireless environments at 5.2GHz," *IEEE Symposium on Personal, Indoor and Mobile Communic.*, vol. 2, pp. 621-624, Sept. 1998.

[44] A. Molisch, "Ultrawideband propagation channels-theory, measurement, and modeling," *IEEE Trans. Veh. Technol.*, vol. 54, no. 5, pp. 1528-1544, Sep. 2005.

[45] A. Muqaibel, A. Safaai-Jazi, A. Bayman, A. M. Attiya, and S. M. Riad, "Ultrawideband through-the-wall propagation," *IEE Proc.-Microw. Antennas Propag.*, vol. 152, no. 6, pp. 581-588, Dec. 2005.

[46] R. U. Nabar, H. Bolcskei, V. Erceg, D. Gesbert, and A. J. Paulraj, "Performance of multiantenna signaling techniques in the presence of polarization diversity," *IEEE Trans. Signal Process.*, vol. 50, no. 10, pp. 2553-2562, Oct. 2002.

[47] M. Nilsson, B. Volcker, and B. Ottersten, "A cluster approach to spatio-temporal channel estimation," *Proc. IEEE Acoustics, Speech, and Signal Proc.*, ICASSP'00, vol. 5, pp. 2757-2760, Jun. 2000.

[48] Y. A. Olenko, K. T. Wong, and J. Ahmadi-Shokouh, "Analytically derived ToA & 2D-AoA distributions with scatterers in a 3D hemispheroid surrounding the mobile," *Proc. Globecom 2004*, pp. 872-876, 2004.

[49] Y. A. Olenko, K. T. Wong, and M. Abdulla, "Analytically derived ToA-AoA distributions of uplink/downlink wireless-cellular multipaths arising from scatterers with an inverted-parabolic spatial distribution around the mobile," *IEEE Signal Processing Lett.*, vol. 12, no. 7, Jul. 2005.

[50] B. Ottersten and T. Kailath, "Direction-of-arrival estimation for wide-band signals using the ESPRIT algorithm," *IEEE Trans. Acoust., Speech, Signal Processing,* vol. 38, no. 2, pp. 317-327, Feb. 1990.

[51] K. Pahlavan and A. H. Levesque, *Wireless Information Networks*, 2nd Ed., John Wiley & Sons, Inc., 2005.

[52] K. M. Pasala and R. P, Penno, "Accurate determination of frequency and angle of arrival from undersampled signals," *IEEE Antennas and Prop. Soc. Symposium*, vol. 2 pp. 686-689, July 1993.

[53] A. Petosa, "Patch array near-field simulation results," *Antenna Design and Development*, CRC Internal Communication 2006.

[54] J. D. Parson, *The Mobile Radio Propagation Channel*, 2nd ed. West Sussex, England: John Wiley, 2000.

[55] S. U. Pillai, *Array Signal Processing*, Springer Verlang, 1989.

[56] J. G. Proakis, *Digital Communications*, 3rd ed., New York: McGraw-Hill, 1995.

[57] T. Rappaport, *Wireless Communications: Principles and Practice*, Prentice Hall, 2001.

[58] T. S. Rappaport, "Characterization of UHF multipath radio channels in factory buildings," *IEEE Trans. Antennas Propag.*, vol. 37, no. 8, pp. 1058-1069, Aug. 1989.

[59] T.S. Rappaport, S. Y. Seidel, and K. Takamizawa, "Statistical channel impulse response models for factory and open plan building radio communication system design," *IEEE Trans. Commun.*, vol. 39, pp. 794-807, May 1991.

[60] T. S. Rappaport and D. A. Hawbaker, "Effects of circular and linear polarized antennas on wideband propagation parameters in indoor radio channels," *Proc. IEEE Globecom*, vol. 2, pp. 1287-1291, Dec. 1991.

[61] T. S. Rappaport and D. A. Hawbaker, "Wide-band microwave propagation parameters using circular and linear polarized antennas for indoor wireless channels," *IEEE Trans. on Commun.*, vol. 40, no. 2, Feb. 1992.

[62] A. M. Saleh and R. A. Valenzuela, "A statistical model for indoor multipath propagation," *IEEE J. Select. Areas Commun.*, vol. 5, no. 2, pp. 128-137, Feb. 1987.

[63] S. Simoens, P. Pellati, J. Gosteau, K. Gosse, and C. Ware, "The evolution of 5GHz WLAN toward higher throughputs," *IEEE Wireless Communications*, vol. 10, no. 6, pp. 6-13, Dec. 2003.

[64] R. Schmidt, "Multiple emitter location and signal parameter estimation," *IEEE Trans. Antennas and Propagation,* vol. 34, pp. 276-280, Mar.1986.

[65] E. Sousa, V. M. Jovanovic, and C. Daignaeult, "Delay spread measurements for the digital cellular channel in Toronto," *IEEE Trans. Veh. Technol.*, vol. 43, no. 4, pp. 837-847, Nov. 1994.

[66] Q. Spencer, M. Rice, B. Jeffs, and M. Jensen, "Indoor wideband time/angle of arrival multipath propagation results," *Proc. of the IEEE Vehicular Technology Conference* (VTC '97), Pheonix, Arizona, pp. 1410-1414, May 1997.

[67] Q. Spencer, M. Rice, B. Jeffs, and M. Jensen, "A statistical model for angle of arrival in indoor multipath propagation," *Proc. of the IEEE Vehicular Technology Conference* (VTC '97), Pheonix, Arizona, pp. 1415-1419, May 1997.

[68] Q. H. Spencer, B. D. Jeffs, M. A. Jensen, and A. L. Swindlehurst, "Modeling the statistical time and angle of arrival characteristics of an indoor multipath channel," *IEEE Trans. Veh. Technol.*, vol. 18, no. 3, pp. 569-571, Mar. 2000.

[69] T. Svantesson, "Correlation and channel capacity of MIMO systems employing multimode antennas," *IEEE Trans. Veh. Technol*, vol. 51, no. 6, pp. 1304-1312, Nov. 2002.

[70] J. Tsao, B. Steinberg, "Reduction of sidelobe and speckle artifacts in microwave imaging: the CLEAN technique," *IEEE Trans. Antennas Propagat.*, vol. 36, no. 4, pp. 543-546, Apr. 1988.

[71] Y. Wang, J. Ostermann and Y.-Q. Zhang, *Video Processing and Communications*, Prentice-Hall, 2002.

[72] T. J. Willink, "Extraction of impulse response from MIMO measurement data - Mark I," *CRC Internal Communication*, 2004.

[73] M. Z. Win and R. A. Scholtz, "Ultra-wide bandwidth signal propagation for indoor wireless communications," *Proc. of IEEE International Conference on Communications*, Montreal, vol. 1, pp. 56-60, Jun. 1997.

[74] M. Z. Win and R. A. Scholtz, "Characterization of ultra-wide bandwidth wireless indoor channels: a communication-theoretic view," *IEEE J. Select. Areas Commun.*, vol. 20, no. 9, pp. 1613-1627, Dec. 2002.

[75] K. Yu, Q. Li, and M. Ho, "Measurements investigation of tap and cluster angular spreads at 5.2 GHz," *IEEE Trans. Antennas Propagat.*, vol. 53, no. 7, pp. 2156-2160, Jul. 2005.

[76] C. Young, C. Ko, and B. Wu, "Field measurements and ray tracing simulations for indoor wireless communications," *Proc. IEEE Int. Symposium on Personal, Indoor, and Mobile Communications*, PIMRC'96, vol. 3, pp. 15-18, Oct. 1996.

[77] H. Xu, V. Kukshya, and T. Rappaport, "Spatial and temporal characterization of 60 GHz indoor channels," *IEEE J. Select. Areas Commun.*, vol. 20, no. 3, pp. 620-630, Apr. 2002.